TECHNISCHE UNIVERSITÄT WIEN

DIPLOMARBEIT

Dependence of Quantification Accuracy on Emission Scan Duration in PET/MR

ausgeführt am Institut für Angewandte Physik der
Technischen Universität Wien

unter der Anleitung von

Ao.Univ.-Prof. DI Dr. Martin Gröschl

und

als verantwortlich mitwirkendem Universitätsassistenten

Jacobo Cal González, PhD

Center for Medical Physics and Biomedical Engineering
Medizinische Universität Wien

durch

Stefan Wampl

Moosham 22
4816 Gschwandt

25. Oktober 2016

Acknowledgements

I would like to express my gratitude to my supervisor at TU Wien, Martin Gröschl, for the opportunity of the masters thesis and preceding project works, for the throughout smooth cooperation and for his constant patience.

My deepest thanks go to Jacobo Cal González for his supervision at Medical University of Vienna. Thanks for the insights and expertise, for introducing me to the world of scientific working and writing, and especially for the incredible support along the way. This way would have been quite lonely without my colleagues from the QIMP-group, especially Ivo, Lalith and Martin. Thanks for your constant help and the knowledge you shared. Special thanks to Thomas Beyer for giving me the possibility of working in and learning from such an exquisite group.

I also thank my colleagues from Technical Physics at TU Wien, Marko, Martin, Sebastian and Vimal, for accompanying me through the last years that eventually led to this work. I am particularly grateful for the thorough review given by Roman Schmied.

I want to thank all people that inspired, motivated or surprised me in the process of writing this thesis. Especially Katrin, I can't thank you enough for all your support and good will in the last months. Thanks to my sister for being a constant inspiration.

Abschließend gebührt der größte Dank meinen Eltern für ihre bedingungslose Unterstützung auf dem gesamten Weg hierher!

Contents

Abstract

Aim

The quantification accuracy of PET images depends on several factors, such as patient status, data acquisition protocol or image reconstruction settings. The objective of this study is to evaluate the impact of acquisition time on the quantitative accuracy of PET images, reconstructed by using different settings, for phantom and patient scans in a PET/MR system.

Materials and Methods

Phantom measurement of a FDG-filled NEMA IQ Body Phantom is acquired in 20 min list mode with a true lesion-to-background ratio (LBR_true) of 4.1. Full acquisition is split to receive sets of 10 min, 5 min, 3 min, 2 min and 1 min images using reconstruction settings OSEM (4it, 21subs, 5 mm FWHM Gaussian post-filtering) and PSF (4it, 21subs, no filtering). Image quality is evaluated by recovery coefficients (RC), signal-to-noise ratios (SNR) and segmented volumes (VOL), for the maximum activity and for mean activities segmented at 41 %, 50 % and 70 % adapted to background. 8 ^{68}Ga $-$ DOTANOC and 16 ^{18}F $-$ FET patients with gliomas are included in the study. 10 min list mode scans for one bed position are performed and reconstructed with OSEM and PSF to receive sets of 5 min, 3 min, 2 min, 1 min and 30 s images. Image quality is assessed via standardized uptake values (SUV), LBR, SNR and VOL for the maximum and mean activities as for the phantom. All measures are referenced to the image with longest frame time and the relative deviation of each image to the reference image is statistically evaluated.

Results

For maximal reduction of acquisition time, by a factor of 20, image noise increases significantly in phantom and patient data with average increases of up to 100 % for OSEM reconstructions and up to 200 % for PSF. RC_max increases especially for bigger spheres (12 % OSEM, 56 % PSF), while RC_{41} shows around half of these deviation values. In patients, SUV_max increases by 8-10 % with OSEM and by 50-65 % in PSF, while SUV_{41} shows less dependence on acquisition time. SNR_max decreases similarly for phantom and ^{68}Ga $-$ DOTANOC data (-70 % in OSEM, -80 % in PSF), but less in ^{18}F $-$ FET data (-40 % in both, OSEM and PSF). Reduction of acquisition time by a factor of 6 (OSEM) or 5 (PSF) does not yet significantly influence RC_max. With OSEM reconstruction in patient studies, scan time can be lowered to 3 min in ^{18}F $-$ FET patients or 5 min in ^{68}Ga $-$ DOTANOC patients without significant effect on SUV_max.

Conclusion

The increase of image noise with shorter scan duration induces significant increases of RC_max and SUV_max and a substantial decrease of SNR_max, all together affecting quantification accuracy adversely. Measures with segmentation at 41 % threshold are affected notably less by reducing acquisition duration than maximum activity measures. We propose potential reductions of acquisition time of up to 50 % without compromising image quality significantly.

Kurzfassung

Ziel

Die Genauigkeit der quantitativen PET-Aufnahmen hängt von verschiedenen Faktoren wie Patientenstatus, Aufnahmeprotokoll oder Rekonstruktionseinstellungen ab. Diese Arbeit beschäftigt sich mit dem Einfluss der Aufnahmezeit auf qualitative und quantitative PET-Bildgrößen von Phantom und Patienten PET/MR-Aufnahmen unter Verwendung verschiedener Rekonstruktionseinstellungen.

Methodik

Die Messung des NEMA IQ Phantoms, befüllt mit FDG und einem Konzentrationsverhältnis von 4.1, wurde im list-mode Modus mit $20\,\text{min}$ Dauer aufgenommen. Die gesamte Aufnahme wurde jeweils vollständig in Aufnahmen mit $10\,\text{min}$, $5\,\text{min}$, $3\,\text{min}$, $2\,\text{min}$ and $1\,\text{min}$ Länge geteilt und mit den zwei Verfahren OSEM (4it, 21subs, $5\,\text{mm}$ FWHM Gauss-Filter) und PSF (4it, 21subs, kein Filter) rekonstruiert. Die Bildqualität der Phantom-Messung wurde anhand von Rückgewinnungs-Koeffizienten (RC), Signal-zu-Rausch-Verhältnissen (SNR) und segmentierten Volumen (VOL) analysiert. Die Kenngrößen wurden jeweils für die maximale Aktivität und die mittleren Aktivitäten in einem an die Hintergrundaktivitäten angepassten Grenzwert von $41\,\%$, $50\,\%$ and $70\,\%$ segmentierten Volumen erhoben. 8 $^{68}\text{Ga} - \text{DOTANOC}$ und 16 $^{18}\text{F} - \text{FET}$ Patienten mit Gliomen waren in die Studie involviert. Die $10\,\text{min}$ list-mode Aufnahmen wurden mit OSEM und PSF rekonstruiert und jeweils in Bilder mit $5\,\text{min}$, $3\,\text{min}$, $2\,\text{min}$, $1\,\text{min}$ and $30\,\text{s}$ aufgeteilt. Die Bildqualität wurde anhand von standardisierten Absorptionswerten (SUV), Läsion-zu-Hintergrund-Verhältnissen (LBR), SNR und VOL bewertet. Alle Messgrößen wurden auf die längste Aufnahmezeit bezogen und die relative Abweichung jeden Bildes zum Referenzbild statistisch ausgewertet.

Ergebnisse

Für die maximale Reduktion der Aufnahmezeit um einen Faktor 20 nahm das durchschnittliche Rauschen in den Phantom- und Patienten-Bildern bis zu $100\,\%$ mit OSEM Rekonstruktion und bis zu $200\,\%$ mit PSF Rekonstruktion zu. Vor allem für größere simulierte Läsionen stieg $RC_{\max}$ signifikant an ($12\,\%$ OSEM, $56\,\%$ PSF), wobei RC_{41} nur halb so starke Abweichungen aufzeigte. In den Patienten nahm $SUV_{\max}$ um 8-10 % mit OSEM und um 50-65 % mit PSF zu, während SUV_{41} wieder deutlich geringere Abhängigkeit von der Aufnahmezeit zeigte. $SNR_{\max}$ nahm in Phantom- und $^{68}\text{Ga} - \text{DOTANOC}$ Aufnahmen stärker ab (ca. $-70\,\%$ mit OSEM, $-80\,\%$ mit PSF), aber weniger deutlich in $^{18}\text{F} - \text{FET}$ Aufnahmen (ca. $-40\,\%$ mit OSEM und PSF). Bei Reduktion der Aufnahmezeit um einen Faktor 6 (OSEM) oder 5 (PSF) wird $RC_{\max}$ noch nicht statistisch signifikant beeinflusst. Mit OSEM Rekonstruktion konnte in Patienten-Bildern die Aufnahmedauer auf $3\,\text{min}$ ($^{18}\text{F} - \text{FET}$ Patienten) bzw. $5\,\text{min}$ ($^{68}\text{Ga} - \text{DOTANOC}$ Patienten) gesenkt werden ohne signifikante Auswirkungen auf $SUV_{\max}$ zu beobachten.

Erkenntnisse

Die Zunahme des Bildrauschens bei kürzerer Messzeit bewirkt einen merklichen Anstieg von $RC_{\max}$ und $SUV_{\max}$ und eine deutliche Abnahme von $SNR_{\max}$, was in Summe die quantitative Bewertung der Bilder nachteilig beeinflusst. Jene Messgrößen, die auf einer 41 %-Segmentierung beruhten, zeigten erheblich weniger Abweichungen bei verkürzter Aufnahmezeit als jene, denen die maximalen Aktivitäten zugrunde lagen. Potenzielle Reduktion um 50 % der Messdauer ohne signifikanten Einfluss auf die Bildqualität konnte nachgewiesen werden.

Chapter 1

Introduction

Over the last decades, Positron Emission Tomography (PET) has been developed as a central tool for functional imaging in nuclear medicine. In contrast to conventional anatomic imaging techniques as Computed Tomography (CT) or Magnetic Resonance Imaging (MRI), PET visualizes functional information based on the (dynamic) distribution of a radiopharmaceutical that is incorporated into the target tissue (e.g. tumor cells) (Muehllehner and Karp, 2006). In order to achieve this, indicators for physiologic processes are labelled with a radionuclide which eventually decays at the site of uptake. This allows the visualization of the tracer distribution and the localization of regions with higher uptake (Ziegler, 2005). Its applications spread over several different clinical fields, from neurology and psychiatry through drug discovery and their development to cardiology and the currently most frequent application, oncology. In neurology and psychiatry, PET is valued for early diagnosis and differentiation of dementias, in the studying of movement disorders, in pre/surgical examination of epilepsy-patients and in the detection and discrimination of brain tumors (Tai and Piccini, 2004). For cardiologists, PET plays an increasing role in the diagnosis of coronary artery disease, especially in the assessment of myocardial perfusion and viability (Bengel et al., 2009). In oncology, PET significantly elevated the clinical possibilities of diagnosis, detection, grading and staging of tumors, as well as monitoring response to therapy and identifying recurrences (Bailey et al., 2005). The quantitative character of PET imaging improved or even replaced qualitative visual assessment of images by introducing semi-quantitative (Standardized Uptake Value - SUV) or fully quantitative (by kinetic modelling) measures for tumor uptake (Ziai et al., 2016; Bai et al., 2013a). Those measures allow absolute comparison of different scans and enable general assessment of grading, staging or response to therapy based on accurate quantification of the tumor uptake (Kinahan and Fletcher, 2010).

Due to the significant increase of CT scans in recent years (UNSCEAR, 2008) and the rapid development and consequent expansion of hybrid PET/CT systems (Beyer et al., 2000), the exposure of patients, technologists and people in waiting areas to radiation from medical imaging has been topic of several investigations (Benatar et al., 2000). The risks of cancer caused by ionizing radiation of medical imaging has been evaluated for adults (Einstein, 2012; Nguyen et al., 2011; Huang et al., 2010) and adolescents, identifying increased risks especially from recurring computed tomography scans in childhood (Pearce et al., 2012; Mathews et al., 2013). Efforts to reduce doses and radiation exposure were initially focusing on CT, mainly proposing reduction by optimizing scan protocols (Huang et al., 2009; Nievelstein et al., 2012). Various studies identified the CT scan(s) of a combined PET/CT study as the main cause for dose exposure to patients. A multi-center study revealed a total received dose of 25 mSv per PET/CT evaluation, of which ~ 7.0 mSv arose from the PET scan itself (Brix et al., 2005). In paediatric PET/CT studies, average exposures of a PET/CT study were similar (24.8 mSv) with a contribution of the tracer injection of 4.6 mSv (Chawla et al., 2010). Dose reductions by adapting CT protocols were studied, showing that exposures varied between 13 mSv and

32 mSv (PET: 6.2 mSv) depending on the applied protocol (Huang et al., 2009), which eventually led to the evaluation of low-dose protocols with 14.5 mSv (PET: 6.3 mSv) per PET/CT scan (Willowson et al., 2012). With optimized low-dose CT protocols, the administered activities for the PET scan gain significant importance, contributing up to 50 % of the total received radiation dose. In the recently introduced PET/MR hybrid systems (Schlemmer et al., 2008), the radiation exposure solely is caused by the PET component, creating the need of improving patient exposure in this part of the scan.

Motivated by the ALARA (*as low as reasonably achievable*) principle, several studies have been conducted to evaluate the influence of radiotracer reduction on the image quality. Beside adapting the administered dose to bodyweight (Boellaard et al., 2015) and body-mass-index (BMI) (Sanchez-Jurado et al., 2014), optimal injection doses were obtained through patient-specific noise-equivalent count (NEC) rates (Inoue et al., 2012; Lartizien et al., 2002; Walker et al., 2009) as well as through a combination of BMI and NEC (Carlier et al., 2013). Oehmigen et al. verified in a phantom study that image quality could be maintained by prolonging acquisition time to the same degree as reducing the injected activity (Oehmigen et al., 2014). When reducing acquisition time by 50 %, the influence on image quality was admittedly visible but did not yet affect feasibility for clinical assessment (Hausmann et al., 2012). To the contrary, quantitative accuracy degrades significantly when reducing scan time by half, showing high noise levels and underestimation of the maximum activity in PET/CT (Molina-Duran et al., 2014; Halpern et al., 2004). Equally, lesion-detection performance of automated observer algorithms degraded for reduced scan time, on the other hand showing significant improvements with resolution recovery and time-of-flight systems (Kadrmas et al., 2012). Comparison of time-of-flight systems of both, PET/CT and PET/MR Zeimpekis et al., suggested a possible reduction of up to 37 % in dose or acquisition time while ensuring the same image quality(Zeimpekis et al., 2015). Similarly, Alessio et al. found lesion detection in paediatric PET/CT to be still accurate for reductions of acquisition time by up to 40 % of acquisition time (Alessio et al., 2011). In a phantom study, the minimal activity-time product and the minimal total number of recorded counts were found as $17\,\mathrm{MBq\,min}$ and $1 \times 10^5\,\mathrm{/s\,min}$, respectively (Chen et al., 2016). Cheng et al. showed the validity of SUV-values for a wide range of acquisition times (Cheng et al., 2014).

Objective

Most existing evaluations to reduce either acquisition time or administered doses have widely concentrated on PET/CT, on either patient or phantom data, or were analysed qualitatively by observers. Furthermore, patient studies were rare and mostly covered a low number of participants for a specific region, and lacking evaluation of different radiotracers.

In this study we want to evaluate the influence of acquisition duration on the quantitative accuracy of PET/MR brain imaging for a broad set of parameters. We will compare measurements in a controlled environment (phantom) to clinically acquired brain scans of patients with two different tracers ($^{68}\mathrm{Ga} - \mathrm{DOTANOC}$ and $^{18}\mathrm{F} - \mathrm{FET}$). Both, phantom and patient data will be analysed by using different image reconstruction settings in order to evaluate the effect of reconstruction parameters on the quantification accuracy when reducing acquisition time.

Structure

The physical and technical basics of PET imaging from production of radionuclides to image formation through to tomographic image reconstruction are presented in Chapter 2. Chapter 3 describes the methodology used in this work. First the phantom acquisitions and the data analysis for the phantom experiment are explained, followed by the patient data selection and analysis. The first section of

Chapter 4 deals with the results of the phantom analysis, the second section with the evaluation of patient data. The figures of merit are presented consecutively in separate subsections. In the discussion, Chapter 5, the most important results are summarized, results of analysing phantom and patient data are evaluated and compared. Relation of the results obtained in this work to published values in the literature is also presented in Chapter 5. Finally, in Chapter 6 the main conclusions of this master thesis are highlighted.

Chapter 2

Theoretical Background and PET Basics

This chapter presents a general introduction to positron emission tomography (PET). In Section 2.1 the basic physical principals of PET are introduced. The following sections cover imaging in PET, from image formation (Section 2.2), to image reconstruction (Section 2.3), eventually to image quantification (Section 2.4). The last section, Section 2.5, gives a historical overview of PET systems, describes current scanner types and mentions principal radiotracers for clinical application. For further details on the physics of PET, the reader is referred to Bailey et al. (2005) and Cal González (2014).

2.1   Physics of PET

Starting from mechanisms to produce radionuclides via the physical process of positron emission through to the interaction with matter, this section presents the main physical principles needed to understand positron emission tomography.

2.1.1   Production of Radionuclides

Common radionuclides used for clinical applications (Table 2.1) are either produced in a cyclotron or manufactured in a specific generator. In a cyclotron, a high frequency alternating electric field is applied in the gap between two semicircular hollow electrodes (see Figure 2.1). These so called *dees* (originating from their D-shape) are put in a static magnetic field generated by two electromagnets, all placed in a vacuum chamber. Charged particles are injected to the center of the device and are accelerated by an electric field ($F_{\mathrm{elec}} = q \cdot E$). Upon entering a dee, the magnetic field forces the moving charged particles to circular paths (Lorentz-force: $F_{\mathrm{magn}} = q \cdot \vec{v} \times \vec{B}$). The radiofrequency of the alternating current source is synchronized to the cyclotron frequency

$$\omega_{\mathrm{C}} = \frac{qB}{m} = const. \tag{2.1}$$

of the particle with charge q and mass m in the magnetic field of strength B. It is set in such a way that the electric field changes its direction exactly when a particle exits a dee again. With each crossing of the gap, the particle gains energy and the radius of its circular path inside the dees increases. After reaching a certain speed, the particle beam can be extracted at the exit port. A cyclotron can be operated with both, positively and negatively charged ions. For the production of protons, H^- ions are injected into the cyclotron and accelerated but stripped off the electrons at the exit port.

For the production of radionuclides, a cyclotron is used to deliver protons for collisional (p,n)-processes. For instance, the radionuclide ^{18}F, which consists of 9 protons and 9 neutrons, is typically produced in a
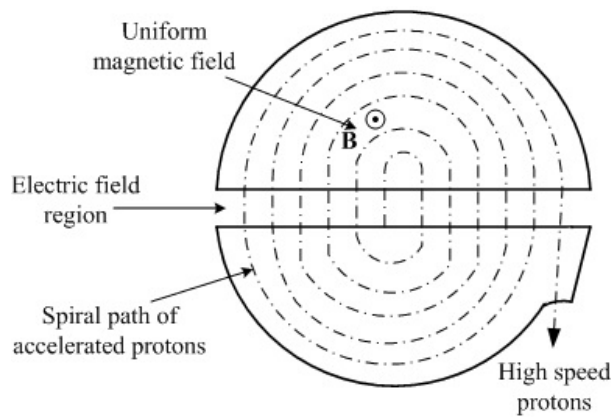
Figure 2.1: *Acceleration of positively charged particles (e.g. protons) in a cyclotron (from Brilliant.org).*

cyclotron via a (p,n)-reaction with highly enriched ^{18}O water as target material. In this process a proton is captured in an ^{18}O nucleus with prompt ejection of a neutron leading to the ^{18}F-nuclide (Guillaume et al., 1991). After extracting ^{18}F from the ^{18}O enriched water, glucose molecules are labelled with the fluoride, e.g. by using a nucleophilic substitution reaction (Lasne et al., 2002).

Certain radionuclides (^{68}Ga, ^{82}Rb) are obtained as decay products from parent isotopes (^{68}Ge, ^{82}Sr) with significantly longer half-lifes. In specific generators the daughter nuclides are accumulated and can be extracted from the mixture due to different solubility of the products (Knapp and Mirzadeh, 1994).

Table 2.1: *Common positron-emitting radionuclides (extracted from Sonzogni (2016)).*

Radionuclide	Half-life [min]	β^+ branching fraction [%]	Mean β^+ energy [keV]	Production mechanism
^{11}C	20.36	99.8	386	Cyclotron
^{18}F	109.7	96.7	250	Cyclotron
^{64}Cu	762.0	17.6	278	Cyclotron
^{68}Ga	67.71	88.9	830	Generator (^{68}Ge)
^{82}Rb	1.258	95.4	1480	Generator (^{82}Sr)
^{89}Zr	4705	22.7	396	Cyclotron
^{124}I	6013	22.7	820	Cyclotron

2.1.2 β^+ Decay and Positron Emission

Positrons (e$^+$ or equally used β^+) are the so-called antiparticles of electrons (e$^-$) with the same mass ($m_{e^\pm} = 9.109 \times 10^{-31}$ kg) and spin quantum number ($s_{e^\pm} = 1/2$) but opposite electric charge ($q_{e^+} = +1\,e$). Positrons can be created either via pair production or via nuclear transformation. In the field of a nucleus, a neutral boson (e.g., a photon) can be convert into a pair of a fundamental particle and its corresponding antiparticle (e.g., e$^-$ and e$^+$), called pair production. The required energy for this process has to exceed at least the rest mass of the two particles created, which is 1.022 MeV in the case of an electron-positron pair. For photons above 2 MeV, the process of pair production is the dominant way of interaction with matter (see Subsection 2.1.3).

To understand the process of nuclear transformation, a step further down the scale to the fundamental constituents of matter, the so-called quarks, is necessary. Quarks exist in six types, their *flavours* up, down, strange, charm, top and bottom. Quarks additionally wear color charge, which causes attraction via the strong interaction and the combination of different quarks causes the formation of composite particles, so called hadrons. Combinations of three *valence* quarks are known as baryons, of which the most stable are the nucleons. Proton (p$^+$) and neutron (n^0) are built just of up-quarks (electric charge
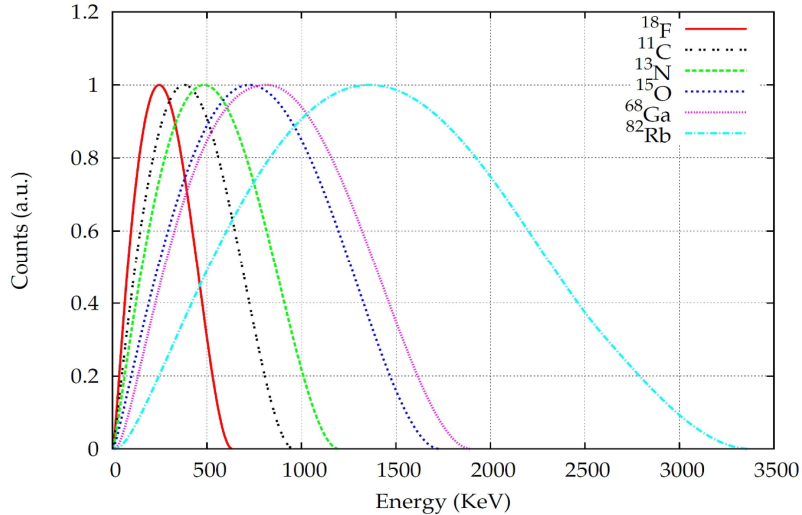
Figure 2.2: *β^+ spectra of several commonly used radioisotops in PET. Maxima are normalized to the respective maximum value (reprinted with permission from (Cal González, 2014)).*

$2/3\,e$) and down-quarks ($-1/3\,e$), the proton of two up and one down (uud), the neutron of one up and two down (udd). Quark flavor is conserved under all interactions except weak force which can mediate a change of a quarks flavour, e.g. from up to down, via exchange of intermediate vector bosons (W^+, W^- and Z^0). In a proton the change of an up- to a down-quark causes the proton to transform into a neutron while emitting a positron β^+ and an electron neutrino ν_e

$$p^+ \longrightarrow n^0 + e^+ + \nu_e + Q \tag{2.2}$$

which is called *beta plus (β^+) decay* or *positron emission*. The energy Q released during the decay is carried away as kinetic energy by the e^+ and the ν_e, and to negligible amounts by the nucleus. Positron and neutrino are emitted on a spectrum (Cross et al., 1983) as shown in Figure 2.2. The general β^+decay of a nucleus decreases the atomic number Z of the parent nucleus X by one

$$^A_Y X \longleftrightarrow {}^{A}_{Z-1} Y + e^+ + \nu_e + Q \tag{2.3}$$

and charge equilibrium forces the daughter nucleus Y to eject an orbital electron. In total two electron masses, the masses of the positron and the electron, are ejected from the nucleus and reduce the released energy Q by $1.022\,\mathrm{MeV}$. Therefore the required energetic gain for a positron decay, or equally the mass-difference of parent and daughter atom, has to exceed twice the electron mass for enabling nuclear transformation. Beta plus decay is more probable in proton-rich atomic nuclei and when high decay energies occur.

A competing decay mode to positron emission is electron capture (EC)

$$p^+ + e^- \longrightarrow n^0 + \nu_e + Q \tag{2.4}$$

where the nucleus is rather capturing an electron than emitting a positron. This decay mechanism is more probable for low decay energies and is the only decay mode for decay energies below two electron masses.

After a β^+ decay, the emitted positron has remaining kinetic energy which will be lost via inelastic

scattering and collisions with the surrounding atoms and electrons. The finite distance a positron is able to travel before annihilation, referred to as *positron range*, adds an intrinsic indeterminancy to the localization of the decaying nucleus. The positron range mainly depends on the emission energy of the β^+ particle, the surrounding material and the scanner size (Levin and Hoffman, 1999; Cal-Gonzalez et al., 2009). This limits the fundamental spatial resolution of a PET scanner to 0.54 mm and 2.83 mm FWHM for ^{18}F and ^{68}Ga, respectively (Moses, 2011). An e$^+$ and an e$^-$ can form the exotic atom *positronium*, where the particles orbit around their common center of mass for a short time. When the electron and the positron come close enough to each other and are basically at rest, they annihilate. The annihilation results in the emission of two photons (see Figure 2.3), each with the rest-mass equivalent of an electron, or similarly a positron (511 keV). Conservation of momentum forces the two photons to be emitted exactly in opposite directions. However, if the momentum of the positronium is not completely zero (center of mass energy), the annihilation photons are emitted with slight deviation from collinearity (non-collinearity $\sim$ 0.3 deg FWHM), as Figure 2.3 illustrates. This angular uncertainty causes a Gaussian blurring with a magnitude that is proportional to the radius of the PET detector ring (Shibuya et al., 2007).
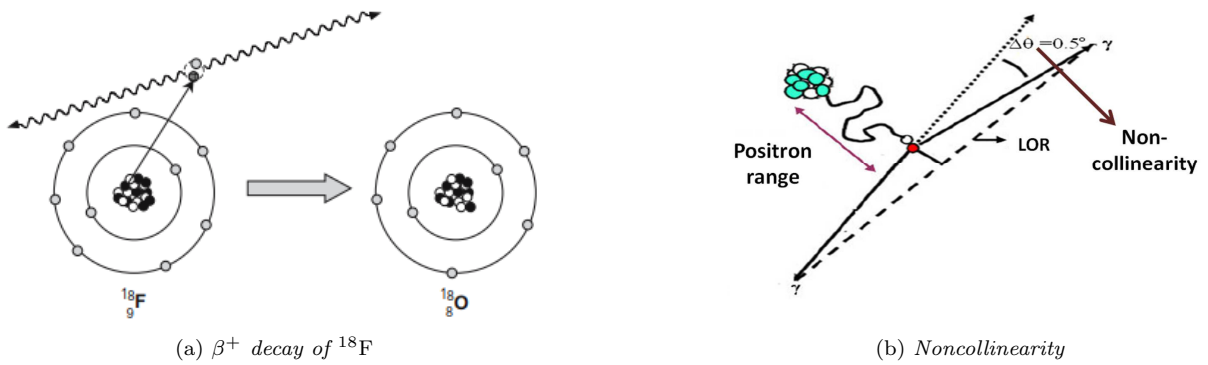

(a) β^+ *decay of* ^{18}F

(b) *Noncollinearity*

Figure 2.3: *Schematics for β^+ decay. (a) shows positron emission of the decaying nucleus, positron range (solid arrow), formation of positronium (dashed circle), final annihilation with emission of two collinear photons (wave-shaped arrows) (from (Bailey et al., 2005)). (b) additionally illustrates the effect of non-collinearity (reprinted with permission from (Cal González, 2014)).*

2.1.3 Interaction with Matter

If gamma rays are collimated to a monoenergetic beam, the attenuation of the beam when passing through a material can be described by the exponential attenuation of γ-rays:

$$I = I_0 \cdot e^{-\mu x} \tag{2.5}$$

where I_0 is the intensity of the incident beam, I the intensity after a distance x in the material and μ the linear attenuation coefficient. The probabilities of the three mainly contributing processes, photoelectric effect (τ), Compton scattering (σ) and pair production (κ), summarize to the linear attenuation coefficient $\mu = \tau + \sigma + \kappa$. The three processes relevant for the energy regimen in PET ($\sim$ 511 keV) are described in the following:

Photoelectric absorption: An incident photon with energy $h\nu$ interacts with an atom and transfers its energy completely to a bound electron (binding energy $E_b < h\nu$). Consequently the so-called photo-electron is ejected from the atom with remaining kinetic energy of:

$$E_{e^-} = h\nu - E_b \tag{2.6}$$

The photoelectric effect is relevant for energies up to $100\,\mathrm{keV}$.

Compton scattering: When interacting with a loosely bound electron in the material, a γ ray can transfer part of its energy to the electron without being absorbed. Due to conservation of energy and momentum, the direction of the photon changes by the scattering angle Θ_C and energy is transferred to the recoil electron:

$$E_e = E_\gamma \frac{1}{1 + \dfrac{E_\gamma}{m_e c^2}\left(1 - \cos\Theta_C\right)} \tag{2.7}$$

where E_γ is the initial photon energy and $m_e c^2$ is the restmass-equivalent of the electron (see Figure 2.4). This process is predominant for γ rays with energies of typical radioisotope sources ($100\,\mathrm{keV}$ to $10\,\mathrm{MeV}$).
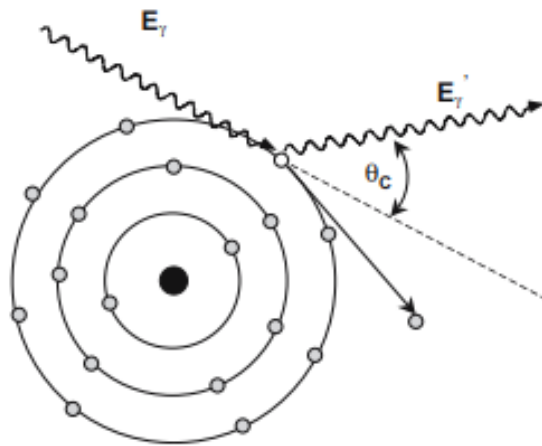

Figure 2.4: *Schematic of Compton scattering, visualizing the deflection by an angle θ_e of an incident photon with energy E_γ at a loosely bound electron (from (Bailey et al., 2005)).*

Pair production: For energies of several MeV or higher, another process called pair production is dominant. When a γ ray with similar energies interacts with the atomic or nuclear field, this can trigger the conversion of a γ quantum into a pair of particle and its according antiparticle. As a photon with basically zero rest-mass transforms into two particles with the same not vanishing mass, in order for this process to be energetically possible the γ ray requires at least the rest-mass-equivalent of the two particles. The specific and most probable case for pair production is the conversion of a γ ray into an electron-positron-pair. With the rest-mass-equivalent of electrons and positrons ($511\,\mathrm{keV}$), this process is energetically only possible for photon-energies above $1.022\,\mathrm{MeV}$ and most favorable for energies of several MeV. However, for the considered annihilation photons ($511\,\mathrm{keV}$) in the measurements presented here, this process is energetically not possible.

In Figure 2.5, the probabilities of the three mentioned interaction processes are illustrated for different energies and atomic numbers Z. The lines represent the constellations where the cross-sections σ_i of neighbouring processes are equal. At $511\,\mathrm{keV}$ (annihilation photons) we see, that for light absorber materials the Compton effect is dominant while for materials with approximately $Z > 80$ the photoelectric effect is more probable. This is especially important for detectors, where for high efficiency as little scattering as possible is wanted within the detector. Consequently, for high stopping power heavy or dense materials are needed.

2.1.4 Detectors in PET

Before signal processing, we will have a brief look into the most common detector types that are used in PET. This part is summarized from Lewellen (2008); Schaart et al. (2009); Grant et al. (2016); Lecomte
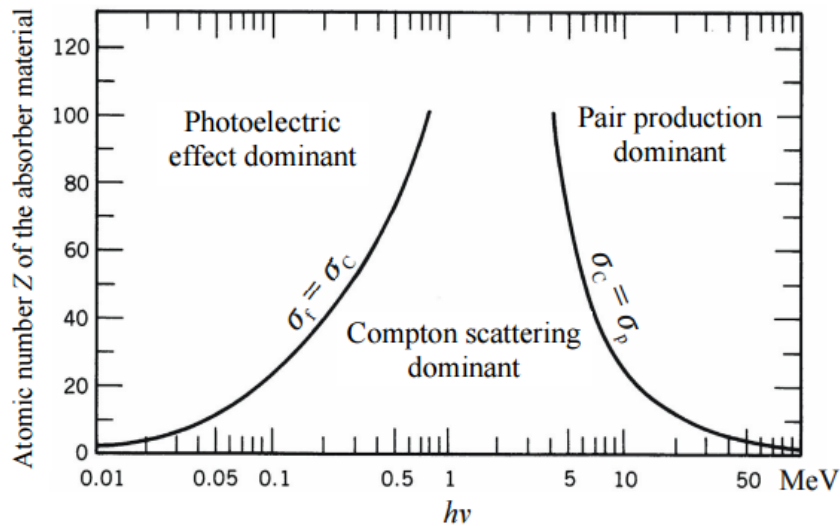
Figure 2.5: *The relative importance of the three major types of γ ray interaction. The lines show the values of Z (atomic number) of the absorber and hν for which the two neighbouring effects are just equal (from Knoll (2010)).*

(2009).

Scintillators

High energetic photons, as emitted from e^--e^+-annihilation (511 keV), can be detected by proportional counters, semiconductor-based detectors or scintillation detectors, of which the latter are most relevant in PET. Generally, a scintillation detector absorbs high energetic photons and re-emits visible light. This low energetic radiation can then be measured by photodetectors to produce electric signals. For practical reasons, most scintillators used in PET are solid, although they can be in liquid or gaseous form as well. They can be divided into organic and inorganic scintillators. In PET the desired properties of a scintillator are great stopping power for high sensitivity, high light output for good energy resolution, as well as fast response time to avoid pile-up of consecutive pulses and coincidences of uncorrelated photons. Good energy resolution is necessary for good scatter discrimination. Further, spatial resolution is normally increased by cutting the crystals into segments. Amongst the most favoured scintillation crystals in PET are BGO, NaI(Tl) and Luthetium-based scintillators.

Photodetectors

Photodetectors are coupled to the scintillator crystal, to detect the emitted scintillation light. They can either be photomultiplier tubes (PMTs) or semiconductor-based photosensors (APDs and SiPMs), which are described in the following:

Photomultiplier tubes (PMTs)   The most common technique is PMT, where the light-photon causes the ejection of an electron from the photocathode. This electron then is multiplied via secondary emission by the dynodes and eventually the signal with gains of 10^5-10^8 is collected at the anode, see Figure 2.6. Usually not a single crystal but scintillation arrays are coupled to the PMT to increase spatial resolution. A major drawback of PMTs is their sensitivity to magnetic fields, which disqualifies them for use in combined PET/MR systems.

Semiconductor-based photodetectors   Two types have emerged for the use in PET: avalanche photodiodes (APDs) and silicon photomultipliers (SiPMs). In APDs the scintillation light creates hole-electron pairs via the photoelectric effect. Compared to PMTs they have a higher photon detection
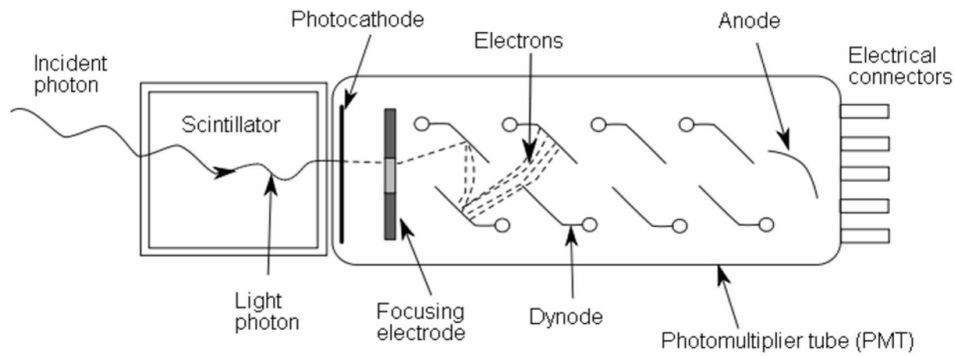
9

Figure 2.6: *Principle of operation of a photomultiplier tube (from Knoll (2010)).*

rate but show worse timing characteristics due to their low intrinsic gain, requiring subsequent electronic processing. Silicon Photomultipliers (SiPMs) are densely packed APDs operated in the Geiger-mode, which yields a high gain (10^5-10^6). Both semiconductor-based detectors have the advantage over PMTs that they are widely resistant against magnetic fields, what makes them applicable for combined PET/MR systems. SiPMs have the additional advantage of fast response and high gain over APDs, which made them the perfect candidate for detectors in time-of-flight PET/MR systems.

Single detectors are most commonly combined to block detectors to save costs and reduce the electronic complexity. Detector blocks are usually arranged in ring-shape, forming several detector rings.

2.2 Image Formation in PET

As seen in the previous section, annihilation leads to emission of two nearly collinear 511 keV photons. How these photons produce a valid signal and how this data is handled will be described in this section.

2.2.1 Classification of Events

In order to deliver a valid event, the two photons have to be registered within a specified time window (*coincidence time window*), the resulting line-of-response (LOR) has to be within a valid acceptance angle, and the energy deposited of each photon has to be within the selected *energy window*. Such a valid event is referred to as *prompt* event. However, there is a wide range of possibilities, how a prompt can be produced by two photons, of which not all are wanted. The possible events in a PET acquisition are as follows (see also Figure 2.7):

Single Events   When a detector registers a photon, this is called a single event. Between 1 % and 10 % of singles are converted into coincidence events.

Coincidence Events   Two photons that originate from the same annihilation and reach two opposed detectors without scattering on their way and lie within the limitations for a prompt, are called a coincidence or true events. For a true event, the point of annihilation lays exactly on the assigned LOR.

Scattered Events   If one or both annihilation photons are scattered, they loose energy and change direction. This means that their assigned LOR does not fit the origin of the annihilation any more (see Figure 2.7) and hence such photons are unwanted. Scattered photons that still lay within the prompt limitations, especially the energy window, form a scattered event. These contribute to noise in the image. Up to 30-40 % of all prompts are scattered events.

Random Events   It is also possible for uncorrelated photons to hit opposed detectors within the coincidence time window, producing accidental coincidence events called *randoms*. The number of randoms depends linearly on the coincidence time window t and the respective single event rates r of coincidence detectors i and j:

$$R_{ij} = 2tr_i r_j \tag{2.8}$$

The count rates can be assumed to be approximately balanced for all detectors throughout the ring, giving a quadratic dependence of the single event rate, $R_{ij} \propto r_i^2$.

Multiple Events   There is the possibility of more than two events being registered within one coincidence time window as well. Those *multiple events* originate from different sources (β^+-γ-emitters, coincidence-random pairing, double coincidences, etc.) and are either discarded by the electronics or incorrectly processed, contributing to additional noise in the image (Cal-González et al., 2015a).

The setting of the *coincidence (time) window* depends on various factors, e.g. the detector type, the scintillator material and the electronics. Time-of-flight (ToF) scanners use the time difference of two coincidence photons arriving at their respective detector to further specify the location of the annihilation on the LOR (Moses, 2003).
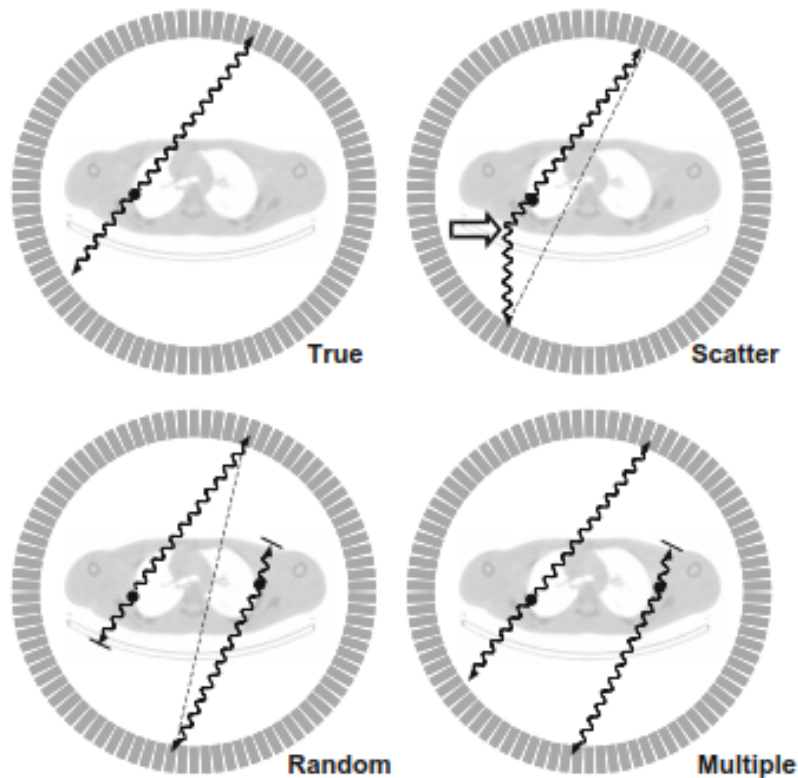
Figure 2.7: *Possible events recorded by a ring shape PET system (from Bailey et al. (2005)). For detailed description see text.*

2.2.2 Signal Processing

At this point we will have a look into the different acquisition modes of PET scanners, how the measured data is sorted and manipulated before the reconstruction.

Acquisition modes

Between detector rings, septas can be installed to prevent photons from crossing detector ring planes. This improves image resolution because of reduced scattered and random events, but reduces scanner sensitivity, as oblique true coincidences are rejected. Scans with installed septas are called two-dimensional (2D) scans, while scans without septas are referred to as operated in three-dimensional (3D) mode. Figure 2.8 visualizes the two acquisition modes. In 2D mode, data is only collected within a transaxial plane, allowing for separate reconstructions of the individual transaxial slices. In 3D mode, data is additionally collected for oblique planes, increasing the amount of data significantly as well as the effort for reconstruction. Although 3D reconstructions are more intensive to perform, clinical routine has shifted from acquiring in 2D mode due to the higher computing power of modern computers and the poorer sensitivity of 2D mode, which led to much noisier PET images at the same injected activity.

Sorting of data

The huge amount of acquired data requires efficient storage and in a convenient way for the subsequent reconstruction. Three different structures can be identified:

List mode	In this format, all prompt coincidences are stored chronologically in a list. The data for each event can include informations from the measurement (deposited energy, crystal number, etc.) as well as external data (count rate, time, gating information).
LOR histograms	Assumed, an annihilation took place somewhere in the FOV of the scanner, the resulting

photons were detected by two opposed detectors d_a and d_b, as illustrated in Figure 2.8. We then only can adopt, that the annihilation took place somewhere on the line connecting the two detectors, the so called line-of-response (LOR). Instead of listing all recorded coincidences with their respective timing information, the events can be stored for each LOR individually, which corresponds to the LOR histogramm.

Sinograms A LOR can either be described by the detector pair d_a-d_b or by the following set of variables: radial distance s to the center of the FOV, transaxial angle ϕ and axial angle θ (see Figure 2.8). In the 2D case, a projection of the spatial activity distribution $f(x,y)$ at angle ϕ is defined as the sum of all parallel LORs at that angle ϕ:

$$P(s,\phi) = \int_{-\infty}^{\infty} f(x,y)dy \qquad (2.9)$$

This is the Radon Transform $P(s,\phi)$ of the spatial activity distribution $f(x,y)$, see Figure 2.9. Arranging the Radon transformations of all angles in a matrix, gives a sinogram. A point source transformed for many different angles resembles a sine wave in the sinogram, hence the name. Every event detected by the pair d_a-d_b increments the value of its associated bin in the sinogram. For an extended object this results in the overlap of numerous sine waves in the sinogram. In multi-ring detectors for each plane (direct, cross and oblique) one sinogram is generated, as indicated in Figure 2.8. For more detailed information the reader is referred to (Fahey, 2002).
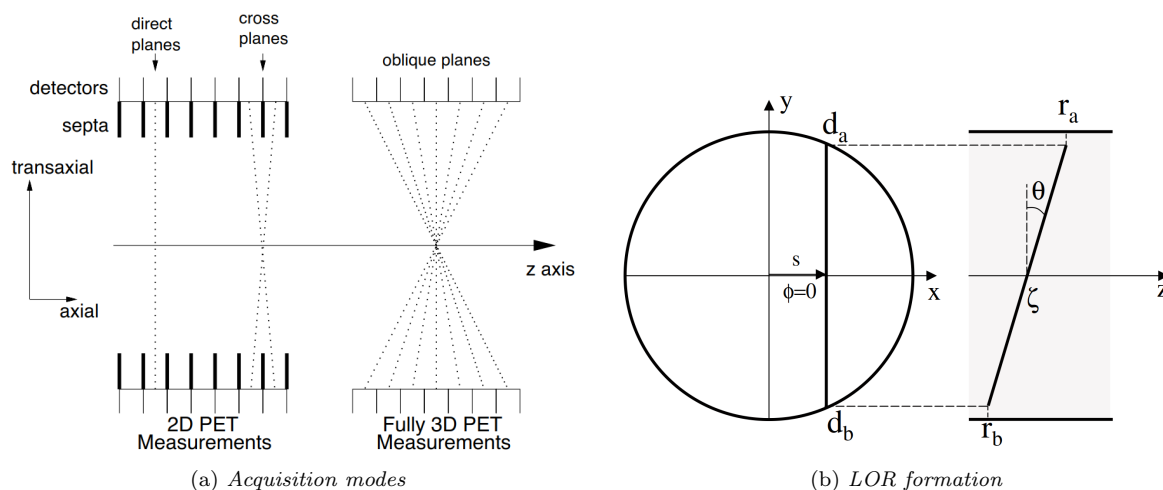

(a) *Acquisition modes*   (b) *LOR formation*

Figure 2.8: *(a) presents the two operation modes of PET systems (2D vs. 3D) and the orientation of direct, cross and oblique planes (from Alessio and Kinahan (2006a)). Formation and orientation of a line-of-response (LOR) in an oblique plane is shown in (b) (from Bailey et al. (2005)).*

Rebinning

As mentioned, 3D reconstruction algorithms are more time-intensive and are more complicated than 2D reconstructions. To reduce the amount of data and to achieve faster reconstructions, methods were developed for rebinning 3D data in a way that it can be reconstructed with 2D algorithms. This brings the advantage of keeping the higher sensitivity of the 3D mode, as all LORs are used in the process, but the reconstruction is reduced to a few independent 2D Radon back transforms. The two approaches that are commonly used are the single slice rebinning (SSRB) and Fourier rebinning (FORE).
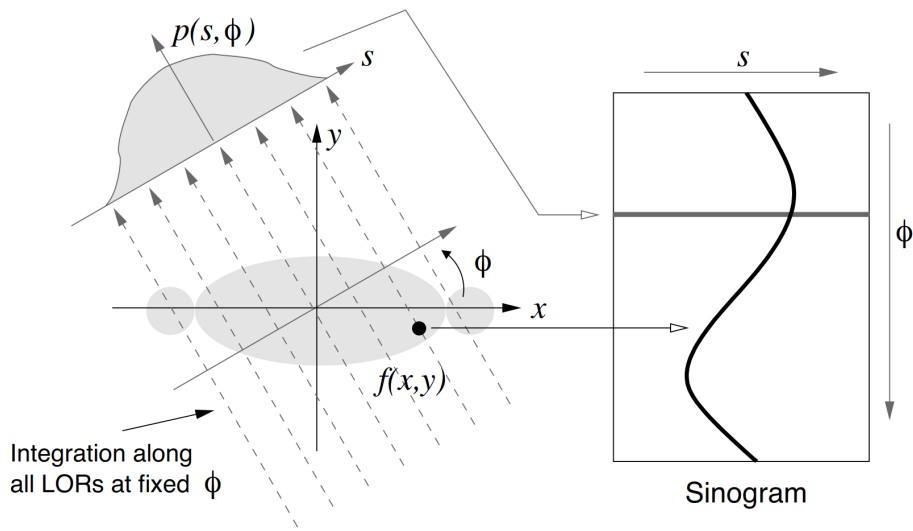
Figure 2.9: *Formation of a projection $p(s,\phi)$ and a sinogram for a point source $f(x,y)$, where ϕ denotes the transaxial angle and s the radial distance from the center of the gantry (from Alessio and Kinahan (2006a)).*

2.3   Image Reconstruction

In tomographic imaging, projections of the actual object (activity distribution in PET) are acquired and stored in convenient forms as sinograms. *Image reconstruction* is the procedure to deduce the activity distribution in image space from the data in projection space. This transformation can either be performed analytically or by using iterative algorithms.

2.3.1   Analytic method

The basis for analytic reconstruction algorithms are the *central section* (or *projection slice*) *theorem*, Radon and Fourier transformations. A Radon transformation converts an object from image space to projection space. The latter is where we get the data of a tomographic scan from. Applying the inverse Radon transformation to our projections, we can in principle obtain the reconstructed image of the object. The central section theorem states that the 1D Fourier transformation of a projection at the angle ϕ is equivalent to the central slice at the same angle ϕ taken from the 2D Fourier transformation of the original image (Hirtl, 2016). Using this theorem and all projection angles ϕ, the image reconstruction reduces to a simple inverse 2D Fourier transformation (Kak and Slaney, 2001). The standard algorithm implementing the analytic approach is filtered backprojection (FBP) (Alessio and Kinahan, 2006a).

2.3.2   Iterative algorithms

Analytic algorithms treat the imaging system as an idealized model, not taking into account errors in the observations. Therefore the solution might be mathematically correct but will lead to streaking artefacts and poorer noise properties (Alessio and Kinahan, 2006a). To account for the noise structure, the intrinsic stochastic of the imaging system has to be estimated or modelled and incorporated into the solution. This adds to the complexity of the mathematical problem requiring iterative methods for solving. Besides the system (*how the image is related to the data*), the image (*discretization of the image*) and the data (*statistical validation of the measurement*) have to be modelled as well before defining the best image (mostly using a Maximum Likelihood approach) and finally adopting an algorithm to find the best image estimate (Bailey et al., 2005). A widely used method for this task is the Ordered Subsets Expectation Maximization (OSEM) method (Hudson and Larkin, 1994) that builds on the Maximum Likelihood Expectation Maximization (ML-EM) algorithm (Dempster et al., 1977; Shepp and Vardi, 1982; Lange and Carson, 1984) described by Figure 2.10. The projections of an initial guess of the image are calculated and compared to the measured projections. Each measured projection is now weighted with the forward projected guess to form a correction factor in the projection domain. Back-projecting delivers the correction factor in the image domain, which has to be weighted voxel-wise with the system matrix. This value serves as the new image estimate for the next iteration. As with each iteration one forward and one back-projection have to be performed, computation time can be substantially longer than for FBP.

For the improved Ordered Subsets Expectation Maximization (OSEM) algorithm the projections are divided into B subsets. The back-projecting and weighting are performed separately for each subset, which means that for the same computational effort the image is updated B times before entering the next iteration. An OSEM method reaches a similar solution B times faster than the corresponding ML-EM.

As a further improvement, *resolution modeling* using the point spread function (PSF) of the system (Figure 2.11) can been incorporated into the reconstruction algorithm (Panin et al., 2006). The PSF describes the response of the imaging system to a point source, which can be found by analytic modeling, by Monte-Carlo simulations or by measurements with a line- or point-source (Leahy and Qi, 2000).
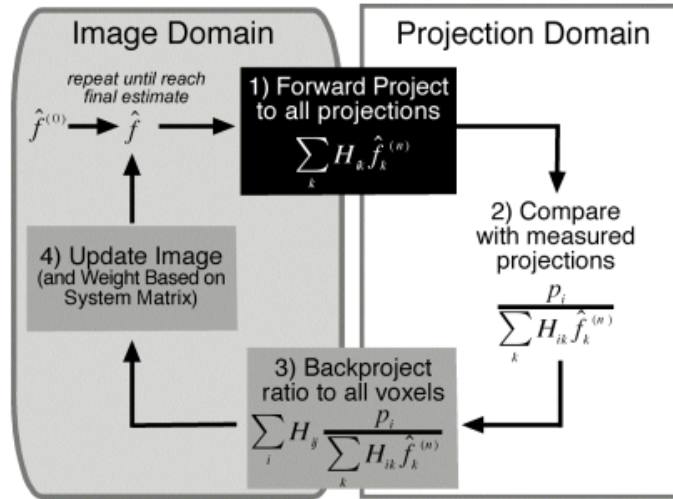
Figure 2.10: *Flow diagram of the maximum likelihood - expectation maximization (ML-EM) algorithm (from Alessio and Kinahan (2006a)).* $\hat{f}$ *is the activity distribution in image space,* $\hat{f}^0$ *the initial guess,* H_{ik} *the projection kernel and* p_i *the image in projection space.*
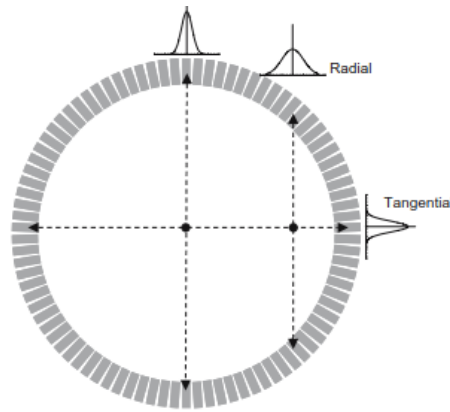

Figure 2.11: *The system response to a point source for a ring detector (point spread functions) can be used to model and improve the resolution (from (Bailey et al., 2005)).*

The incorporation of the PSF within the reconstruction algorithm can improve image resolution and contrast, but can affect noise negatively and produce edge artefacts (Rahmim et al., 2013). Iterative reconstruction methods based on maximum likelihood estimation maximization often produce unrealistic and noisy results.

Regularization is the introduction of additional information as smoothness, continuity or finite band limits to the reconstruction process. It penalizes unacceptable solutions and hence leads to improved image quantification (Magdics et al., 2011). As a further step of regularizations, anatomical information from other imaging modalities can be incorporated into the reconstruction process, improving resolution and noise properties significantly (Alessio and Kinahan, 2006b). For the use of these *anatomical priors*, CT proved less valuable due to poorer contrast in soft tissue than MRI (Bai et al., 2013b). Further improvements in image quality were achieved with time-of-flight systems (TOF), providing higher sensitivity as well as reduced scattered and random events (Vandenberghe et al., 2016).

2.4 Quantification in PET

In order to obtain quantitative measures in PET imaging, precise and complete corrections for the physical effects and the systematic reductions of signal have to be performed (Subsection 2.4.1). Subsection 2.4.2 then describes parameters for measuring performance of PET systems and image quality.

2.4.1 Data Corrections

Correction methods for the most common sources of quantification errors are presented below.

Attenuation correction

The interactions described in Subsection 2.1.3 reduce the number of events received by the detector, depending on the density and distribution of matter in the field-of-view (FOV). Attenuation correction maps (μ-maps) are mostly acquired by transmission scanning, computed tomography (CT) or magnetic resonance imaging (MRI) (Zaidi and Hasegawa, 2003). Transmission scans measure the photon attenuation directly by using sources that emit photons at similar energies to the annihilation photons (Bailey, 1998). Computer tomography (CT) scans measure the attenuation of X-rays which can be extrapolated to the desired $511 \, \text{keV}$ attenuation (Kinahan et al., 1998; Ziegler et al., 2015). CT-based μ-maps have advantages over traditional transmission scans, including faster scan time and better resolution. Minor problems present the translation from Hounsfield units to attenuation values, adapting image resolutions and the scaling of the attenuation from X-rays to annihilation photons.

As MRI measures the proton density and relaxation properties, the translation of these values to photon attenuation is far from trivial and still presents severe problems in the implementation. A major error in the attenuation maps of PET/MR derives from tissue inversion, or tissue swap, where the classification of water and fat is incorrectly performed in the MR images. As the PET μ-maps are mostly derived from water and fat images of MRI, misclassified tissues can lead to significant errors in the attenuation correction and further in the quantification of PET images (Ladefoged et al., 2014). Another big issue is the segmentation of bone in MR. As bone lacks signal in MRI, it is classified as soft tissue and accordingly not considered in the attenuation correction which further hampers the accuracy of MR-based attenuation correction. Although several methods have been proposed for improving the signal and segmentation of bone in MRI (atlas-based AC, ultrashort echo time sequences, Dixon-based sequences), it still has its limitations (Boellaard and Quick, 2015). Similarly to bone, air in the lungs lacks signal and deteriorates accuracy of attenuation correction in the thorax ("lung artefacts"). The limited FOV of MRI implies truncation of images, which causes notable artefacts in body imaging and in attenuation correction for PET. Further, smallest differences in magnetic susceptibility of PET scanner components can cause artefacts ("susceptibility artefacts") in the resulting images (Vandenberghe and Marsden, 2015). All together, these factors still lead to unresolved imprecisions in the MRI-based attenuation maps. For a thorough review of the mentioned issues in PET/MR imaging, the reader is referred to Boellaard and Quick (2015). Compared to CT-derived μ-maps, a major advantage of MR-based attenuation correction is better segmentation of soft tissue and substantial reduction of radiation exposure to the patient (Jadvar and Colletti, 2014).

Scatter correction

The various characteristics of scattered events in the PET data have led to a variety of approaches for scatter estimation and scatter correction. The calculated corrections can either be subtracted from the sinogram data or be implemented as an additive term in the model of the system (see Section 2.3). Four main categories can be identified which are based on empirical corrections, multiple energy windows, convolution and deconvolution, or analytical and Monte Carlo simulations (Bailey et al., 2005). The most

used method for scatter correction is the *Single Scatter Simulation*, which requires an initial estimate of the scatter-free distribution and an accurate μ-map.

Randoms correction

Randoms introduce a uniform background signal that reduces the image contrast. As already described, the number of randoms can be estimated from the singles rate and the coincidence time window. Another even more common way to correct for randoms is the delayed window method. The signals of one detector are delayed relative to the other detector by a time bigger than the coincidence time window. All detected coincidences that arise from this detector pairing are truly unrelated and give an estimation of the number of randoms. Equally as in the scatter correction, the estimation is either subtracted from the prompts or incorporated into the system model of the iterative reconstruction algorithm.

Normalization

Due to physical differences in the detectors (gain, accuracy,...), the sensitivity is slightly different for all detector pairings. To account for these deviations, a uniform activity concentration that exposes all detectors equally is measured and each detector pair accordingly is normalized by its respective count rate.

Decay correction

During the duration of a study, the activity decreases and hence in longer studies, the later signals would have less effect on the result than the signals from early in the measurement. This requires the scaling of all data points with a decay correction factor especially necessary in dynamic studies.

Correction for dead time

Dead time corrections can either be realized by so-called live time measurements or by modelling the dead time effects into a paralyzable and a non-paralyzable component.

Partial volume correction

Partial volume effect combines to effects that degrade image quantification, especially in small lesions. First, due to limited spatial resolution of the imaging system, the resulting 3D images are blurred. This causes higher activities to spread to neighbouring regions and introduces a reduction of the maximum activity, as can be seen in Figure 2.12. The second effect is caused by the image sampling to a voxel grid. The edges of the activity distribution do not match the borders of the voxels, hence the voxels at the edges combine activity measurements of both, lesion and background. PVE depends on various factors, as lesion size, contrast, spatial resolution, sampling size and others. Various methods have been proposed to correct for PVE, but still PVE is not implemented in the clinical routine (Erlandsson et al., 2012).

2.4.2 Image Quantification

Qualitative interpretation in clinical oncology has widely been replaced by quantitative measurements of image factors, especially for inherently quantitative imaging modalities as PET (Bai et al., 2013a). Hence, the performance of PET systems has to be accurate and reproducible, and, amongst others, is usually described by the following parameters:

Sensitivity   The sensitivity of a scanner describes the relation between total amount of measured true coincidences to the total amount of activity in the FOV of the scanner. Simply spoken, sensitivity describes a scanners ability to correctly quantify a specified amount of activity in the FOV. Apparently, sensitivity crucially depends on the scanner geometries,
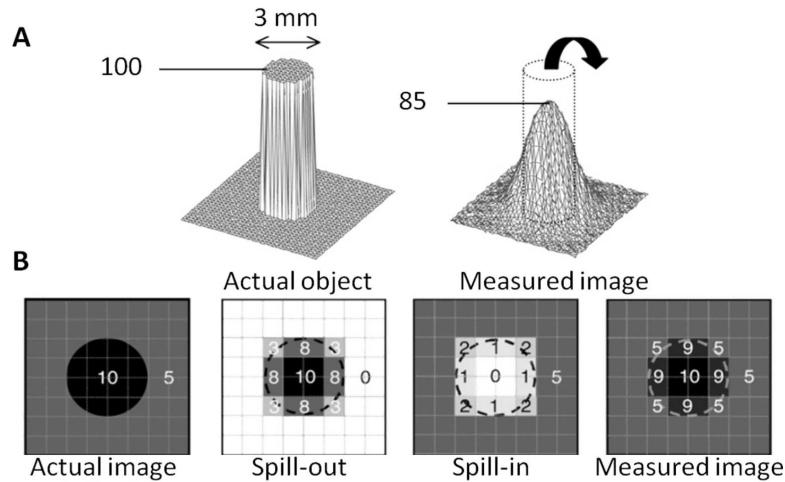
Figure 2.12: *Illustration of partial volume effect. A circular source in a non-active background results in a decreased maximum with smeared out distribution (A). Both effects, spill out and spill in, contribute to the measured image (B) (adapted from Soret et al. (2007)).*

but detection efficiency, dead time and detector properties play a main role as well. Sensitivity is given in $cps/$(Bqml), where cps is counts per second. Higher sensitivity generally translates to decrease in noise and higher quantification accuracy due to higher number of counts in the images (see Subsection 4.1.4).

Scatter fraction The scatter fraction is another important measure for the performance of a PET scanner, describing the fraction of scattered events within the energy window. Scattered events reduce the image contrast by adding a constant background level to the images. The scatter fraction is not solely determined by the patient but scanner, detector and gantry geometry and properties can be optimized as well.

Noise equivalent count (NEC) rate The noise equivalent count (NEC) rate indicates how well a scanner is able to process a given number of prompts. At its extremum, an optimum between dead time losses, random coincidence counts and image noise is found. One of the several ways to formulate the NEC rate is:

$$NEC = \frac{T^2}{T + S + R} \qquad (2.10)$$

where T, S and R are the true, scatter and random coincidence rates, respectively.

In PET, we literally count a physical quantity, the number of radioactive decays. After correction for physical degradation factors as mentioned above, we obtain absolute quantitative measurements of the tumor uptake in $\mathrm{Bq\,ml^{-1}}$. In clinical practice, quantification additionally often refers to physiological meaningful parameters received via transformation of the absolute activity measures, opposed to *semi-quantification* where "relative measurements are compared to a disease-free or receptor-void region" (Zaidi, 2006). Several measures for image quality are commonly applied:

Spatial resolution is the smallest distance between two point sources that allows them to be separated from each other in the reconstructed image. It usually is given as the full-width-at-half-maximum (FWHM) of a point source and is inherently limited by the positron range and the noncollinearity.

Image contrast is the ratio between uptake in a lesion and the background, and it rates the separability of a lesion from the background.

Image noise   is often defined as the coefficient of variation (or relative standard deviation) to easily assess homogeneity in the image.

Signal-to-noise ratio (SNR)   relates the uptake in a lesion to the noise in the image, another indicator for the detectability of lesions in an image.

Recovery coefficient (RC)   defines the recovered contrast in the image compared to the true contrast (in phantom studies).

Standard uptake value (SUV)   are commonly used for quantification in oncology imaging with a central role in controlling response to therapy by "removing variability introduced by difference in patient size and the amount of injected" activity (Kinahan and Fletcher, 2010).

Several factors (partial volume effect, noise, acquisition time,...) influence not only image quality, which in most cases is the main method in clinical assessment, but predominantly quantification accuracy.

2.5   Evolution of PET

In this section a short overview of the historical developments contributing to PET will be given before describing current system setups and essential radiopharmaceuticals used in clinical routine.

2.5.1   PET systems

The technological innovations that led to the evolution of PET scanners were synergistically accompanied by the development of suitable radiotracers (Portnow et al., 2013). A vast number of people similarly contributed to the various technologies of PET imaging, just a few pioneers and the cornerstones of PET development shall be mentioned here.

After invention of scintiscanners in the 1950s, several developments in image reconstruction and research in tracer extraction (Nutt, 2002), the first PET scanner for human studies was developed in the 1970s by Phelps and colleagues (Phelps et al., 1975; Ter-Pogossian et al., 1975).

Stand-alone PET systems   Til the 90s, the development was marked by the first synthesis of FDG, the discovery of bismuth-germanate (BGO) as ideal material for scintillators, the development of block detectors and first availability of medical cyclotrons for PET (Nutt, 2002). To that date, all PET scanners were stand-alone devices, admittedly providing good functional images but lacking anatomical information. Therefore, separate computed tomography (CT) or magnetic resonance imaging (MRI) scans were performed for the acquisition of anatomical images, mostly including movement of the patient and temporary delay between scans. This led to the huge draw-back of the difficult co-registration of two separate acquisitions.

PET/CT systems   This draw-back was solved by the invention of dual-modality PET/CT devices by Beyer et al. (2000), which were incorporated into the market shortly after. Such a hybrid scan consists of two CT-scans and a PET scan, the first CT to create an attenuation correction map and the second for anatomical imaging (Beyer et al., 2004). These systems had the advantage of increasing image quality, minimizing errors in the co-registration and shortening the scan-procedure for patients, with the disadvantage of exposing the patient to significantly more radiation than in the separate scans (Huang et al., 2010). Due to the fast first transmission scan, respiratory motion manifests differently in the attenuation image (CT) and the PET image (Beyer et al., 2011b). Further developments in PET/CT, as the introduction of time-of-flight capability and reconstruction algorithms with resolution recovery

(PSF), improved image quality and quantification of these hybrid systems significantly (Akamatsu et al., 2012). Although initially introduced in the early days of PET, time-of-flight (TOF) capable PET systems reached their full potential just in recent years. TOF PET scanners make use of the time difference at the arrival of two coincidence photons, achieving higher sensitivity, spatial resolution, signal-to-noise ratio and lesion contrast together with lower image noise (Surti, 2015).

PET/MR systems   Recently, PET/MR hybrid systems combining the PET and MR scan were introduced (Schlemmer et al., 2008), reducing the radiation for the patient to solely the PET part and improving the contrast in soft tissue (Beyer et al., 2011a). Combining PET and MR was long limited by the sensitivity of the photomultiplier tubes (PMTs) to magnetic fields, which was overcome by the development of silicon photomultipliers (SiPMs) and avalanche photodiodes (APDs) (Lecomte, 2009). A remaining challenge is the correct transformation of the proton density measured by MRI to the linear attenuation coefficients of the 511 keV photons in PET (Beyer et al., 2008). The problematic issues of attenuation correction in PET/MR, as mentioned in Section 2.4, still translate to notable imprecisions of quantification accuracy in PET images. Due to low timing resolution of APDs, TOF capability is not possible in APD-based PET/MR systems. However, with the development of SiPM detectors the necessary timing resolution was achieved (Lewellen, 2008), allowing for first TOF capable PET/MR scanners (Grant et al., 2016).

Despite their big advantages in functional imaging, all the mentioned PET systems depend on the availability of medically usable tracers with radioisotopes of short half-lives. Those have mostly to be produced by expensive on-site cyclotrons which eventually holds back the faster expansion of PET systems (Muehllehner and Karp, 2006). In most recent attempts, state-of-the-art PET/CT could be replaced by functional whole-body diffusion-weighted MRI for cancer staging in children and young adults, showing a promising detectability rate by solely using radiation-free contrast agents (Klenk et al., 2014).

2.5.2   Radiopharmaceuticals / PET tracers

As seen in Subsection 2.1.1, just a few radionuclides have the adequate chemical and physical properties which make them suitable for in vivo biochemical and physiological studies. The main requirements to make a radioisotope suitable for PET imaging are: it must be easy to incorporate into molecules that participate in metabolic processes and it must have a relatively short half-life to significantly reduce radiation exposure to the patient and to clinical staff handling the radionuclides.

The diagnostic output of a PET scan is strongly dependent on the availability of differentiated radiopharmaceuticals that address specific biochemical processes or cover a wide range of applications (Bailey et al., 2005). These range from simple diffusion in blood to measure its flow, to generally tracking metabolism rates. For a short selection of clinical applications of PET with the according tracers, see Table 2.2.

FDG   The widest spread and most universal radiopharmaceutical not only for applications in oncology, is ^{18}F-FDG (2-deoxy-2-[^{18}F]fluoro-D-glucose). It is accumulated in the tissue via the glucose metabolism, relating the amount of FDG closely to the metabolic activity of tissue (Boellaard et al., 2015). Many types of cancer cells have increased glucose uptake compared to their surroundings, which is indicated by higher concentration of FDG (Bailey et al., 2005).

DOTANOC ^{68}Ga − DOTANOC is a ^{68}Ga-labelled analogue of somatostatin, which is expressed on neuroendocrine tumors (NET) and several types of intracranial tumors, as meningiomas, carcinoids,

Table 2.2: *PET radiotracers in clinical application (reproduced with permission from Cal González (2014))*

Radionuclide	Tracer compound	Physiological process	Typical application
^{18}F	Fluoro-deoxy-glucose (FDG)	glucose metabolism	oncology, neurology and cardiology
^{18}F	[^{18}F]Fluoride ion	bone metabolism	oncology
^{18}F	[^{18}F]FMISO, [^{18}F]FETA	tumor hypoxia	oncology - response to radiotherapy
^{18}F	[^{18}F]FHBG	gene therapy	gene expression
^{11}C	[^{11}C]Choline	choline metabolism	oncology
^{11}C	[^{11}C]Methionine	protein synthesis	oncology
^{11}C	[^{11}C]Flumazenil	benzodiazepine receptor antagonist	neurology
^{13}N	[^{13}N]Ammonia	blood perfusion	myocardial perfusion
^{18}O	[^{18}O]Carbon Dioxide, [^{18}O]Water	blood perfusion	brain activation estudies
^{68}Ga	^{68}Ga-DOTATOC, ^{68}Ga-DOTATATE, ^{68}Ga-DOTANOC	receptor binding SSRT	neuroendocrine tumors
^{82}Rb	^{82}Rb-rubidium chloride	blood perfusion	myocardial perfusion
^{124}I	[^{124}I]MIBG, [^{124}I]IAZA, [^{124}I]IAZG	tumor hypoxia	oncology - response to radiotherapy

gliomas and secondary tumors of NET, and shows physiologic uptake in the pituitary gland (Kagna et al., 2014; Sharma et al., 2013).

FET ^{18}F-fluoro-ethyl-tyrosine (^{18}F − FET) is an amino acid analogue labelled with ^{18}F and is actively taken up by tumor cells with high metabolism. Its main use is for evaluating patients with primary brain tumors of all grades and types, as gliomas and meningiomas (Dunet et al., 2012; Cornelius et al., 2014).

Chapter 3

Materials and Methods

In Section 3.1 first the specifications of the PET/MR system used for all acquisitions will be given. Section 3.2 describes the NEMA IQ phantom, how data was acquired and which figures of merit were chosen. Analogously, Section 3.3 presents choice of patient data, post-processing steps and definition of figures of merit for patient evaluation. The statistical analysis applied to the measures can finally be found in Section 3.4.

3.1 PET/MR System

The data acquisition was performed on a Siemens Biograph mMR, an integrated whole-body PET/MR hybrid system, located at Allgemeines Krankenhaus (AKH) Wien (see Figure 3.1). Specifications of the Biograph mMR are summarized in Table 3.1. The PET component of the Biograph mMR consists of 8 detector rings of 56 detector blocks each, or 448 detector blocks in total. The individual detector blocks contain 8×8 crystal elements with 3×3 avalanche photodiodes (APD) per block attached for readout. Single crystal elements are $4\,\mathrm{mm} \times 4\,\mathrm{mm} \times 20\,\mathrm{mm}$ in size with cerium-doped lutetium oxyorthosilicate (LSO) as scintillation material. The scanner totals 64 crystal rings with 448 crystal elements per ring and axial spacing of $0.406\,\mathrm{mm}$. The PET component of the Biograph mMR provides an axial and radial field of view (FOV) of $258\,\mathrm{mm}$ and $588\,\mathrm{mm}$, respectively. The energy window is set to 430-610 keV and the coincidence time window to $5.86\,\mathrm{ns}$. The manufacturer states the results of NEMA 2007 measurements for transverse spatial resolution as $13.2\,/(\mathrm{s\,kBq})$ for sensitivity, $1.75 \times 10^5\,/\,\mathrm{s}$ for peak noise-equivalent-count (NEC) rate at an activity concentration of $21.8\,\mathrm{kBq\,ml^{-1}}$ and $4.4\,\mathrm{mm}$ for the FWHM at $1\,\mathrm{cm}$ (Siemens, 2016).

The MR component of the Biograph mMR consists of a $3\,\mathrm{T}$ niobium-titanium superconductor magnet, a whole-body gradient coil system of $45\,\mathrm{mT\,m^{-1}}$ at $200\,\mathrm{T\,m^{-1}\,s^{-1}}$ and a radiofrequency body coil with peak power of $35\,\mathrm{kW}$ and transmitter bandwidth of $800\,\mathrm{kHz}$ (Delso et al., 2011). Its FOV is between $0.5\,\mathrm{cm}$ and $50\,\mathrm{cm}$ with a 2D slice thickness from 0.1-200 mm and a 3D slab thickness from 5-500 mm, and a maximum resolution of $9\,\mathrm{\mu m}$ (Delso et al., 2011).

Figure 3.1: *Siemens Biograph mMR at Allgemeines Krankenhaus Wien (courtesy of Andreas Renner).*

Table 3.1: *Specifications of the Siemens Biograph mMR (from Delso et al. (2011))*

MR component		
Magnet		$3\,\mathrm{T}$
Gradient coil: strength		$45\,\mathrm{mT\,m^{-1}}$
Gradient coil: slew rate		$200\,\mathrm{mT\,m^{-1}\,s^{-1}}$
Radiofrequency coil: peak power		$35\,\mathrm{kW}$
Radiofrequency coil: transmitter bandwidth		$800\,\mathrm{kHz}$
PET component		
Detector rings		8
Axial spacing		0.40625mm
Detector blocks (per detector ring)		56
Crystal elements (per detector block)		8x8
Size of crystal elements [mmxmmxmm]		4x4x20
Avalanche photodiodes (per detector block)		3x3
Axial FOV [mm]		258
NEMA NU 2-2007 protocol	Manufacturer*	Delso et al. (2011)
Transverse spatial resolution FWHM at 1 cm [mm]	4.5	4.3
Sensitivity [cps/kBq]	13.2	13.8
Peak NEC rate (at $21.8\,\mathrm{kBq\,ml^{-1}}$) [kcps]	175	179

*from Siemens (2016)

3.2 Phantom Methodology

3.2.1 Body Phantom

A NEMA Body Phantom as described by the National Electrical Manufacturers Association (NEMA) NU 2-2012 standards for Image Quality (National Electrical Manufacturers Association, 2013) was used for the evaluations performed in this work. As demonstrated in Figure 3.2, the phantom shall represent a human torso with a length of 180 mm. Further description of the phantom can be found elsewhere (International Electrotechnical Comission, 2013). Housing and cap are made of acrylic glass with wall thickness of 3 mm and 10-20 mm, respectively. The lung insert, a cylindrical insert with 50 mm outside diameter and wall thickness of 4 mm, could be filled with Styrofoam to simulate the attenuation of the lung but was left empty. A second insert holds six glass spheres with inner diameters between 10 mm and 37 mm (for more details see Table 3.2) and wall thickness of 1 mm or less. Ideally all spheres are centered to the slice 70 mm from the top of the phantom allocated equidistantly on a circle of 72.2 mm in radius (see Figure 3.2). The background (BG) of the body phantom and all six spheres were filled with different concentrations of ^{18}F-FDG yielding a true lesion-to-background ratio (LBR_{true}) of 4.065 : 1. For this purpose, a total activity of 101.6 MBq was injected into the water-filled background compartment 40 min before acquisition start, giving an activity concentration of 5.676 kBq mL^{-1} at acquisition start. Similarly, 35 min before acquisition start the six spheres were filled with activity to meet an activity concentration of 23.07 kBq mL^{-1} at start of acquisition.

Table 3.2: *Specifications of the NEMA IEC Body Phantom*

|	Diameter [mm]	VOL_{true} [cm^3]	Activity concentration [kBq mL^{-1}]	Total activity [kBq]
background (BG)	-	9550	5.676	54 200
sphere 1	37	26.5	23.07	612
sphere 2	28	11.5	23.07	265
sphere 3	22	5.58	23.07	129
sphere 4	17	2.57	23.07	59.3
sphere 5	13	1.15	23.07	26.5
sphere 6	10	0.524	23.07	12.1

Note: Activity concentrations are given at start of acquisition. VOL_{true} is the actual sphere volume.

3.2.2 Data Acquisition

Data was acquired in 3D-mode of a one bed position list mode scan with 20 min duration. Attenuation correction was performed using the standard CT-based template provided by the manufacturer. Slight deviations of two spheres (13 mm and 22 mm) in the actual setup to the template were observed, as shown in Figure 3.5. Reconstructions were performed directly at the scanner by using the clinical software. An OP-OSEM (3D Ordinary Poisson Ordered-Subset-Expectation-Maximization) algorithm with 4 iterations and 21 subsets was used for reconstruction. Pixel size in the slices was set to 2.086 mm × 2.086 mm with 2.031 mm slice thickness, giving an image matrix of 344 × 344 with a voxel volume $V_{\text{voxel}} = 8.84 mm^3$. Two separate reconstruction settings were applied, one with a Gaussian post-filtering of 5 mm full-width-half-maximum (FWHM) referred to as OSEM (Hudson and Larkin, 1994) and the other with a point spread function for resolution modelling of the system but without post-filtering, referred to as PSF (Panin et al., 2006). These reconstruction settings were chosen to compare images with two fundamentally different noise behaviours. The post-filtering in OSEM smoothes the images to reach an appearance similar to clinical applications, while with PSF the images are significantly noisier but offer better resolution. For details of the reconstruction settings, see Section 2.3.
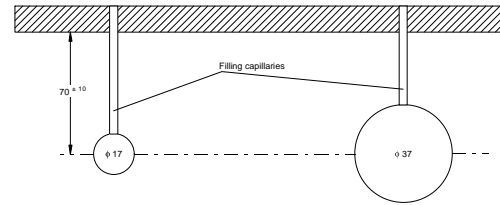
(a) *Body phantom*
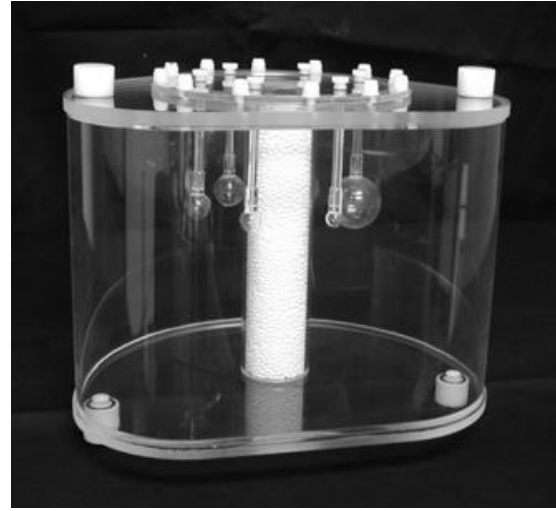
(b) *Sphere insert*
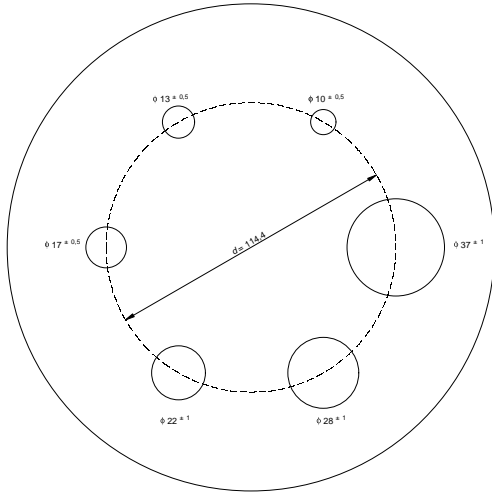
(c) *Schematic transverse section*

(d) *Schematic longitudinal section*

Figure 3.2: *The NEMA Body Phantom used for the measurements, showing the whole phantom (a), the insert with the six spheres (b) (from El-se.com (2016)) and schematics of the cross sections with measures of the phantom, (c) and (d) (from NEMA (2001)).*

To simulate shorter acquisitions, the 20 min list mode data was split up into consecutive images of the same length, the *frames* or *realizations* of one acquisition time, see Figure 3.3.

All frames of the mentioned configurations were reconstructed using both OSEM and PSF algorithms. The longest acquisition, the *reference frame*, was regarded the golden standard for evaluation of image quality. Absolute values of the figures of merit (SNR, noise, ...) strongly depend on fixed reconstruction parameters as iterations, filtering, etc. Therefore, the changes in image quality with reduced acquisition time were evaluated relative to the reference frame.

Regions Of Interest - ROIs

A *Region Of Interest* (ROI) defines a region that is considered for evaluation and the segmentation algorithm. For each ROI, an individual maximum voxel value is located.

Centered on each sphere, one ROI was placed to evaluate different regions in the image separately, see Figure 3.4. The ROIs consist of a substantially bigger volume than the actual sphere to enclose all relevant higher activity, including spillover. These ROIs serve as the basic regions for the automatic segmentation algorithm and are marked as yellow contour lines in Figure 3.4.
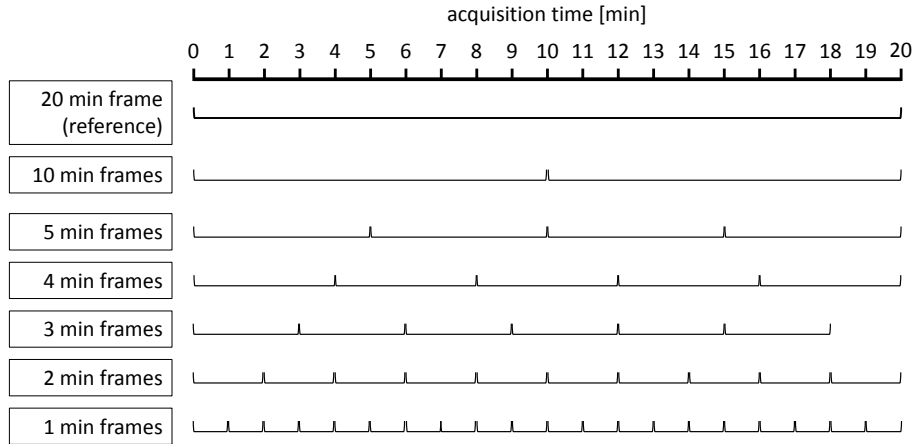
Figure 3.3: *Schematic for frame composition in the phantom study. As shown for the phantom analysis, the* 20 min *list-mode data (reference frame) was split into* 10 min, 5 min, 4 min, 3 min, 2 min *and* 1 min *frames. For the patient studies included in this work (see Subsection 3.2.2), the* 10 min *list-mode data was similarly split into frames of* 5 min, 3 min, 2 min, 1 min *and* 30 s *length.*

Additional spherical ROIs were placed centric around each sphere. These ROIs are of the exact same size as the spheres, reproducing the true boundaries of the spheres in the images. This so-called *geometric segmentation* delivers the mean activity concentration a_{mean}, marked as green masks in Figure 3.4.

For the evaluation of the background distribution, six cylindrical regions of interest (ROI) with $R = 25$ mm and $H = 40$ mm were placed in different locations of the background, as shown by the white contours in Figure 3.4.

The segmentation and the calculation of figures of merit in Subsection 3.2.3 is limited to the voxels within the mentioned ROIs.

The actual setup of the phantom shows deviations from the ideal positions for the 13 mm and 22 mm spheres, as indicated in Figure 3.5. These misalignments affect the quantitative results for the two mentioned spheres so reproducibility might not be guaranteed with an other phantom.
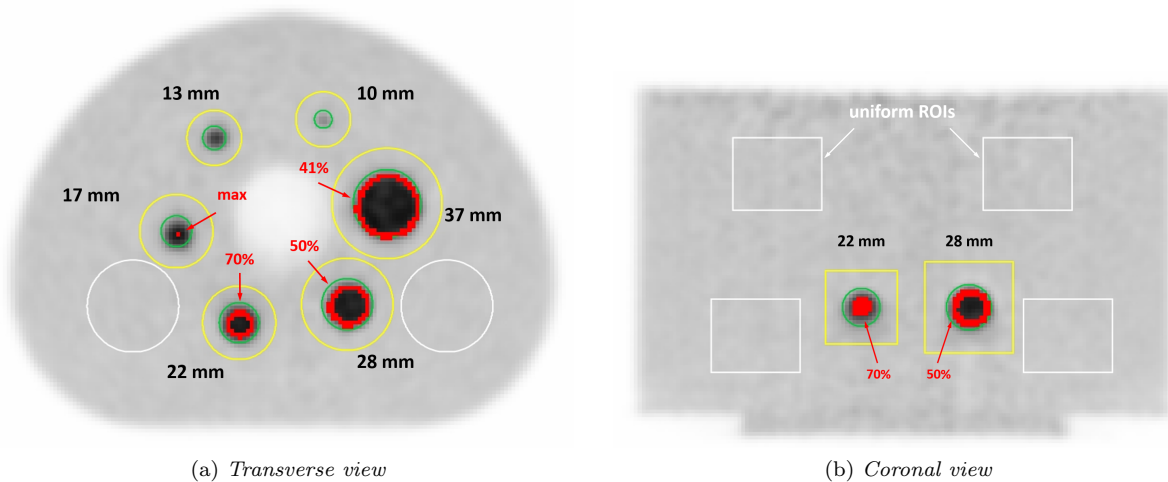

(a) *Transverse view*

(b) *Coronal view*

Figure 3.4: *Position of the regions of interest in the transverse and the coronal view of an exemplary phantom image (*20 min *frame length with* **OSEM** *reconstruction). Spheres are labelled with their diameter. Following ROIs are visible in the transverse view: cylindrical background-ROIs (* white*), cylindrical ROIs for calculation and the general segmentation algorithm (* yellow*), spherical ROIs for calculation of* RC_{mean} *(*green*) and iso-contours (*red*). Starting from the single red dot, the iso-contours mark counter-clockwisely: maximum voxel value,* 70 %, 50 % *and* 41 % *thresholds of the individual sphere.*

27

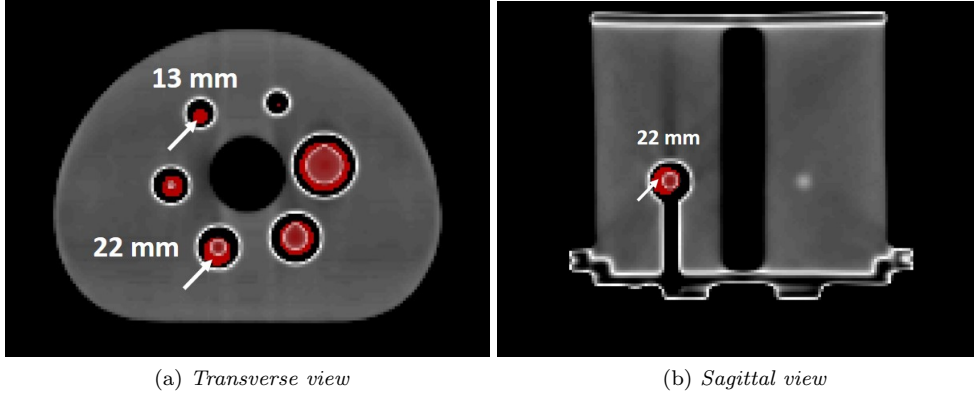(a) *Transverse view*   (b) *Sagittal view*

Figure 3.5: *Misalignment for two spheres (13 mm and 22 mm diameter) between the actual phantom setup and the CT-based attenuation correction map is shown by merging an exemplary image (20 min OSEM image, color scale) with the μ-map of the manufacturer (gray-scale). Red regions mark voxels with activities above a fixed threshold (12.2 kBq ml⁻¹) as an indicator for the location of the spheres. The arrows point to spheres where significant spatial deviations were found.*

Segmentation algorithm

To segment regions of higher activity, a threshold-based segmentation method that accounts for the background activity (Boellaard et al., 2015) was chosen. (Firouzian et al., 2014) showed the suitability of adaptive thresholds for our purpose. In-house software was adapted to this method.

Voxels are considered part of the emitting volume when their activity value is equal or higher than an absolute threshold $[\mathrm{kBq\,ml^{-1}}]$

$$T_{\mathrm{t}} = (a_{\max} - a_{\mathrm{BG}}) \cdot t \tag{3.1}$$

where $a_{\max}$ and a_{BG} are maximum and average background values in the image, respectively. t denotes the threshold in percent, which was chosen as 41 %, 50 % and 70 %. For each threshold, the segmented voxels form a volume, the volume of interest (VOI), that is used for the calculation of the figures of merit. The thresholds T_{t} are based on the respective $a_{\max}$ of each ROI. In Figure 3.4, the red isocontours show T_{41}, T_{50}, T_{70} and $a_{\max}$ of 37 mm, 28 mm, 22 mm and 17 mm spheres, respectively.

3.2.3   Figures of Merit

PET image quality of the phantom measurements was analysed by means of the following figures of merit:

Recovery Coefficient (RC)

The RC, or sometimes called contrast recovery, is defined as the measured activity concentration in a given hot lesion divided by the actually administered activity concentration in this region. In this work, the RC of a considered volume of interest (VOI) was calculated as:

$$RC_{voi} = \left(\frac{frac a_{voi} a_{\mathrm{BG}}}{r_{\mathrm{adm}}} \right) \tag{3.2}$$

where the lesion-to-background ratio (LBR) of the average activity concentration in the considered VOI a_{voi} and the mean activity concentration in the background a_{BG} is divided by $r_{\mathrm{adm}} = A_H/A_{BG}$, which is the ratio of the administered activity concentrations in the hot spheres A_H and the background A_{BG}. RCs compare and normalize the measured activity concentration ratio in the images to the actual administered ratios. For each sphere, RC was calculated for the maximum voxel value and the mentioned segmented volumes, indexed with the according threshold: $RC_{\max}$, RC_{mean}, RC_{41}, RC_{50} and RC_{70}.

With ideal acquisition and reconstruction, the RC of all spheres should equal 1. Higher values imply a bigger difference between sphere and background activities in the image, which can originate form an under- or overestimation in the background or the sphere, respectively. $(1 - RC_{\mathrm{mean}})$ directly relates to the amount of spill-out (partial volume effect).

Background Activity Concentration (a_{BG})

The background activity concentration a_{BG} is the mean activity concentration measured on average in the six background (BG) ROIs.

Background Variability (N_{BG})

The background variability N_{BG} describes the *image noise* in form of the relative standard deviation (RSD), or coefficient of variation (CV), and is calculated as

$$N_{\mathrm{BG}} = \frac{\sigma_j}{a_{\mathrm{BG}}} \cdot 100\,\% \tag{3.3}$$

where $\sigma_j = \sqrt{\frac{\sum_{i=1}^n (b_i - a_{\mathrm{BG}})^2}{n}}$ is the standard deviation of all n voxels b_i in the BG-ROI j and a_{BG} is their average. N_{BG} is averaged over the six BG-ROIs.

Segmented Volumes at $41\,\%$, $50\,\%$ and $70\,\%$ (VOL_{41} , VOL_{50} , VOL_{70})

For each sphere, the segmentation algorithm yields three segmented volumes VOL_{41}, VOL_{50} and VOL_{70} for the respective threshold parameter $t = 41\,\%$, $50\,\%$ and $70\,\%$ in Equation 3.1. These volumes correspond to the number of voxels with higher or equal activity concentrations than the threshold values T_{t}, times the voxel volume VOL_{voxel}. This is done independently for each sphere in one image.

Lesion-to-Background Ratio (LBR)

In clinical science, the expression *lesion-to-background ratio*

$$LBR_i = \frac{a_{\mathrm{seg}}}{a_{\mathrm{BG}}} \tag{3.4}$$

is often used synonymously for *contrast*, where a_{seg} is either the maximum activity concentration (seg = max) in the ROI, the mean within the spherical ROI (seg = mean) or a segmented volume (seg = $\{41; 50; 70\}$). In a perfectly acquired, noiseless image of a phantom-experiment, we should find an image contrast equal to the administered activity ratio and an RC value of 1.

Signal-to-Noise Ratio (SNR)

The *signal-to-noise ratio* (SNR) is calculated as

$$SNR_{\mathrm{seg}} = \frac{\overline{a}_{\mathrm{seg}}}{N_{\mathrm{BG}}} \tag{3.5}$$

where $\overline{a}_{\mathrm{seg}}$ is the average activity concentration in the according segmented volume VOL_{seg}.

3.3 Patient Methodology

Once the phantom experiments were performed, the next step in the project was to evaluate how the frame time would affect the quantitative accuracy of patients with brain tumors.

3.3.1 Patient Selection

The study included a total of 24 patients which underwent clinical PET/MR brain studies for staging or restaging of brain tumors between September 2014 and June 2016. The visual assessment of the reconstructed PET data revealed 7 primary and 9 recurring tumors in the ^{18}F − FET patients, and 7 meningeal tumor formations in ^{68}Ga − DOTANOC scans. 1 negative ^{68}Ga − DOTANOC scan was included for consideration of the pituitary gland. Patient weight averaged 76(10) kg and 78(18) kg for ^{68}Ga − DOTANOC and ^{18}F − FET, respectively, ranging totally between 42 kg and 117 kg. For further details regarding patient data, see Table 3.3. Inclusion criterion was at least one region of high tracer expression, which could be either known or suspected brain tumors or high uptake in the pituitary gland (only in ^{68}Ga − DOTANOC patients). Exclusion criteria were:

- Patients in which the injected activity was lying outside (160 ± 35) MBq for ^{68}Ga − DOTANOC and (240 ± 45) MBq for ^{18}F − FET. The injected activity directly correlates to the number of counts in an image and consequently to its quantitative measures. To receive a uniform data pool, patients with high differences in the protocol had to be excluded.
- Tumors with very unregular shape or with difficulties to separate from artifacts or boundaries.

This retrospective study was approved by the Institutional Ethics committee and was in accordance with the 1964 Helsinki declaration and its later amendments or comparable ethical standards.

Table 3.3: *Demographics of patients included in the study*

	^{68}Ga − DOTANOC			^{18}F − FET		
	Mean(SD)	Range		Mean(SD)	Range	
		Lower	Upper		Lower	Upper
number of patients (female, male)	8 (4 f, 4 m)			16 (9 f, 7 m)		
age [y]	55(17)	30	75	53(16)	23	84
weight [kg]	76(10)	60	90	78(18)	42	117
injected activity [MBq]	158(19)	128	189	253(18)	199	278
specific inj. activity [MBq kg^{-1}]	2.1(4)	1.8	2.7	3.4(10)	2.3	6.3
post injection time* [min]	95(14)	80	117	34(3)	30	42
specific activity** [MBq kg^{-1}]	0.53(18)	0.31	0.84	2.51(74)	1.56	4.66
total prompts ($\times 10^6$) [-]	15.5(71)	9.91	31.1	162(37)	116	259

* time from injection to the start of acquisition
** specific activity at start of acquisition

3.3.2 Data Acquisition

All PET scans were performed on the combined PET/MR system Siemens Biograph mMR as explained in Section 3.1 with matrix size $172 \times 172 \times 127$ and voxel size $2.086\,\text{mm} \times 2.086\,\text{mm} \times 2.031\,\text{mm}$. Scan protocol was conducted according to local standards, oriented towards (Albert et al., 2016). Acquisition was started averagely 95(14) min for ^{68}Ga − DOTANOC and 4(3) min for ^{18}F − FET patients after injection of the tracer. One bed position with the head centered in the scanner was recorded for a full acquisition duration of 10 min in the case of ^{68}Ga − DOTANOC. For ^{18}F − FET patients, the scan data was acquired of a kinetic study which consisted of 30 min dynamic and subsequent 10 min static acquisition. "Post injection time" in Table 3.3 already includes the preceding 30 min of the kinetic

study. In both cases, ^{68}Ga − DOTANOC and ^{18}F − FET, the full 10 min acquisition was acquired and stored in list-mode format. The list-mode data was then split into frames to simulate shorter acquisition times. The 10 min data was divided into full sets of 5 min, 3 min, 2 min, 1 min and 30 s frames, similarly as demonstrated for the phantom in Figure 3.3. All generated frames then were reconstructed with the same settings as used for the phantom, OSEM (including 5 mm Gaussian post-filtering) and PSF (including point-spread-function, no post-filtering). This results in 41 individual images $(1 + 2 + 3 + 5 + 10 + 20)$ per patient and reconstruction method.

Regions of Interest - ROIs

After visual inspection, regions of high tracer uptake (tumors, or pituitary glands in ^{68}Ga − DOTANOC patients) were manually marked with *cylindrical* ROIs, the high-uptake-ROIs (HU-ROIs). In ^{18}F − FET patients, exactly one HU-ROI per patient was placed according to one identified lesion per patient, while in ^{68}Ga − DOTANOC patients up to three regions of high uptake were marked for evaluation. They could either be multiple tumors or additionally the pituitary gland, which is not a lesion or tumor but healthy tissue with simply overexpression of the tracer. Nevertheless, this region was treated similarly to tumors as a region of high uptake to study the influence of acquisition time. All together, that resulted in a total of 32 marked *regions of high uptake*, of which 16 were retrieved from the 16 ^{18}F − FET patients and 16 from the 8 ^{68}Ga − DOTANOC patients. The ROIs were designed individually and of sufficient size to contain all significant higher activity.

Additionally, three cylindrical ROIs per patient were placed in mostly uniform regions of the brain to get the "background" activity. Figure 3.6 shows the placement of the evaluated ROIs for each, a ^{68}Ga − DOTANOC and an ^{18}F − FET study.
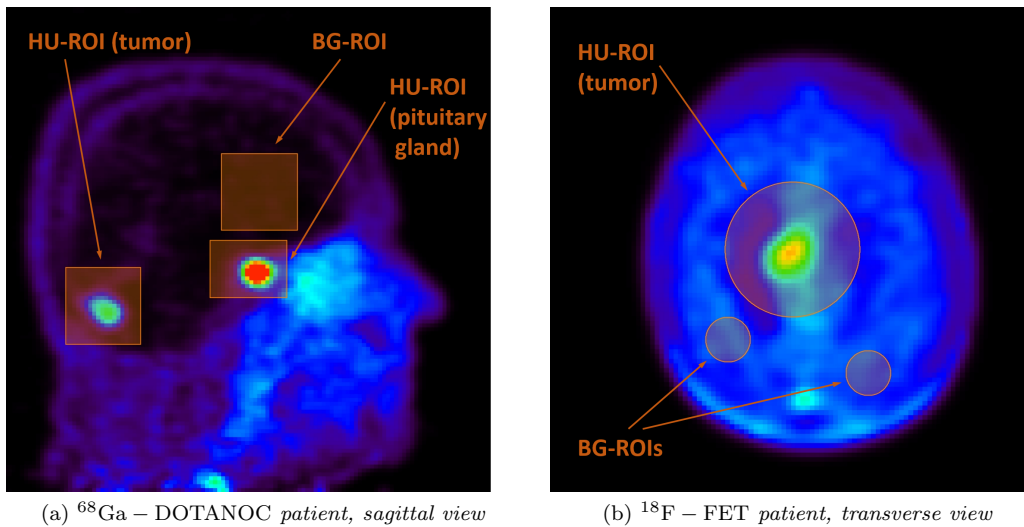

(a) ^{68}Ga − DOTANOC *patient, sagittal view*   (b) ^{18}F − FET *patient, transverse view*

Figure 3.6: *Regions of interest (ROIs) in different views as defined for (a) a ^{68}Ga − DOTANOC and (b) a ^{18}F − FET patient.*

3.3.3   Figures of Merit

The same segmentation algorithm as for the phantom (Subsection 3.2.2) was used for patient data. This includes the employed volumes of interest (VOIs) as well, which are in HU-ROIs:

- maximum voxel value: voi = max
- 3D isocontour at 41 % of the maximum voxel value adapted for background: voi = 41
- 3D isocontour at 50 % of the maximum voxel value adapted for background: voi = 50
- 3D isocontour at 70 % of the maximum voxel value adapted for background: voi = 70

Averages of the three ROIs in *uniform* regions were indexed by BG.

For evaluation of the patient data, the following measures were calculated identically to the phantom:
- Background Variability N_{BG}
- Segmented Volumes VOL_{41}, VOL_{50} and VOL_{70}
- Lesion-to-Background Ratio LBR
- Signal-to-Noise Ratio SNR_{max}

See Subsection 3.2.3 for detailed description. Additionally, and as substitute for RC_{voi} in the analysis, the **Standard Uptake Value** was defined:

$$SUV_{voi} = \frac{a_{\mathrm{voi}}}{\frac{A_{\mathrm{adm}}}{BW}} \tag{3.6}$$

with the measured activity concentration a_{voi} [kBq/ml] in the respective volume of interest (see above), the total administered activity A_{adm} [MBq] and the bodyweight BW [kg].

3.4 Statistical Analysis

Data analysis was performed on all images separately, which equals a total of:

2	reconstruction settings per patient x
41	images per patient and reconstruction setting x
32	evaluated ROIs in all patients (16 ^{68}Ga $-$ DOTANOC + 16 ^{18}F $-$ FET) =
2624	evaluated HU-ROIs

For each HU-ROI the above mentioned figures were calculated. The absolute values of each measure were additionally normalized to the according value in the reference frame, the 10 min acquisition, to express the deviation in %. Universally, the deviation would be expressed as

$$\mathrm{dev}X[t,n] = \frac{X[t,n] - X[ref]}{X[ref]} \tag{3.7}$$

with the variable X as a dummy for the figures of merit ($SUV_{\max}$, VOL_{41}, ...), and the parameters t, n and ref for the frame length, the number of the frame and the reference frame, respectively.

These deviations, mentioned as "stabilization factors" elsewhere (Cheng et al., 2014), allow the comparison of solely the *trend* of measures when changing acquisition time, even if the absolute values differ strongly. For each frame length, all frames and all patients were pooled and statistically analysed for the mentioned measures. This was done for both, the absolute and the relative (deviation) values, group sizes are shown in Table 3.4. *Mean* and *standard deviation* (SD) were used to express the average trend over all patients for normally distributed data. Otherwise, *median* and *interquartile range* (IQR) were given, where $IQR = Q3 - Q1$ describes the range from the first (25 %, Q1) to the third (75 %, Q3) percentile. Normality was tested for by using the Shapiro-Wilk algorithm at significance level of 0.05. If not stated differently, significance level of 0.01 was concluded appropriate for all other considerations in the present case. Mean or median of different frame lengths were compared via one-way-ANOVA, where the assumptions (normality, homogeneity and independence) were met or met sufficiently (Feir-Walsh and Toothaker, 1974; Keselman et al., 1998; Troncoso Skidmore and Thompson, 2012). To test, whether the mean or median deviations per frame-length-group differed significantly from 0 (the reference frame), One-Sample-t-Tests or One-Sample-Wilcoxon-Signed-Rank-Tests were performed, respectively.

Table 3.4: *Grouping and respective group sizes for the statistical analysis of patient data*

frame length	10 min	5 min	3 min	2 min	1 min	30 s
group size*	16	32	48	80	160	320

*Groups were of equal sizes for **OSEM** and **PSF**, as well as for ^{68}Ga $-$ DOTANOC and ^{18}F $-$ FET due to the same number of HU-ROIs (16).

Chapter 4

Results

In this chapter the main results of this thesis are presented. Section 4.1 details the results obtained from the phantom experiments, while Section 4.2 shows the results from the analysis of patient data.

4.1 Results from Phantom Measurements

Subsection 4.1.1 describes the measured count rates for prompt, random and true+scattered events in the phantom acquisition before visual examples of the phantom reconstructions are presented in Subsection 4.1.2. Later, the measured background activity and variability are presented in Subsection 4.1.3 and Subsection 4.1.4. The main results of evaluating recovery coefficients, segmented volumes and signal-to-noise ratios will be given in Subsection 4.1.5, Subsection 4.1.6 and Subsection 4.1.7, respectively.

4.1.1 Recorded Events

The 20 min acquisition of the phantom scan amounted to a total of 6.57×10^8 recorded events (prompts) in the listmode data, of which 1.85×10^8 are randoms and 4.72×10^8 trues (including scatter). This equals an average count rate of $5.47 \times 10^5 \, \mathrm{s}^{-1}$ (prompts) and $3.93 \times 10^5 \, \mathrm{s}^{-1}$ (trues+scatter). Figure 4.1 shows the decrease of recorded counts per frame for the 20 consecutive 1 min frames. From the first to
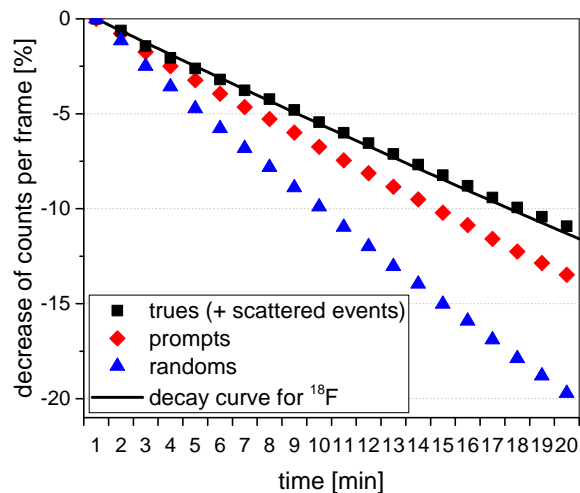

Figure 4.1: *Decreasing count rate per frame with elapsing time. Dependence of trues, prompts and randoms is shown for* 20 *consecutive frames of* 1 min. *For comparison, the solid curve gives the ideal decay rate of the pure radionuclide* ^{18}F *with a half life of* 109.77 min.

the last frame, the countrate of the trues (red diamonds) reduces by 11.1 % which fits the theoretical decay of ^{18}F (-11.3 % in 20 min). Randoms do not show linear dependence on the amount of activity in the FOV, as indicated by the blue triangles in Figure 4.1.

4.1.2 Reconstructed Images

In this section we will present reconstructed images of the phantom scan for OSEM and PSF reconstructions as well as for different acquisition durations. Figure 4.2 shows transverse slices through the center of the spheres for frame lengths 20 min and 1 min and each of the two reconstruction settings (OSEM and PSF). Visual inspection leads us to the following subjective and qualitative statements:

1. Activity in smaller spheres is significantly lower than in bigger spheres (PVE)

2. Image contrast and resolution is higher in PSF images at expense of a higher noise level

3. Boundaries of the spheres appear more precise in PSF images

4. Activities in spheres appear higher in PSF images

5. Noise increases with reduced acquisition time

6. Activity in the spheres seems to increase with reduced acquisition time

7. Contrast of spheres to the background decreases with reduced acquisition time

8. Homogeneity of activity in spheres decreases with reduced acquisition time
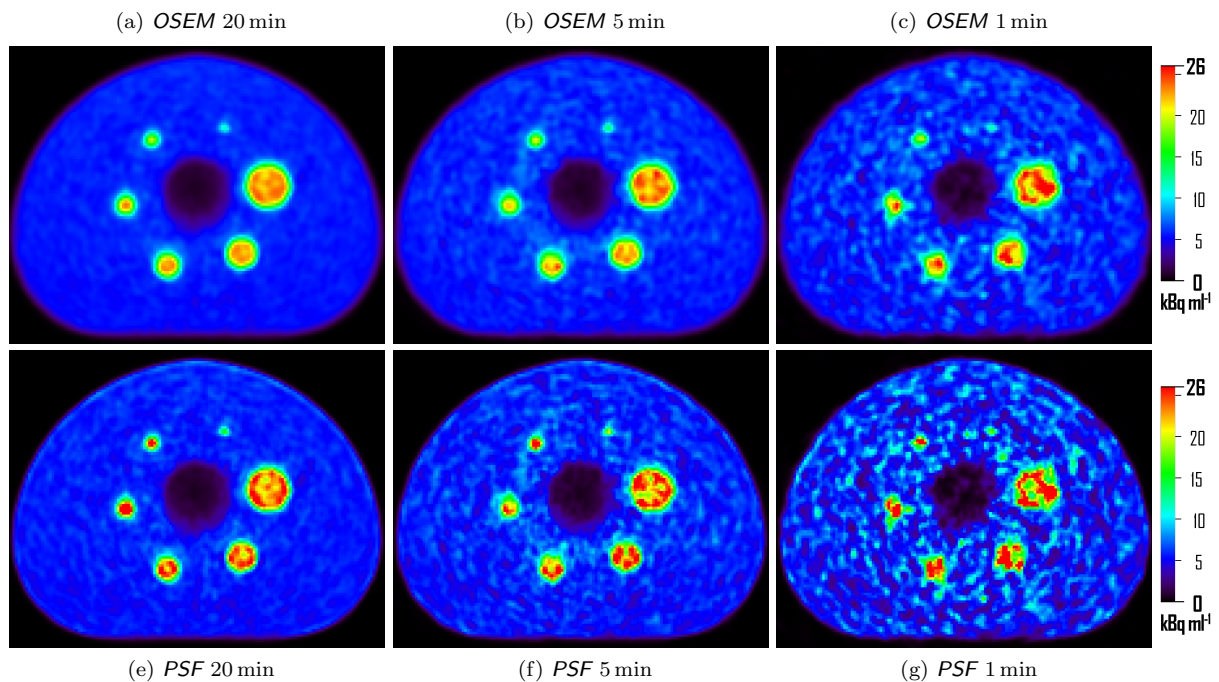

Figure 4.2: *Transverse slices of OSEM (top row) and PSF (bottom row) images with 20 min (left), 5 min (center) and 1 min (right) acquisition duration. Always first frame is shown, slices at center of 10 mm sphere were chosen. Same color scale was applied to all images. Complete series of slices with all acquisition times can be found in Appendix A.*

The line-profiles in Figure 4.3 support several of these visual observations. First, we see that the maximum activity in the small sphere (10 mm) is significantly lower than in the bigger sphere (37 mm). Second, the fluctuations of the PSF line-profiles signalize more noise and they contribute to a higher maximum activity, additionally confirming the more homogeneous appearance of OSEM images. The subjectively perceived sharper edges in PSF images can be derived from the steeper slopes in the

line-profiles. Comparing the 20 min to the 1 min line-profiles, higher noise (fluctuation) is found. This translates to higher maximum values in the 1 min images, supporting the conception of increasing activity with reduced acquisition time.
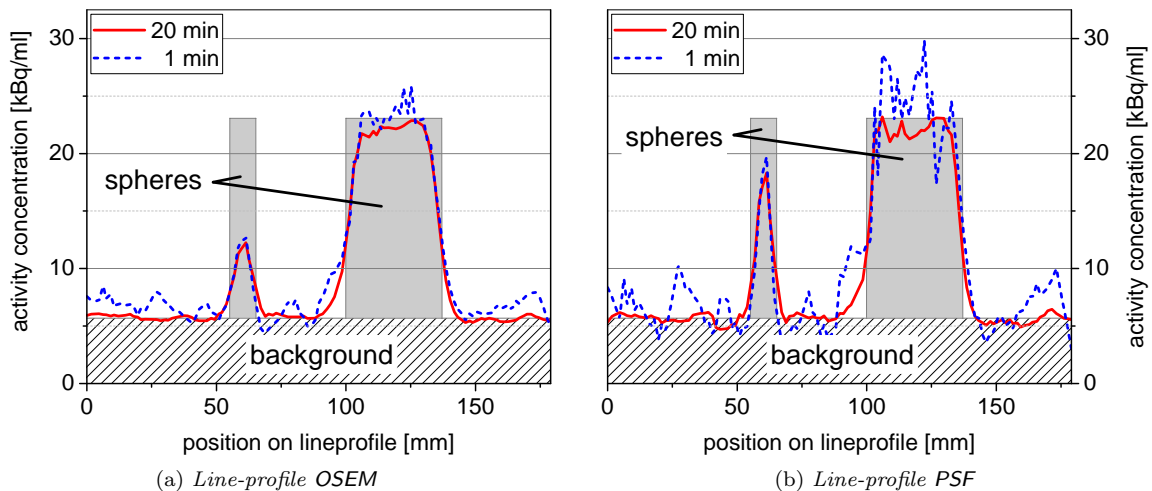

(a) *Line-profile OSEM* (b) *Line-profile PSF*

Figure 4.3: *Line-profiles of* 20 min *and* 1 min *images with OSEM and PSF reconstruction. Line-profiles go through the centers of* 10 mm *and* 37 mm *spheres, taken in the center-slices as shown in Figure 4.2. Ideal activity distributions are indicated by the gray areas.*

4.1.3 Background Activity

In the 20 min acquisition of OSEM and PSF images we found similar values for a_{BG} of $5.641\,\mathrm{kBq\,ml^{-1}}$ and $5.623\,\mathrm{kBq\,ml^{-1}}$, respectively. The dependence of measured activity concentration in the background a_{BG} on the acquisition duration is shown in Figure 4.4 for both reconstruction settings combined. When reducing the acquisition time, we found a steady increase of a_{BG}. While the difference for the 10 min frames is not yet statistically significant at the 1 % confidence level, acquisitions of 5 min or shorter differ significantly. The 5 min acquisitions yield an increase of 4.1(7) % in background activity, the shortest acquisitions (1 min frame length) 5.6(6) %. This translates to an approximate increase of 0.28 %/min for every minute of reduced acquisition time if a linear behaviour is assumed. The reduction from 5 min to 1 min acquisitions yields significant difference (1 % confidence level) of the two mean a_{BG} values. The mentioned findings apply similarly to OSEM and PSF.

In Figure 4.4 we additionally see a differentiation by the number of recorded events (shown for PSF). Similar plots obtained from OSEM reconstructions and 5 mm Gaussian post-filtering can be found in Appendix A. The background activity a_{BG} correlates significantly ($P < 0.05$) with the countrate in the respective frame, showing a Pearson correlation of -0.85 and -0.84 for OSEM and PSF, respectively.
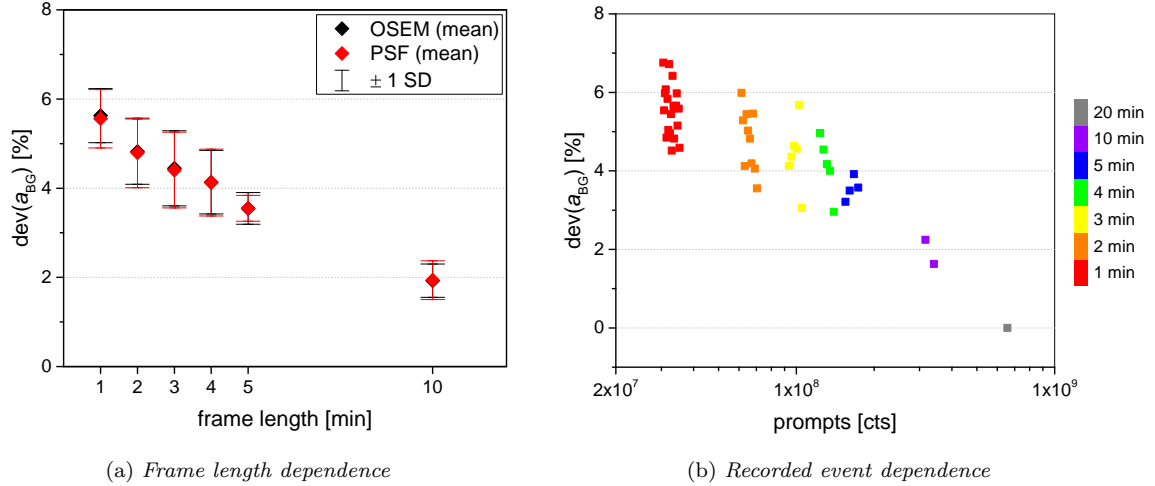
(a) *Frame length dependence*

(b) *Recorded event dependence*

Figure 4.4: *Background activity* a_{BG} *as a function of (a) frame length and (b) number of counts in the image (for* PSF*).*

4.1.4 Background Variability

The evaluation of the image noise N_{BG} is shown in Figure 4.5 for both OSEM and PSF reconstruction. The background variability in the 20 min OSEM and PSF images equals to 5.59 % and 9.15 %, respectively. When reducing the acquisition time, we found a continuous increase in noise for both reconstructions. As for a_{BG}, the difference in the 10 min images is not statistically significant, but for frame lengths of 5 min and shorter we found significant deviations at the 0.01 level for both, OSEM and PSF. For frames with the same length, the noise levels differ very little with coefficient of variations between 0.016 and 0.025. For reduction of the frame length by a factor of 6 down to 3 min, N_{BG} in the OSEM images more than doubles to a value of 11.5(1) %, compared to triple the noise (18.8(4) %) in the 1 min frames. In the PSF images the noise doubles when reducing frame length down to 4 min, in the 1 min frames N_{BG} increases fourfold to an average of 38.2(9) %.

The noise N_{BG} correlates directly to the number of recorded counts with an Pearson coefficient of -0.75 (significant at the 0.05 level) for both, OSEM and PSF. In Figure 4.5 the curve fit $y = a + b/\sqrt{x}$ yields $a = 3.03 \times 10^{1}$ % and $b = 2.16 \times 10^{7}$ % with an R-square of 0.998 for OSEM, and $a = 1.68 \times 10^{2}$ % and $b = 9.81 \times 10^{6}$ % with an R^2 of 0.997 for PSF. a_{BG} and N_{BG} correlate significantly at the 5 % level with a Pearson coefficient of 0.80 and 0.79 for OSEM and PSF, respectively.

(a) *Frame length dependence* (b) *Recorded event dependence*
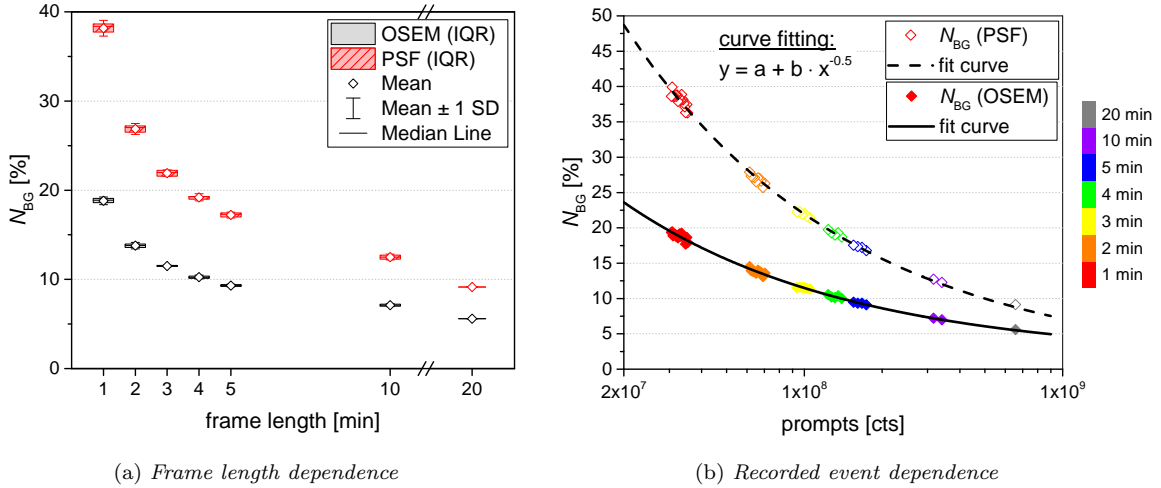
Figure 4.5: *Background variability* N_{BG} *as a function of (a) frame length and (b) number of counts in the image, for reconstruction settings OSEM and PSF.*

4.1.5 Recovery Coefficient

RC-values describe the deviation of the *LBR* measured in the image to LBR_{true}, the ratio of the truly administered activity concentrations (4.065). The evaluation reveals that *RC* values depended strongly on two factors, *sphere size* and *frame length*, what can be seen in Figure 4.2.

Effects of the partial volume effect (PVE) are clearly visible in both extremes, the 20 min and the 1 min acquisitions. Comparing the smaller spheres to the biggest one (37 mm), all three measures RC_{max}, RC_{41} and RC_{mean} show steadily lower values, the smaller the sphere diameter. Figure 4.6 shows the corresponding *RC* values for the OSEM reconstruction. For the 20 min OSEM image, the RC_{max} values of 37 mm and 10 mm spheres differ by 52 % and for the corresponding 1 min images by 57 %. Analogously, RC_{mean} in the smallest sphere is by 53 % and 52 % lower in the 20 min and 1 min images compared to the biggest sphere. At the 0.01 level, PVE in the 1 min images affects RC_{max} and RC_{mean} significantly different. In the corresponding PSF images, the PVE ranges between -43% and -56% for RC_{max} and -40% and -48% for RC_{mean} in the 20 min and 1 min images, respectively. Additionally, the lower average *RC* values, the variation of values between frames increases for smaller spheres, as indicated by the box sizes and error bars in Figure 4.6. Even the 37 mm sphere shows 19 % and 15 % of injected activity is spread out of the sphere in the OSEM and PSF reference image, respectively. This is apparent when looking at the line-profiles Figure 4.3 where spill-out is clearly notable. Due to noise, the peak (RC_{max}) does not sink below 1 but over-represents the actually injected activity by 12 % and 41 % in the OSEM and PSF images, respectively. In the 1 min frames, the average spill-out is 21 % and 17 % (OSEM and PSF). The 10 mm sphere shows 62 % and 56 % spill-out and RC_{max} underestimates the injected activity by 47 % and 20 % in the OSEM and PSF reconstructed reference images. Spill-out in the 1 min frames is not significantly different from the reference frame.

RC-values predominantly increase continuously when reducing acquisition time, as demonstrated in Figure 4.7 for 37 mm and 10 mm spheres. As pointed out before, the sphere size has a crucial influence on the *RC* values, therefore the results for dependence on frame length will be presented separately for the biggest (37 mm) and the smallest (10 mm) sphere.
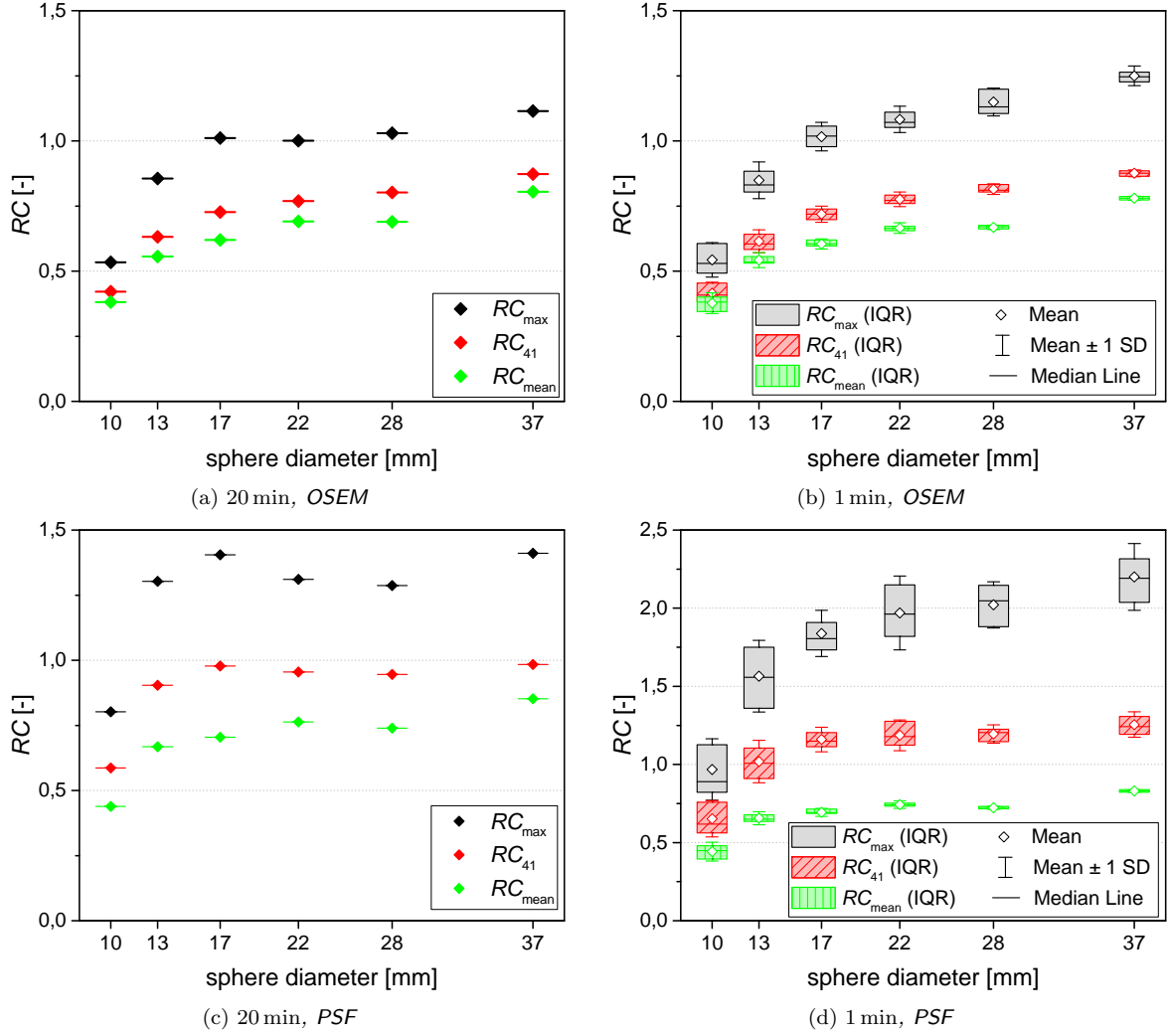
(a) 20 min, *OSEM*

(b) 1 min, *OSEM*

(c) 20 min, *PSF*

(d) 1 min, *PSF*

Figure 4.6: *Influence of sphere size on RC values is shown for* 20 min *(left column) and* 1 min *(right column) acquisitions with* **OSEM** *(top row) and* **PSF** *(bottom row) reconstruction. The three segmentation levels* $RC_{\max}$, RC_{41} *and* RC_{mean} *are separated by different colors. Box size represents the interquartile range (IQR).*

37 mm sphere

RC_{mean} in the 20 min OSEM acquisition is at 0.81 and 0.85 in the OSEM and PSF images, respectively. For shorter frame lengths average RC_{mean} values decrease by 3 % and 2 % compared to the 20 min frame for OSEM and PSF, respectively. This decrease is significant for frame times $\leq$5 min due to negligible deviations of similar frames, as indicated by the small boxes and bars. In the 20 min images, $RC_{\max}$ compared to RC_{mean} is overestimated by 39 % and 66 % with OSEM and PSF reconstruction, respectively. $RC_{\max}$ increases steadily from 1.12-1.25(4) (+12(3) %) in the OSEM image and from 1.41-2.20(21) (+56(15) %) in the PSF when reducing frame length to 1 min. The increase of $RC_{\max}$ with shorter frame length is significant for acquisition times $\leq$2 min in OSEM and $\leq$3 min in PSF. Increase of RC_{41} is not significant for any frame length in OSEM images. Using PSF reconstruction RC_{41} increases by 28 % when reducing acquisition time down to 1 min, showing significance for frame lengths $\leq$3 min.

10 mm sphere

RC_{mean} in the 20 min OSEM acquisition is at 0.38 and 0.44 in the OSEM and PSF images, respectively. The respective $RC_{\max}$ values are 0.53 and 0.80 (+40 % and 83 %) for OSEM and PSF reconstruction, respectively. For all shorter frame lengths average RC_{mean} and RC_{41} values do not deviate

significantly from the 20 min frame for both reconstructions. $RC_{\max}$ in the OSEM images does not deviate significantly from its corresponding 20 min value. In the PSF images only the average $RC_{\max}$ of the 1 min frames shows a significant increase of 20 % while the median maintains at the same RC level. Figure 4.7 visually confirms that average and median RC values are not or just insignificantly influenced by the frame length, whereas the deviations of individual frames increase strongly, as indicated by box size and length of the whiskers.

The results for the remaining spheres with 13 mm, 17 mm, 22 mm and 28 mm in diameter can be very well drawn from interpolation between the previously discussed spheres. For OSEM reconstruction, $RC_{\max}$ is not affected for spheres smaller than 20 mm in diameter. The 22 mm sphere shows minimal but significant increases of $RC_{\max}$ for acquisition times below 2 min (OSEM). In the OSEM images, RC_{41} does not show any significant deviations from the reference frame for any sphere size. RC values of the The PSF images are generally affected stronger and show increasing deviations for bigger spheres. In the 1 min frames, $RC_{\max}$ shows significant deviations even for the 13 mm sphere. For spheres bigger than 20 mm the deviation of $RC_{\max}$ is significant even for acquisition times of 5 min. RC_{41} deviates from the reference value when reducing frame length below 3 min for all spheres ≥ 17 mm. The respective graphs for spheres 13-28 mm can be found in Appendix A.

Summarized, we found that RC_{mean} underestimated the LBR in all combinations of sphere size and frame length. The absolute RC-values range between 0.5 and 0.8 in OSEM images and 0.45 and 0.85 in PSF images. This indicates heavy influences of PVE with spill-out fractions between 15 % and 55 %. The maximum activity value on the other side overestimates LBR in the biggest spheres, but underestimates it as well in small spheres. For smaller spheres, PVE dominates over effects of acquisition time, while activity values in bigger spheres are even overestimated and hence have to be influenced by noise.
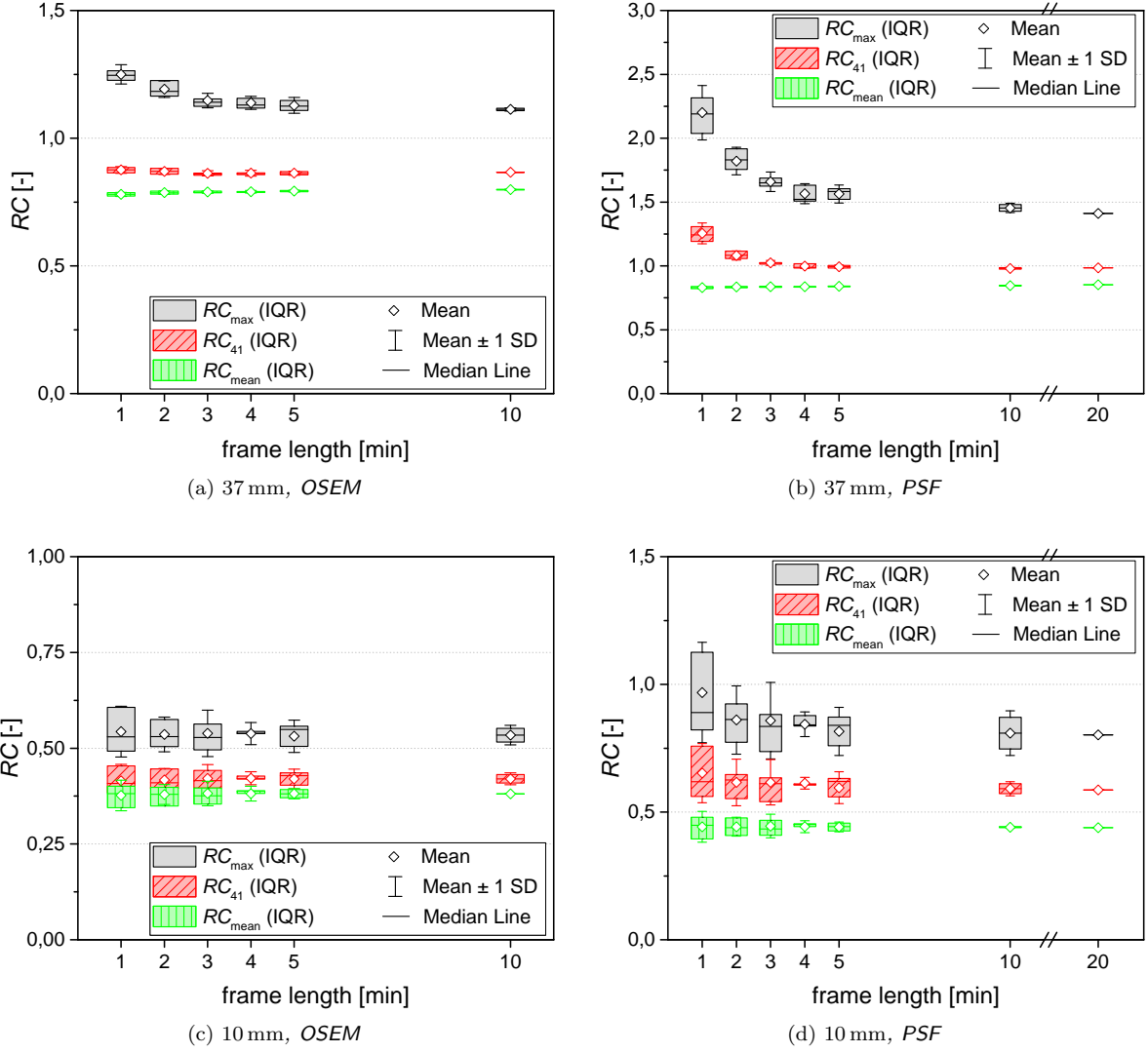
Figure 4.7: *The dependence of RC_{max}, RC_{41} and RC_{mean} values on acquisition duration is shown for evaluation of the 37 mm (top row) and 10 mm sphere (bottom row) with OSEM (left column) and PSF (right column) reconstructions.*

4.1.6   Segmented Volume

As in the previous section, results for 37 mm and 10 mm spheres will be presented separately because of fundamental differences in the outcome of the evaluation.

37 mm sphere

Figure 4.8 shows the amount of the actual sphere volume (VOL_{true}) that is segmented by the algorithm using two different thresholds, 41 % and 70 %. In the 20 min images VOL_{41} segments $83\,\%_{vol}$ and $72\,\%_{vol}$ of the actual volume using OSEM and PSF, respectively. VOL_{70} yields suitably lower values of $51\,\%_{vol}$ and $17\,\%_{vol}$. The reduction of acquisition duration drives VOL_{41} to decrease by 11 % to $74\,\%_{vol}$ in the OSEM images and by 65 % to $25\,\%_{vol}$ in the PSF. VOL_{70} is influenced similarly by shorter frame times when using OSEM (see Figure 4.8), but with PSF reconstruction the volume drops even below $2\,\%_{vol}$. Compared to the 20 min acquisitions, differences in VOL_{41} are significant for frame durations ≤ 2 min in OSEM and ≤ 3 min in PSF images.

41

10 mm sphere

In the 20 min images VOL_{41} segments $74\,\%_{\mathrm{vol}}$ and $25\,\%_{\mathrm{vol}}$ of the actual volume using OSEM and PSF, respectively. VOL_{70} yields suitably lower values of $22\,\%_{\mathrm{vol}}$ and $12\,\%_{\mathrm{vol}}$. Contrarily to the 37 mm sphere, the reduction of acquisition duration causes VOL_{41} to *increase* by $137\,\%$ to $176\,\%_{\mathrm{vol}}$ in the OSEM images and by $122\,\%$ to $90\,\%_{\mathrm{vol}}$ in the PSF. As can be seen in Figure 4.8, the deviations within a frame length increase substantially as well. Nevertheless, the mean VOL_{41} values only differ significantly for frames ≤ 1 min in both reconstruction cases. As opposed to the biggest sphere, VOL_{70} in the 10 mm sphere for both cases, OSEM and PSF, shows just greater variation but no significant change in mean value.
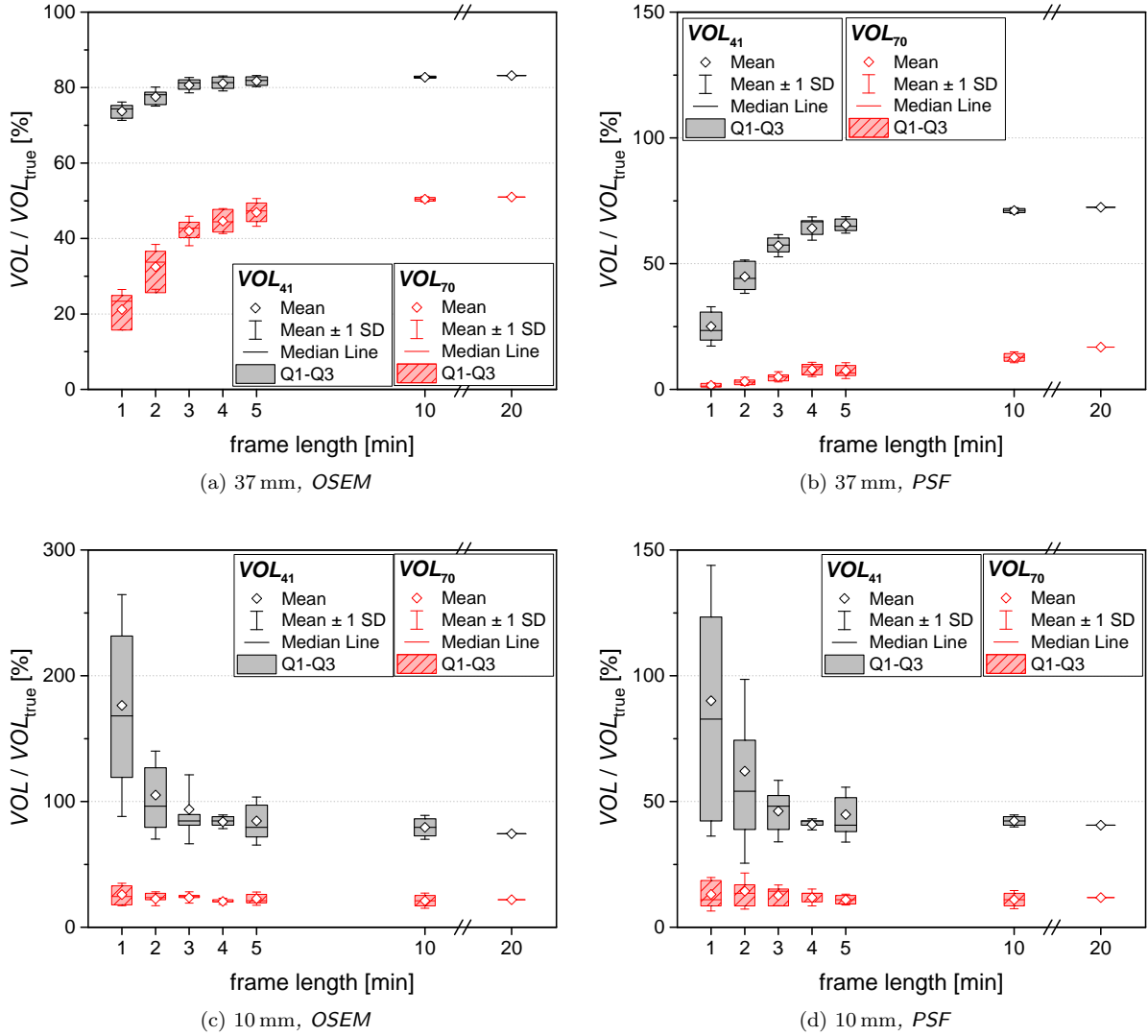
Figure 4.8: *Dependence of recovered volume on acquisition duration in the 37 mm (top row) and 10 mm (bottom row) spheres is presented for reconstruction settings* **OSEM** *(left column) and* **PSF** *(right column). The fraction of the actual sphere volume* VOL_{true} *that was recovered by the segmentation algorithm at thresholds 41 % and 70 % is presented in each figure.*

As a comparison between the two segmentation thresholds $41\,\%$ and $70\,\%$, Figure 4.9 displays VOL_{70} as a fraction of VOL_{41}. In both cases, OSEM and PSF, proportionally VOL_{70} decreases stronger than VOL_{41} when reducing acquisition time. Figure 4.10 illustrates the degrading performance of the segmentation algorithm when reducing acquisition time. We see that for longer acquisition times, VOL_{70} (violet) covered almost similar areas as VOL_{41} (black). With shorter frame times, VOL_{70} recovers significantly less sphere volume and is very prone to heterogeneities of the activity distribution. Secondly, the figure shows that with reduced acquisition time both VOL_{41} and VOL_{70} recover less volume and

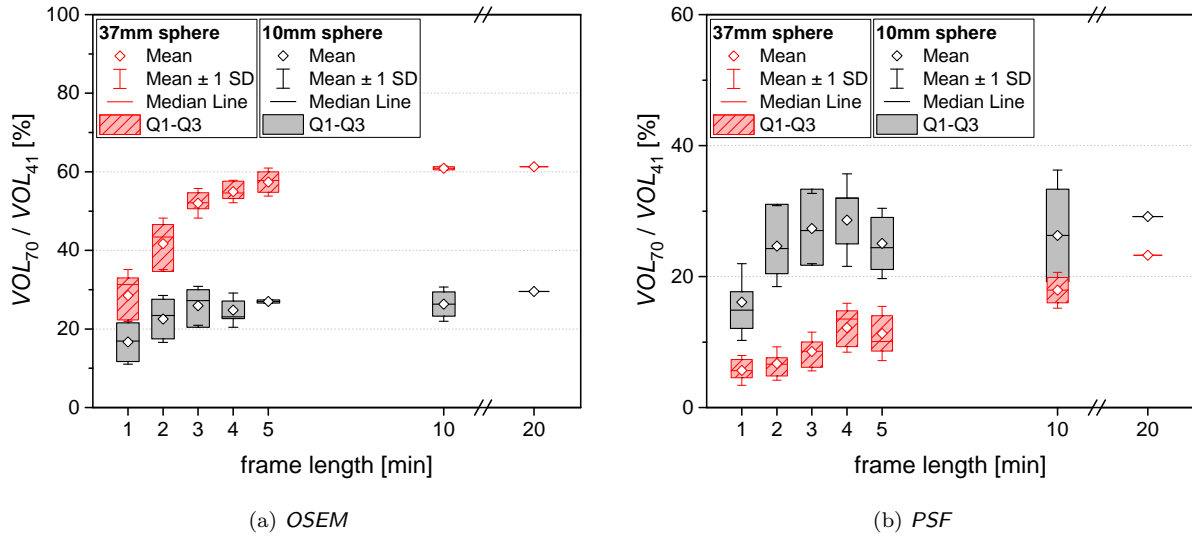show very irregular formations compared to the true spherical form.

(a) *OSEM*   (b) *PSF*

Figure 4.9: *The figures show VOL_{70} as fraction of VOL_{41} for the $37\,$mm and the $10\,$mm sphere and for various acquisition times. (a) provides results for OSEM images, (b) for PSF.*
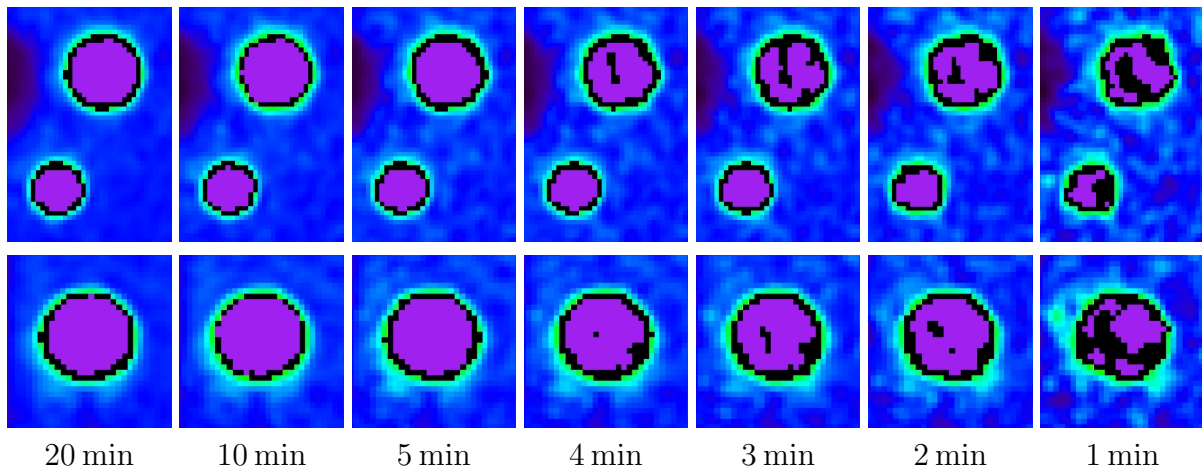

Figure 4.10: *Segmented volumes visualized for several acquisition times in an OSEM image. Violet areas mark VOL_{70}, black areas mark additional areas covered by VOL_{41}. In the transverse slice (top row) the segmentations are shown for the $28\,$mm and $37\,$mm spheres, the corresponding coronal slice shows only the $37\,$mm sphere. From left to right acquisition time decreases.*

4.1.7 Signal-to-Noise Ratio

The influence of reduced acquisition time on SNR_{max} is presented in Figure 4.11 for OSEM and PSF separately. In the $20\,$min OSEM frame, the absolute value of SNR_{max} is 81 and 39 for the $37\,$mm and $10\,$mm spheres, respectively. When reducing acquisition time by a factor of 20 (to $1\,$min), SNR_{max} decreases by $67\,\%$ and $70\,\%$ to absolute values of 27 and 12 for the mentioned spheres. In the $20\,$min PSF frame, the absolute value of SNR_{max} is 63 and 24 for the $37\,$mm and $10\,$mm spheres, respectively. When reducing acquisition time down to $1\,$min, SNR_{max} decreases by $78\,\%$ and $76\,\%$ to absolute values of 13 and 6 for the mentioned spheres. SNR_{max} is significantly different for $\leq 5\,$min. Absolute values for SNR_{max} in two inherently different image slices (OSEM vs. PSF and $20\,$min vs. $1\,$min) with consequently distinct noise levels are presented in Figure 4.12.
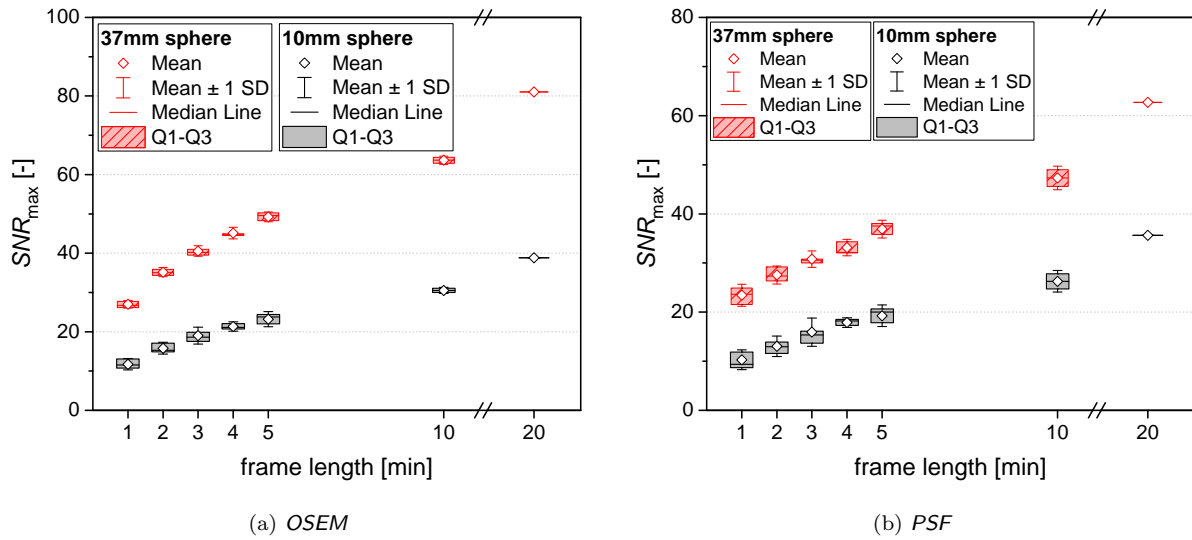
(a) *OSEM*

(b) *PSF*

Figure 4.11: *Absolute* SNR_{max} *values for various frame lengths are presented separately for (a)* **OSEM** *and (b)* **PSF**. *Results are shown for the two extreme spheres with* $37\,mm$ *and* $10\,mm$ *in diameter.*

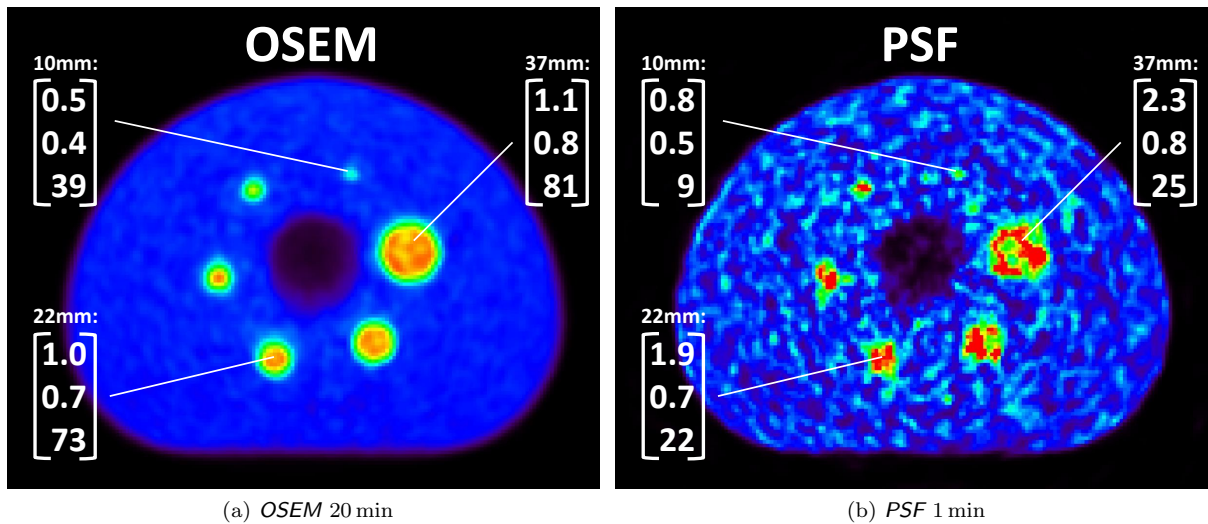(a) *OSEM* 20 min

(b) *PSF* 1 min

Figure 4.12: *Demonstrating the visual correspondence of quantitative measures in two transverse slices with fundamentally different noise levels. Numbers are* RC_{max} *(top),* RC_{mean} *(center) and* SNR_{max} *(bottom) for spheres with* $10\,mm$, $17\,mm$ *and* $37\,mm$ *diameter as indicated. (a) shows the transverse slice of the* $20\,min$ **OSEM** *acquisition (* $N_{BG} = 5.59$ *). For (b) the first frame of the* $1\,min$ **PSF** *acquisitions was taken (* $N_{BG} = 36.3$ *).*

4.2 Results from Patient Scans

In this section the main results obtained from $^{18}\text{F} - \text{FET}$ and $^{68}\text{Ga} - \text{DOTANOC}$ patient studies are presented. Similar to the previous section, initially the relation between frame length and countrate in patient data will be examined before proceeding to the results of each figure of merit in separate subsections.

4.2.1 Recorded Events

Theoretically, the average countrate in the 30 s frames ought to fall by 5.82 % between first and last (20th) frame when using $^{18}\text{F} - \text{FET}$ and by 9.28 % when using $^{68}\text{Ga} - \text{DOTANOC}$. As shown in Figure 4.13, the actually measured countrate per frame reduced by 12.4 % and 10.1 % in $^{68}\text{Ga} - \text{DOTANOC}$ and $^{18}\text{F} - \text{FET}$ patients, respectively. This shorter half-life we see in the actual measurement is most likely caused by additional biological effects that redistribute the activity and eliminate tracer from the body. The division of the full acquisition (10 min) into up to 20 frames of 30 s length thus introduces a deviation between the first and the last frame of a single patient. Additionally, the total number of prompts in the full 10 min acquisitions of the patients among each other deviate too, depending on the injected activity, post-injection time, metabolic uptake, etcetera. Figure 4.14 shows the relation between the number of prompts in a frame to its frame length. In total for all patients, we see that the images of a specific frame length have quite different numbers of counts in them.
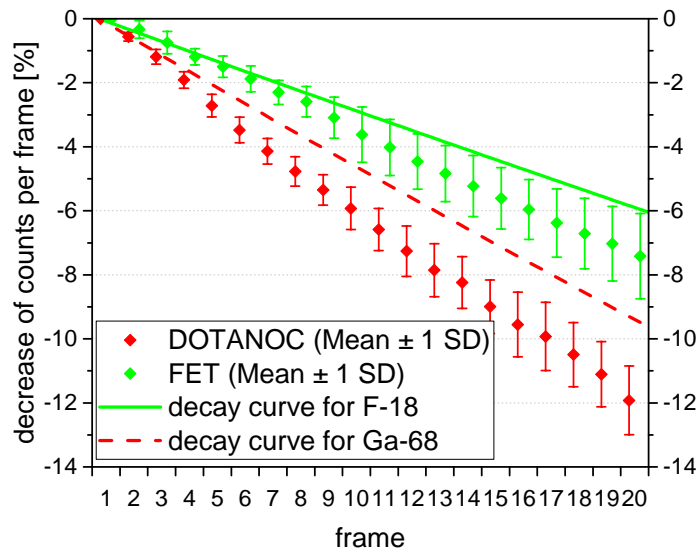

Figure 4.13: *Number of recorded counts (prompts) per* 30 s *frame reduces from the first to the last frame as shown in the graph. Symbols show the mean value of all* 8 $^{68}\text{Ga} - \text{DOTANOC}$ *(red) and* 16 $^{18}\text{F} - \text{FET}$ *patients (green), errorbars indicate* 1 *SD. For comparison, the dashed and the solid curves give the decay rate of the pure radionuclides* ^{68}Ga *and* ^{18}F *with half lives of* 67.63 min *and* 109.77 min*, respectively.*
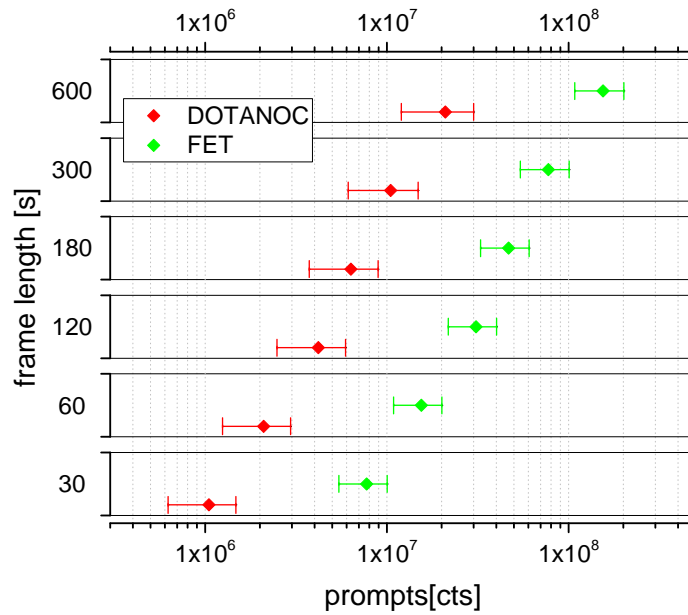
Figure 4.14: *Relation between the frame length and the recorded counts (true and scattered events) in the respective frame is shown in a lin-log plot for the* ^{68}Ga $-$ DOTANOC *(red) and* ^{18}F $-$ FET *(green) patient pool.*

4.2.2 Reconstructed Images

Visual assessment of the patient scans revealed similar tendencies as found for the phantom but with slightly less obvious consequences when reducing acquisition time. Background variability was found in both patient groups to increase, again the impacts were stronger on PSF images than on OSEM. In PSF images several artefacts were identified, which apparently arose from amplification of background variability. ^{68}Ga $-$ DOTANOC patients (see Figure 4.15) show a very clear separation between lesions and background which with OSEM reconstruction is not really hampered by reducing acquisition time. With PSF the lesions in long acquisitions appear sharper than in the OSEM images, but when reducing acquisition time high background variability influences the image and introduces apparent errors in the background. ^{18}F $-$ FET scans (see Figure 4.16) show more background and consequently harder separation and detection of the tumors. The line-profiles in Figure 4.17 supports this visual and subjective impression, where we see only a small difference between the highest uptake in the tumor and increased background activity.
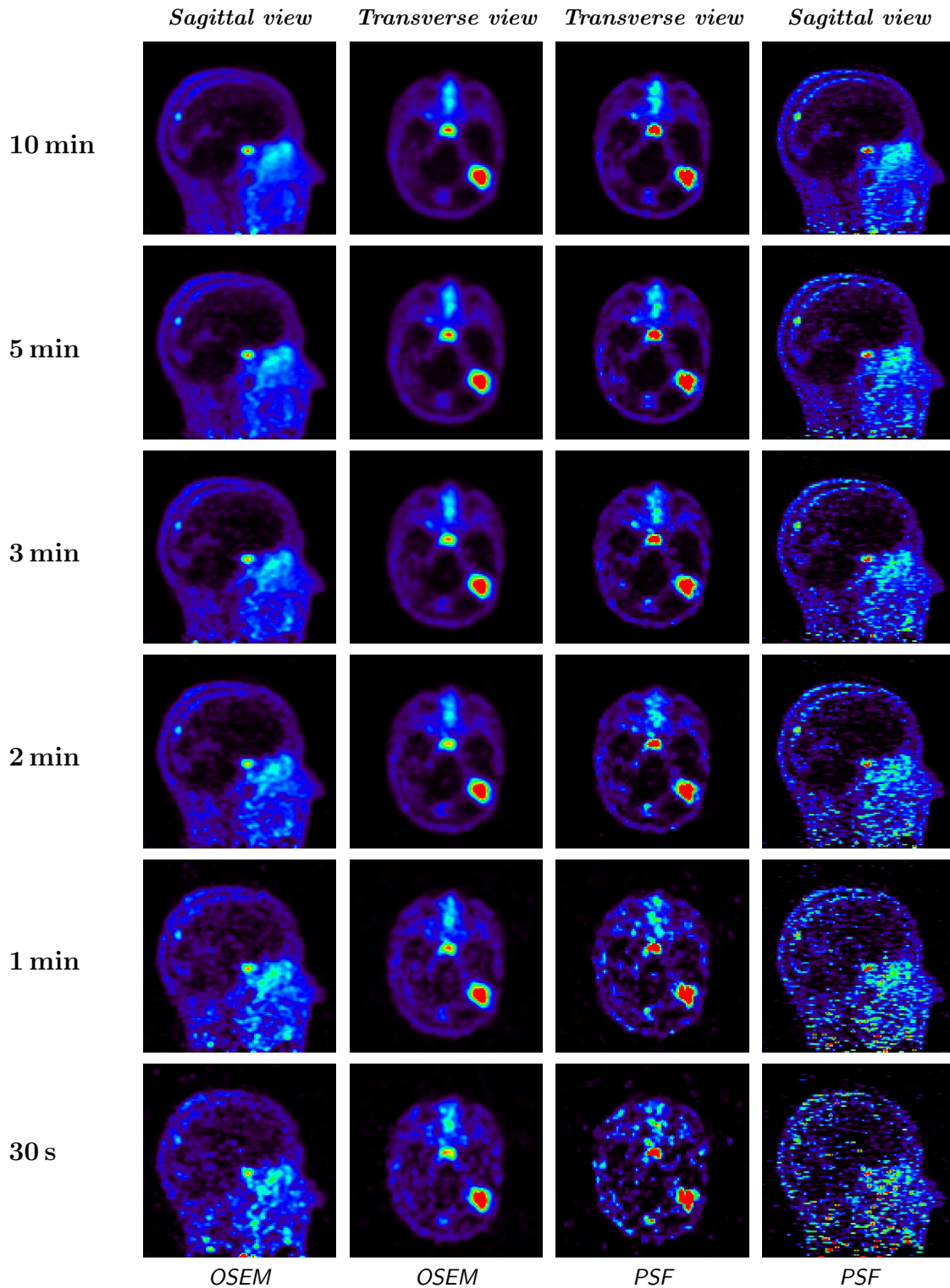
	Sagittal view	*Transverse view*	*Transverse view*	*Sagittal view*
10 min				
5 min				
3 min				
2 min				
1 min				
30 s				
	OSEM	*OSEM*	*PSF*	*PSF*

Figure 4.15: *Sagittal and transverse slices of a* ^{68}Ga $-$ DOTANOC *patient. The two columns to the left show the OSEM images, the two to the right the PSF images. Acquisition time decreases from top (10 min) to bottom (30 s). Always the first frame of the whole acquisition is presented. Sagittal views show the slice through the middle of the pituitary gland and a lesion. All images are scaled equally.*

(a) *OSEM* 10 min   (b) *OSEM* 2 min   (c) *OSEM* 30 s

(d) *PSF* 10 min   (e) *PSF* 2 min   (f) *PSF* 30 s
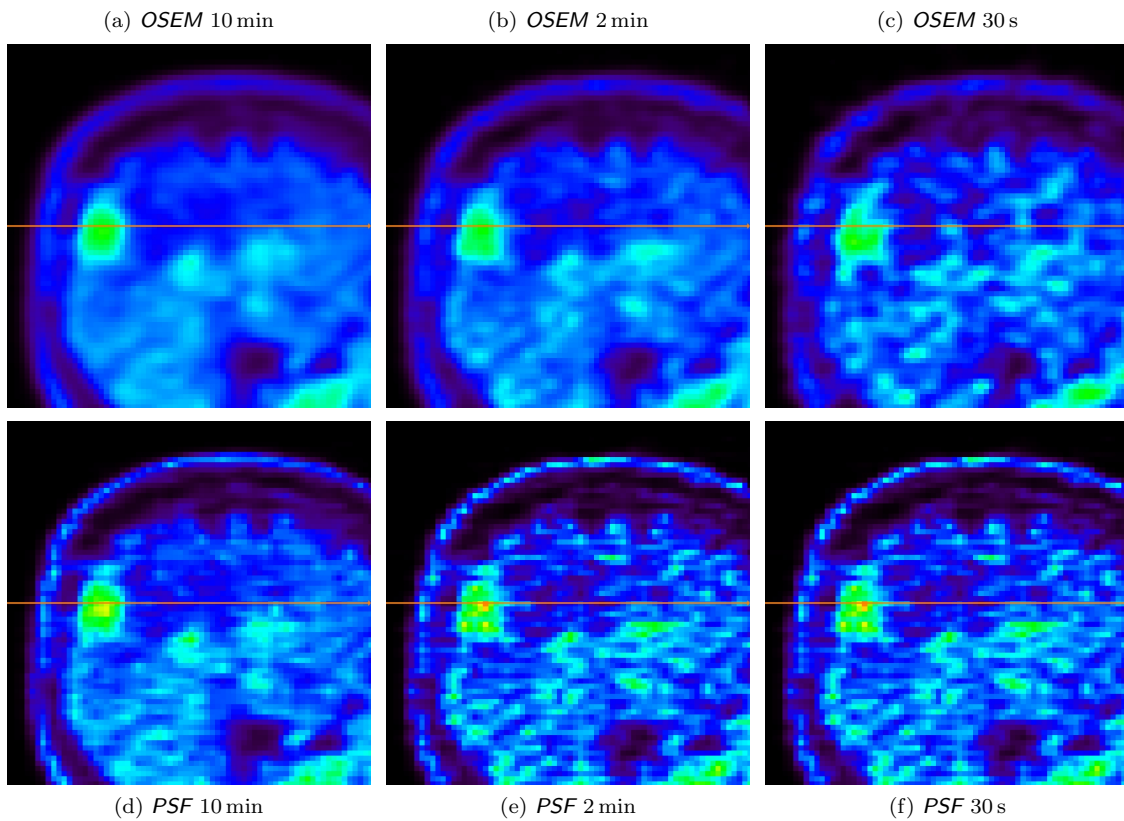
Figure 4.16: *Sagittal slices of a* ^{18}F − FET *patient. Acquisition times* 10 min *(left),* 2 min *(center) and* 30 s *(right) with* **OSEM** *(top row) and* **PSF** *(bottom row) reconstruction are presented. Always first frame of the whole acquisition is shown. For the according line-profiles see Figure 4.17. Position of the line-profiles is indicated by the orange lines in the images. Equal color-scale is applied to all images.*

(a) *Line-profile* **OSEM**   (b) *Line-profile* **PSF**
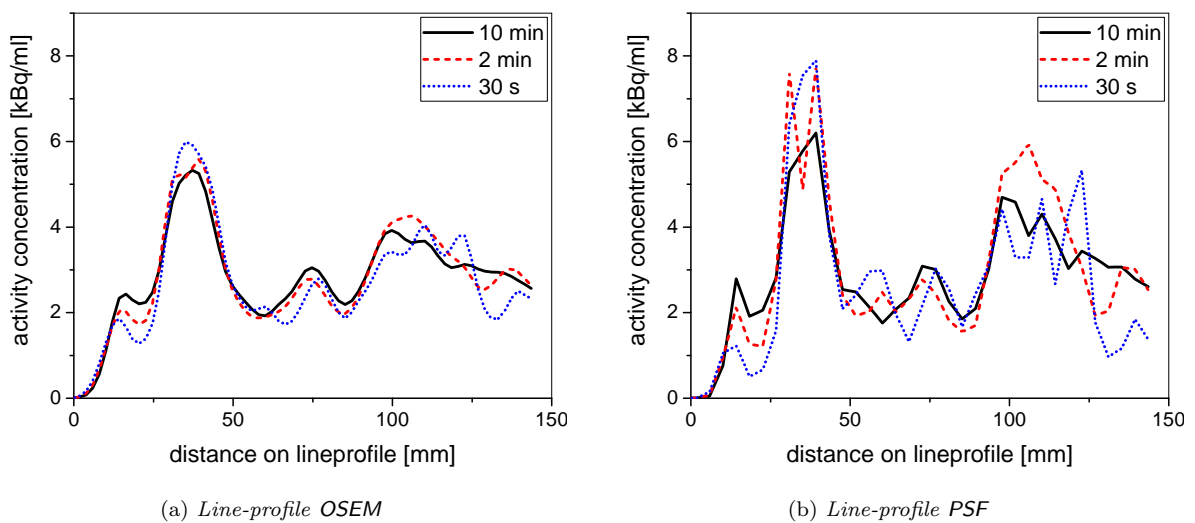
Figure 4.17: *Line-profiles for the images of a* ^{18}F − FET *patient, according to Figure 4.16.*

4.2.3 Background Activity

DOTANOC In ^{68}Ga $-$ DOTANOC patients, activity in the background regions is as low as 30-90 Bq ml^{-1}. In the reference frame SUV_{BG} is found at 0.10(3) f and 0.09(3) for OSEM and PSF, respectively. For frame lengths of 2 min, SUV_{BG} on average increases slightly but yet significantly by 10(9) % with OSEM and PSF. For 1 min frame length, the deviations of SUV_{BG} distribute irregularly with two separate points of high concentrations, which is indicated by the huge interquartile range (IQR) of 30-170 % in Figure 4.18. The 30 s frames show a regular (normal) distribution again, with an average increase of SUV_{BG} of 173(34) % compared to the 20 min acquisition for both reconstruction settings. When the average background activity of the frames is viewed against the respective number of recorded prompts, a sudden increase of SUV_{BG} is visible around 2.35×10^6 events. Figure 4.19 shows this irregularity for ^{68}Ga $-$ DOTANOC, where SUV_{BG} jumps from ~ 10 % to over 100 %.

FET In ^{18}F $-$ FET patients, the background activity ranges between 1.6 kBq ml^{-1} and 5.7 kBq ml^{-1} resulting in an average SUV_{BG} of 0.95(19) in the reference frame for both OSEM and PSF. Changes in background activity are significant for frame times ≤ 1 min with a decrease of $-3(2)$ % (see Figure 4.18) for the 30 s frames in OSEM and PSF images. Figure 4.19 shows the continuous reduction of SUV_{BG} with decreasing number of prompts per frame. Difference between e.g. a 30 s and a 60 s frame with the similar number of prompts is not significant. The abrupt change of SUV_{BG} below 2.35 prompts was confirmed by a reevaluation of an discarded patient (not shown in Figure 4.19) where the 30 s frames had counts less than the mentioned number.

Notched box charts: The box marks the interquartile range (IQR), so the upper edge is the third quartile, the lower edge the first quartile. The mean is represented by the symbol, the whiskers give the standard deviation (SD) of the underlying data from the mean. The median is marked by the notches on the box, where the height of the notches gives the 95 % confidence level. The upper (U) and lower (L) limits are calculated by $median \pm 1.58 \cdot (IQR/\sqrt{n})$, with the interquartile range $IQR = Q3 - Q1$ and the number of data points n (Origin). Two median values would be significantly different at the 0.05 level, if the notches of two boxes do not overlap (McGill et al., 1978).
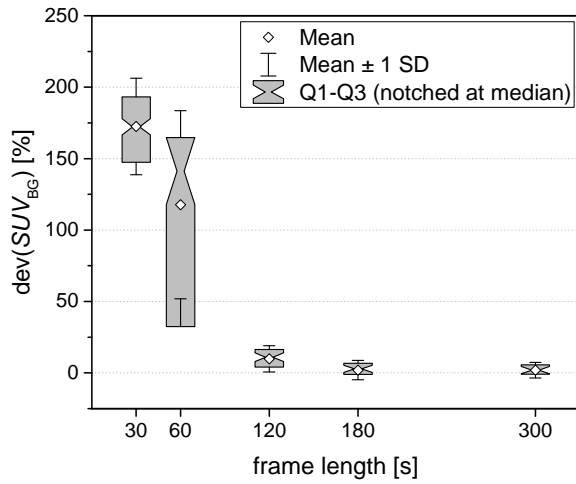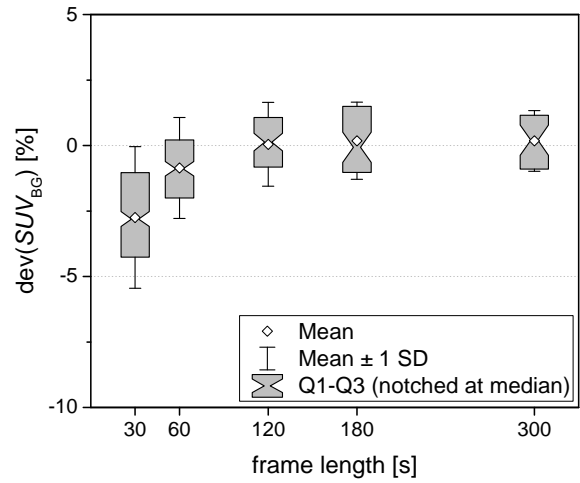
(a) ^{68}Ga − DOTANOC, *OSEM*
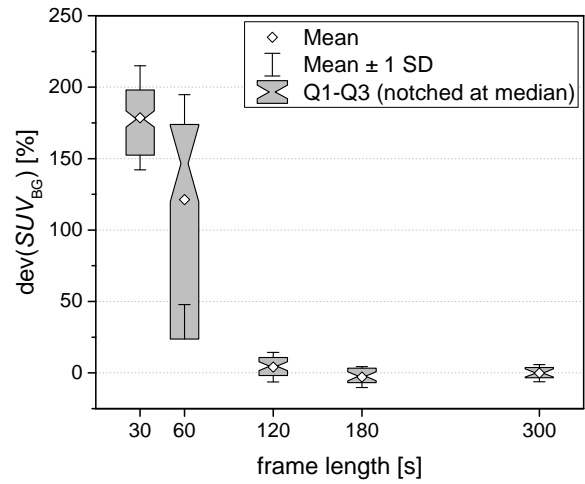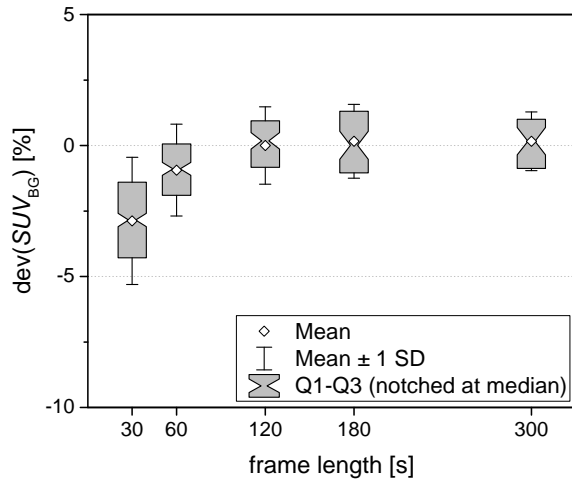
(b) ^{68}Ga − DOTANOC, *PSF*

(c) ^{18}F − FET, *OSEM*

(d) ^{18}F − FET, *PSF*

Figure 4.18: *Dependence of background activity* a_{BG} *on frame length. Relation is shown for the 8* ^{68}Ga − DOTANOC *(top row) and the 16* ^{18}F − FET *patients with reconstruction settings* **OSEM** *(left column) and* **PSF** *(right column). Values are shown as deviations from the* 10 min *acquisitions in a notched boxplot.*
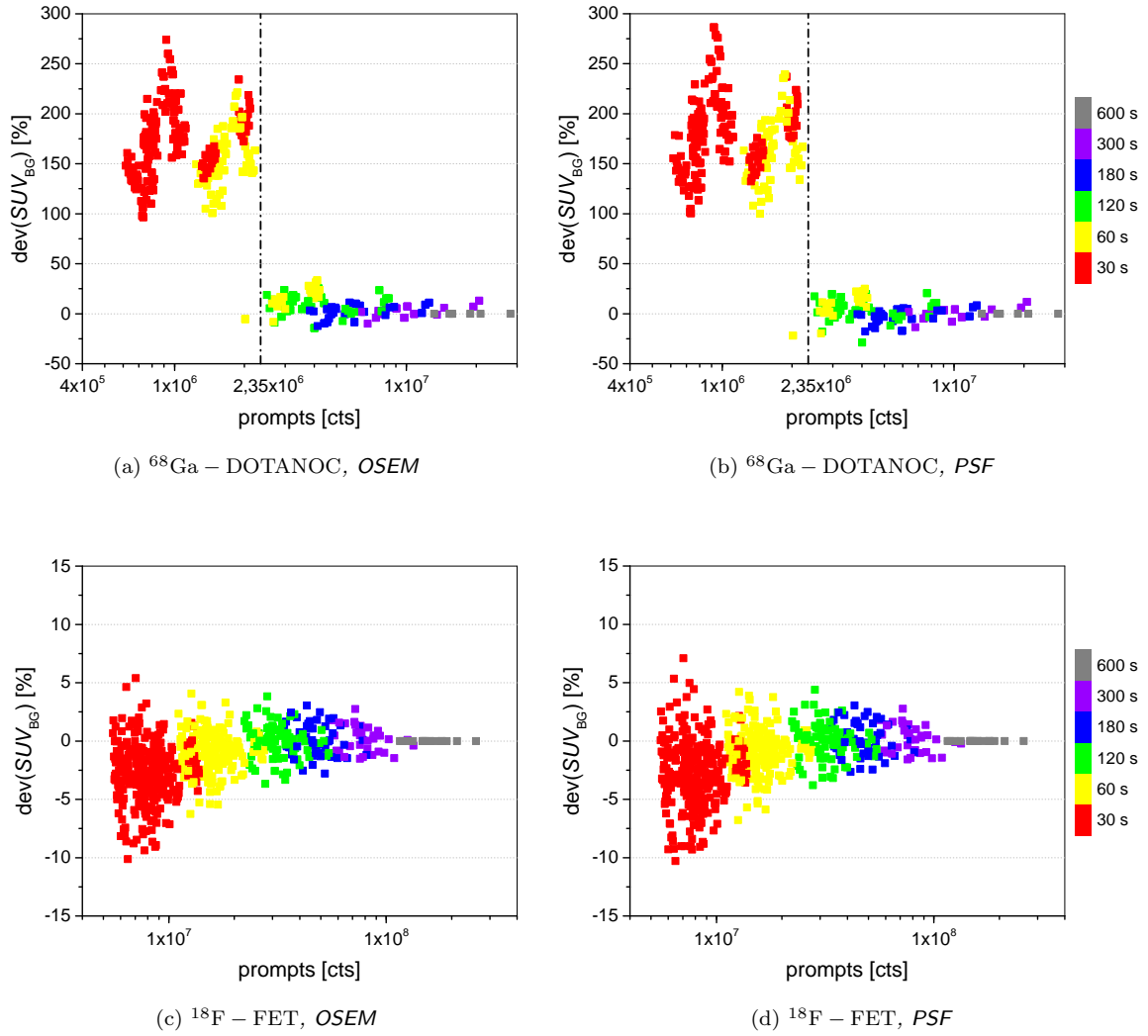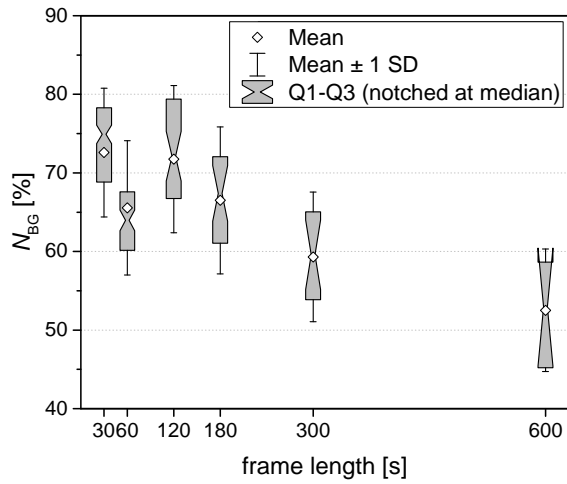
Figure 4.19: *Dependence of background activity SUV_{BG} on the total number of counts (prompts). Data is presented in a lin-log plot for $^{68}\mathrm{Ga} - \mathrm{DOTANOC}$ (top row) and $^{18}\mathrm{F} - \mathrm{FET}$ patients (bottom row), both reconstructed with setting **OSEM** (left column) and **PSF** (right column). Colors indicate different frame lengths, dash-dotted line marks the amount of prompts below which an abrupt increase of SUV_{BG} is observed.*
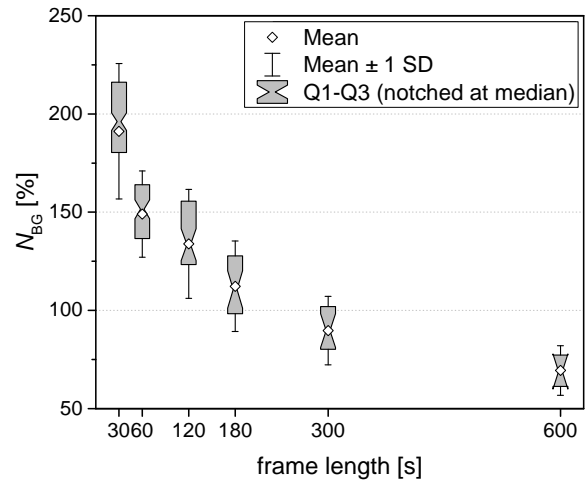
4.2.4 Background Variability

DOTANOC The 10 min acquisitions show an average background variability of 52.5(78) % in the OSEM and 69.4(126) % in the PSF images. For all frame times $\leq 5\,\text{min}$, N_{BG} is significantly different from the reference frame. In the 1 min acquisitions a deviation from the overall tendency (statistical outlier) is visible (Figure 4.20). When reducing acquisition time down to 30 s, background variability increases by 40(19) % to 72.6(82) % in the OSEM reconstructions and by 176(37) % to 191(35) %. As before SUV_{BG} in Subsection 4.2.3, the background variability shows a sharp deviation at around 2.35×10^6 prompts as well. Frames with a prompt count of 3×10^6 show an average background variability of 82 % and 171 % while for frames with 2×10^6 prompts the background variability drops to 56 % and 122 % for OSEM and PSF, respectively. This equals a relative reduction of 32 % and 71 %, again for OSEM and PSF. Figure 4.21 shows the dependence of background variability on the number of prompts for reconstruction method PSF.

FET In images of $^{18}\text{F} - \text{FET}$ patients, the average background variability is notably lower (10.7(24) % and 14.6(23) % with OSEM and PSF, respectively) than in $^{68}\text{Ga} - \text{DOTANOC}$ images. When reducing the frame length, N_{BG} increases on average by 102(31) % for OSEM and 192(30) % for PSF images. The absolute background variability in the 30 s frames is 21.2(39) f and 42.4(70) for reconstruction with OSEM and PSF, respectively. Figure 4.21 visualizes the correlation between background variability and the number of prompts (Pearson correlation of -0.681). Again, the discarded patient $^{18}\text{F} - \text{FET15}$ confirms the behaviour around 2.35×10^6 events as observed in $^{68}\text{Ga} - \text{DOTANOC}$ patients (not shown).
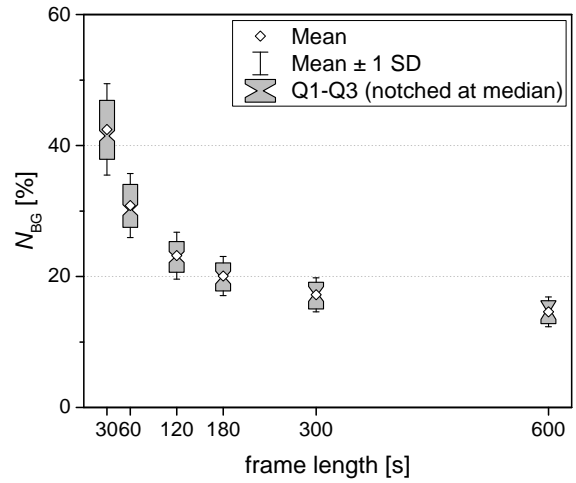
(a) ^{68}Ga − DOTANOC, *OSEM*
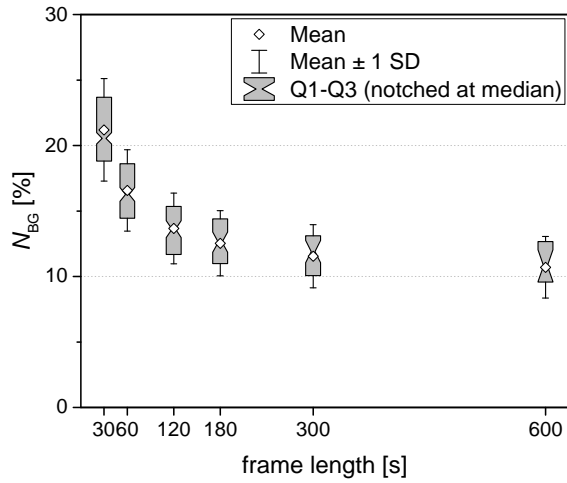
(b) ^{68}Ga − DOTANOC, *PSF*

(c) ^{18}F − FET, *OSEM*

(d) ^{18}F − FET, *PSF*

Figure 4.20: *Background variability N_{BG} versus frame length. Graphs for the 8 ^{68}Ga − DOTANOC (top row) and the 16 ^{18}F − FET patients (bottom row) are given for reconstruction settings OSEM (left column) and PSF (right column). Values are shown as deviations from the 10 min acquisitions in a notched boxplot.*
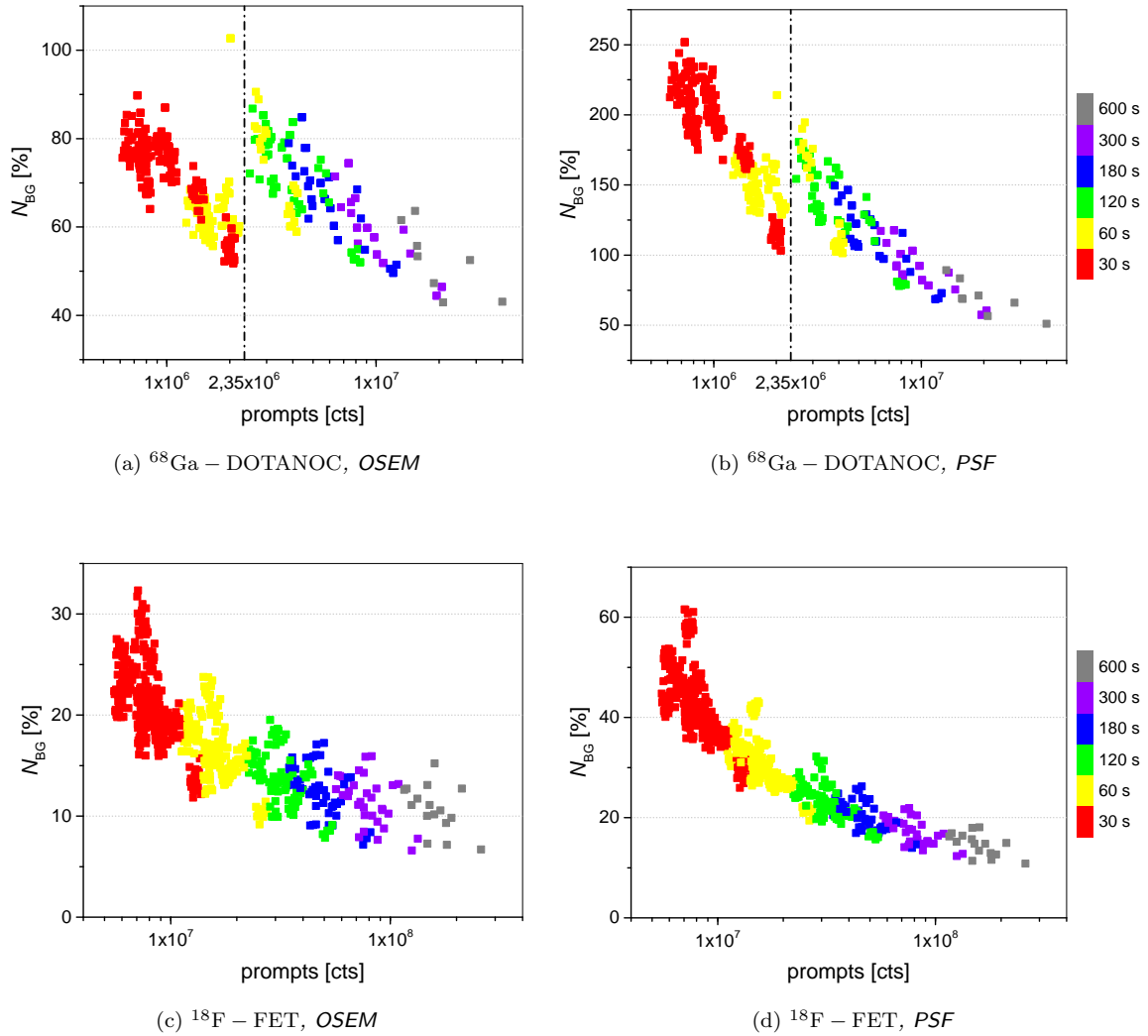
(a) ^{68}Ga − DOTANOC, *OSEM*

(b) ^{68}Ga − DOTANOC, *PSF*

(c) ^{18}F − FET, *OSEM*

(d) ^{18}F − FET, *PSF*

Figure 4.21: *Dependence of background variability* N_{BG} *on the total number of counts (prompts) in a lin-log plot. Results are shown for* ^{68}Ga − DOTANOC *(top row) and* ^{18}F − FET *(bottom row) patients, both reconstructed with* **OSEM** *(left column) and* **PSF** *(right column). Colors indicate different frame lengths, dash-dotted line marks the amount of prompts below which an abrupt increase of* SUV_{BG} *is observed (see Figure 4.19).*

4.2.5 Segmented Volume

Heavy outliers of segmented volumes can be found beyond $\pm 50\%$ of the reference volume, affecting the calculation of the mean strongly. Therefore, the more robust median will be considered for the evaluation of the volume.

DOTANOC Absolute volumes of the segmented regions cover a broad range of approximately 0.3-80 cm^3 (20 min acquisition, 41 % threshold), see Table 4.1. This range corresponds roughly to the volumes covered by the spheres in the phantom (0.21-22 cm^3).

Comparing the two volumes of segmentation with thresholds 41 % and 70 %, reveals a slightly stronger dependence on frame length for VOL_{70}. Figure 4.22 displays the proportion between the two segmented volumes for various frame durations. For the 30 s frames, a significant decrease to the 10 min proportion can be found with PSF reconstruction while for OSEM the difference is not significant. On average, the 70 % threshold recovers 25(6) % and 16(8) % in 20 min acquisitions reconstructed with OSEM and PSF, respectively.
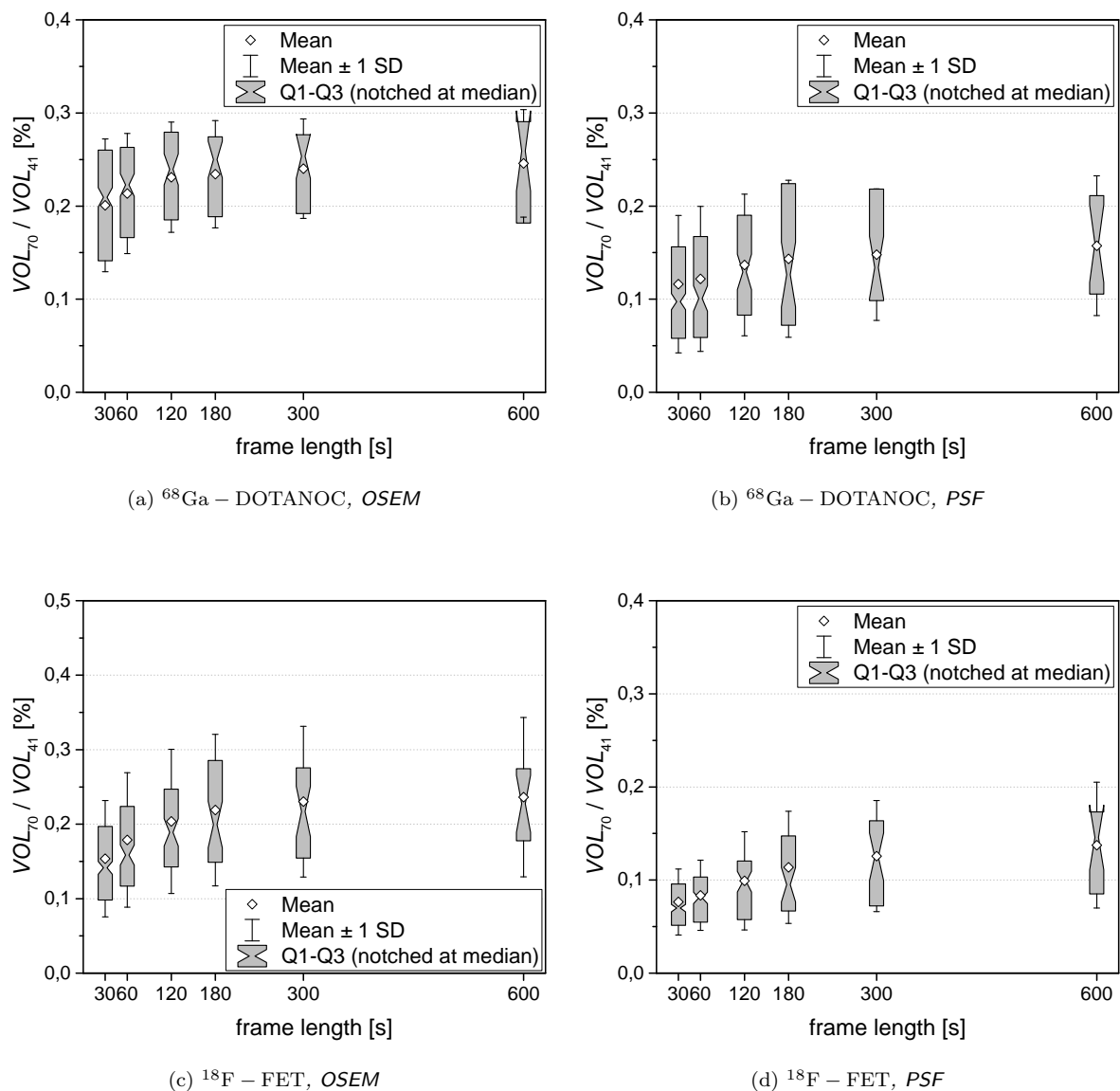

(a) ^{68}Ga − DOTANOC, *OSEM*

(b) ^{68}Ga − DOTANOC, *PSF*

(c) ^{18}F − FET, *OSEM*

(d) ^{18}F − FET, *PSF*

Figure 4.22: *Proportion between* VOL_{70} *and* VOL_{41} *. Shown in notched boxplots for the* 16 *evaluated VOI in* ^{68}Ga − DOTANOC *(top row) and* ^{18}F − FET *(bottom row) patients with reconstruction settings* OSEM *(left column) and* PSF *(right column).*

Generally with reduced acquisition time (or respectively, lower number of counts per frame) we see diverging volumes, as is indicated by the increasing box sizes and error bars in Figure 4.22. On average the segmented volumes VOL_{41} and VOL_{70} decrease with shorter frame times, but especially VOL_{41} and OSEM reconstruction show contrary behaviour for up to 25% of the regions evaluated. This is visualized by the error bars in Figure 4.23 spanning over the x-axis. For VOL_{41} the average deviation from the reference frames is significant for acquisition times $\leq 1\,\mathrm{min}$ and $\leq 3\,\mathrm{min}$ with OSEM and PSF, respectively. The median of VOL_{41} in the $30\,\mathrm{s}$ frames reduces by 10% and 54% compared to the $20\,\mathrm{min}$ frames in OSEM and PSF images, respectively. VOL_{70} is influenced even stronger with a decrease of 24% and 70% for OSEM and PSF.

FET Proportion between volumes of 41% and 70% segmentation show similar results as in $^{68}\mathrm{Ga} - \mathrm{DOTANOC}$ patients: VOL_{70} decreases stronger with acquisition time than VOL_{41}. In the reference frames, VOL_{70} recovers $24(11)\%$ and $14(7)\%$ of VOL_{41} with OSEM and PSF reconstruction, respectively. In the $20\,\mathrm{min}$ frames the volumes (VOL_{41}) of the 16 segmented lesions range from $1\text{-}30\,\mathrm{cm}^3$. Similar to the behaviour in $^{68}\mathrm{Ga} - \mathrm{DOTANOC}$ images with reduced acquisition time, the segmented volumes deviate in either directions, increasing and decreasing values. Especially for very short frame lengths, heavy outliers were detected that influence the mean strongly. As Figure 4.23 shows for VOL_{41}, the mean would suggest a slightly increasing volume for the $30\,\mathrm{s}$ frames while the median signalizes a statistically significant (the notches indicate 5% confidence) decrease of 11%. For the PSF reconstruction the median of VOL_{41} significantly deviates for frame lengths $\leq 2\,\mathrm{min}$ with a reduction of 58% in the $30\,\mathrm{s}$ frames. VOL_{70} shows significant deviations for frame times $\leq 2\,\mathrm{min}$, yielding a decrease of the median of 38% and 77% with OSEM and PSF, respectively.

Table 4.1: *VOL_{41} [cm^3] of all segmented HU-ROIs (tumors, pituitary gland, spheres) measured in the reference frames*

radiotracer	reconstruction	Mean ($\pm$ SD)	Range	
			Lower	Upper
$^{68}\mathrm{Ga} - \mathrm{DOTANOC}$	OSEM	13.5	0.902	77.8
$^{68}\mathrm{Ga} - \mathrm{DOTANOC}$	PSF	8.74	0.327	65.2
$^{18}\mathrm{F} - \mathrm{FET}$	OSEM	9.55	1.00	28.8
$^{18}\mathrm{F} - \mathrm{FET}$	PSF	5.47	4.69	16.7
Phantom	OSEM	6.16	0.39	22.06
Phantom	PSF	5.17	0.21	19.21

$^{18}\mathrm{F} - \mathrm{FET}$ patients: $N = 16$; $^{68}\mathrm{Ga} - \mathrm{DOTANOC}$ patients: $N = 16$; phantom: $N = 6$;
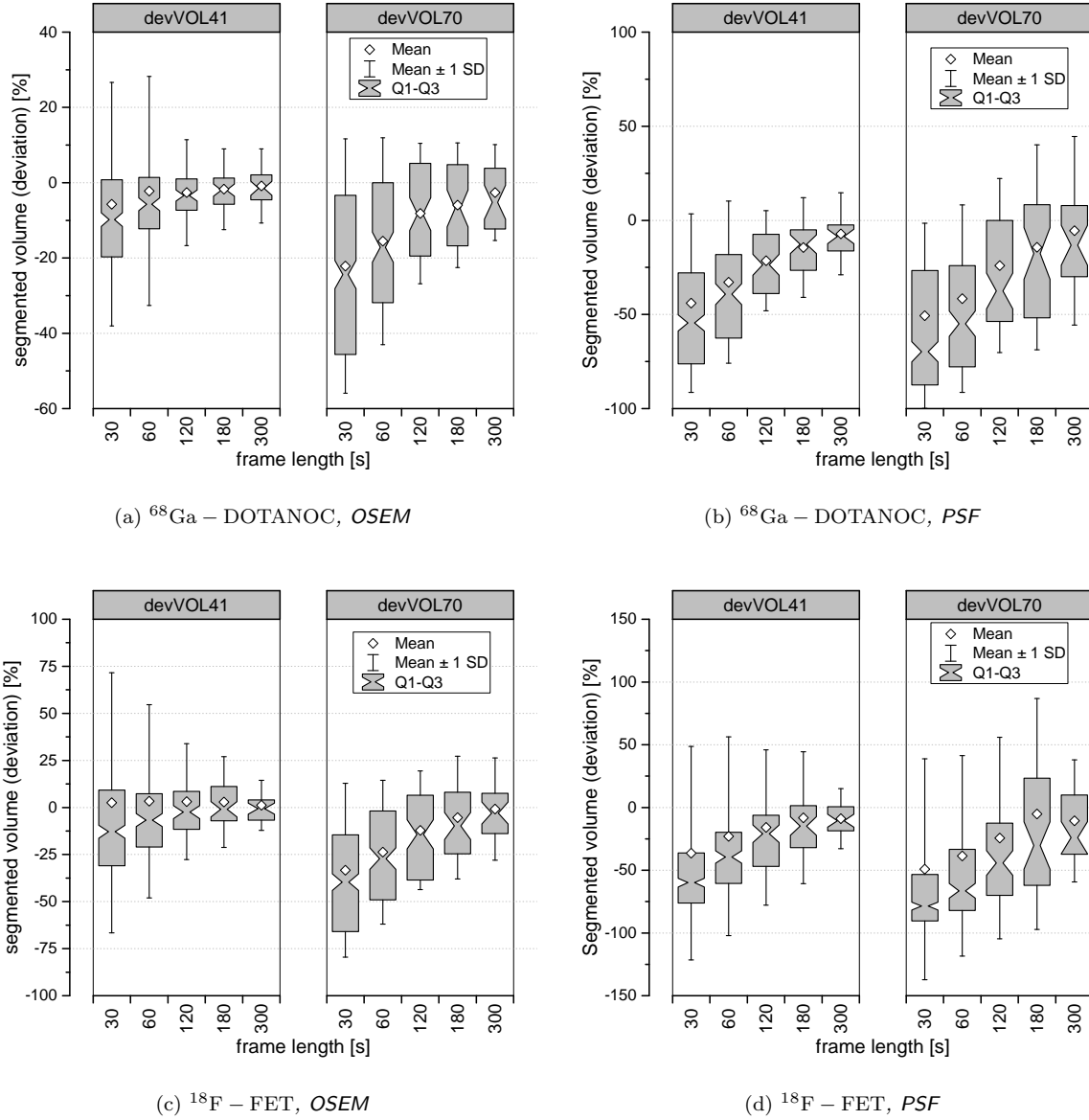
Figure 4.23: *Segmented volumes VOL_{41} and VOL_{70} of the 16 VOI in ^{68}Ga − DOTANOC (top row) and the 16 VOI in ^{18}F − FET (bottom row) patients for reconstruction settings OSEM (left column) and PSF (right column). Values are shown as deviations from the 10 min acquisitions in notched boxplots.*

4.2.6 Standard Uptake Value

^{68}Ga − DOTANOC For the ^{68}Ga − DOTANOC patients, Figure 4.24 shows absolute values of the four evaluated SUVs (SUV_{41}, SUV_{50}, SUV_{70} and SUV_{max}) for the reference and the shortest (30 s) frame, reconstructed with OSEM (for respective figure with PSF reconstruction, see Appendix B). In the reference frames, SUV_{max} ranges widely for both, OSEM (min to max: 2.2-63) and PSF (4.0-93) reconstructions due to a heavy outlier. Median (IQR) of the patient pool for SUV_{max} is 11(12) for OSEM and 20(21) for PSF. SUV_{41}, SUV_{50} and SUV_{70} show significantly lower values, according to the applied thresholds. Although absolute values do differ widely even if cleared from outliers, the deviations for shorter frame lengths present more uniformly. Figure 4.25 shows the dependence of SUV_{max} on frame length for OSEM and PSF. We see continuous increase with shorter frame length, which is statistically significant for SUV_{max} and SUV_{70} with acquisition times ≤ 2 min in OSEM images. SUV_{41} and SUV_{50} first show significant deviations from the reference frame for ≤ 1 min acquisitions in OSEM images. In PSF images, all $SUVs$ increase significantly with the first reduction (≤ 5 min). In the 30 s frames, the

median of SUV_{max} increases by 8.3 % to 12.1 for OSEM and by 49 % to 30 for PSF. Figure 4.26 shows the correlation of SUV_{41}, SUV_{50} and SUV_{70} with the respective SUV_{max} (all values in deviations from the reference frame). The plots visualize, whether the SUV_{41} / SUV_{50} / SUV_{70} deviate stronger or weaker from their respective 10 min value than the SUV_{max} does from its reference value. The graphs plainly show high correlation (Pearson coefficients > 0.999 in all six cases) between the deviations, visible from the narrow distribution of the data points around the linear fits. Further, in the figure for SUV_{41} the linear fit $y = k \cdot x$ to the 30 s points (red solid line) and the identity line (black dashed) are shown. For the linear fit we find the slope k as 0.866 with an R-Square of 0.945. The difference from the linear fit's slope to the identity line visualizes how much weaker (−14 %) the increase of SUV_{41} with acquisition time is compared to the increase of SUV_{max}. For SUV_{41} the median increases from 10 min to 30 s only by 7.1 % compared to 8.3 % for SUV_{max} (OSEM), which resembles the mentioned difference of 14 %. With PSF the difference is even more crucial, where the median of SUV_{max} increases by 49 % compared to 39 % increase of SUV_{41} for reducing acquisition time from 10 min to 30 s. The higher the threshold, the less the difference to SUV_{70}. The influence of reduced acquisition time on SUV_{70} is statistically not significantly different from SUV_{max}.
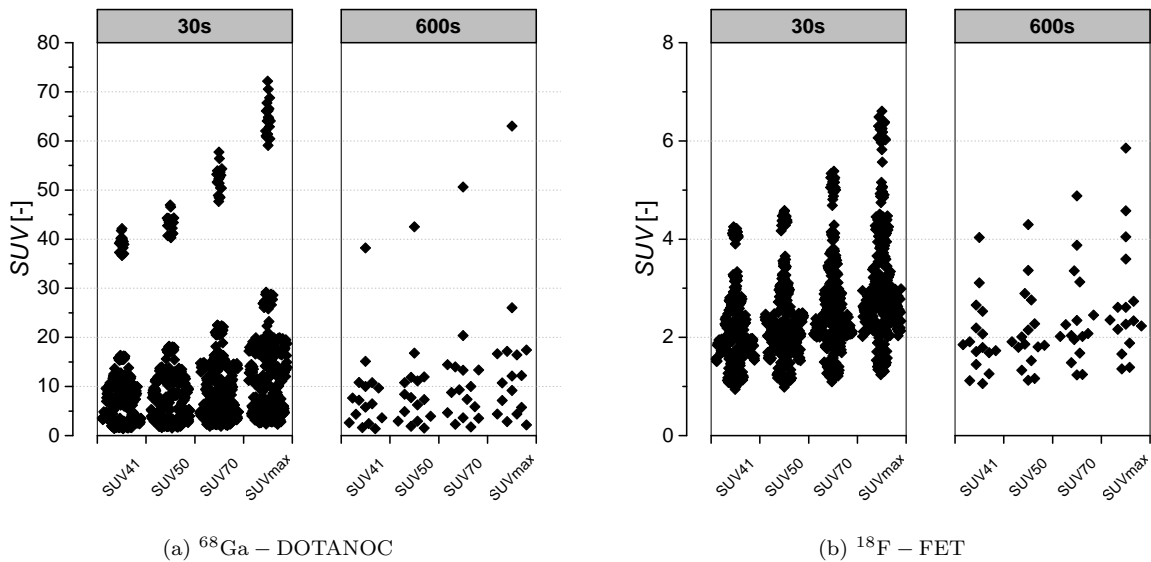

Figure 4.24: *Standardized Uptake Values at different threshold levels in scatter plots where each point represents an evaluated ROI of a region with high uptake (tumor or pituitary gland). Figures (a) and (b) show the results for $^{68}\mathrm{Ga} - \mathrm{DOTANOC}$ and $^{18}\mathrm{F} - \mathrm{FET}$ patient data, respectively. Both groups contain 16 ROIs in the 10 min acquisition and accordingly 320 ROIs in the 30 s acquisitions. Graphs show results for 30 s and 600 s frame lengths with OSEM reconstruction. In both cases, $^{68}\mathrm{Ga} - \mathrm{DOTANOC}$ and $^{18}\mathrm{F} - \mathrm{FET}$ an outlier with significantly higher SUV values is included.*

$^{18}\mathrm{F} - \mathrm{FET}$ Absolute SUV values of the $^{18}\mathrm{F} - \mathrm{FET}$ patients are presented in Figure 4.24 for OSEM reconstruction. In the reference frame, SUV_{max} ranges from 1.4-5.9 with median of 2.3 in the OSEM images, and from 1.7-7.0 with median of 3.2 in the PSF images. The medians (IQR) for SUV_{41}, SUV_{50} and SUV_{70} of all patients are 17(8) %, 14(6) % and 8(3) % lower then the respective SUV_{max}. For the OSEM reconstructions, SUV_{max}, SUV_{50} and SUV_{70} show significant increases for frame lengths ≤ 3 min while SUV_{41} first deviates significantly for frame lengths ≤ 2 min. For the PSF reconstructions, all frames ≤ 5 min are affected significantly by the shorter acquisition time. Reducing acquisition time by a factor of 20 (down to 30 s) induces a 10(14) % increase of median (IQR) SUV_{max} with OSEM and 64(58) % with PSF. While the absolute values of the segmentation SUVs obviously are different from the SUV_{max}, their relative change with acquisition time is not necessarily different from the change of SUV_{max}. The deviations of SUV_{41} and SUV_{50} are with statistical significance different from the
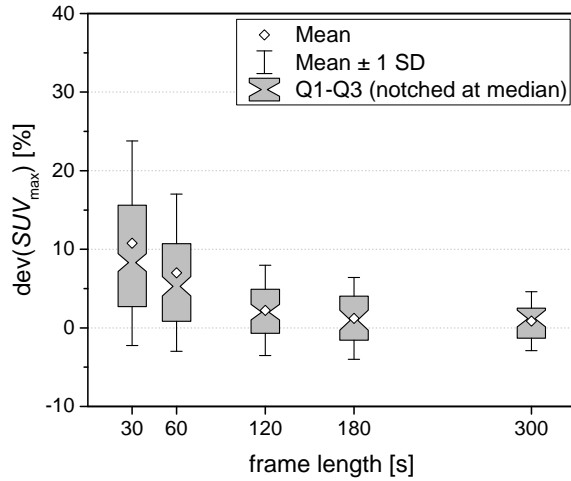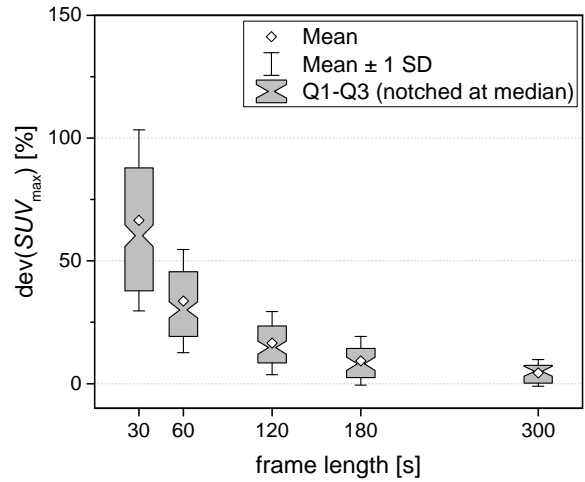
(a) $^{68}\text{Ga} - \text{DOTANOC}$, *OSEM*
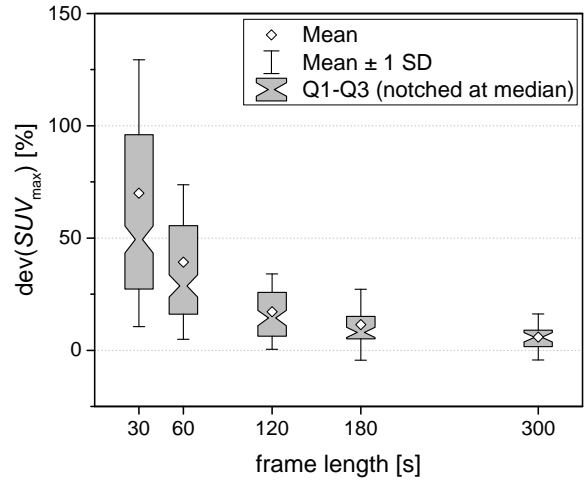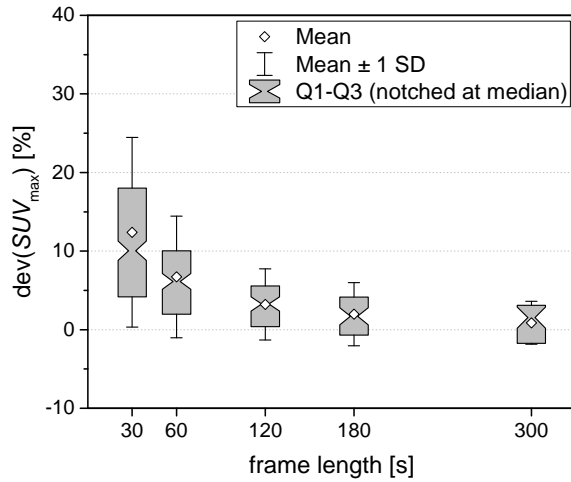
(b) $^{68}\text{Ga} - \text{DOTANOC}$, *PSF*

(c) $^{18}\text{F} - \text{FET}$, *OSEM*

(d) $^{18}\text{F} - \text{FET}$, *PSF*

Figure 4.25: SUV_{max} *of the respectively* 16 *evaluated VOI in* $^{68}\text{Ga} - \text{DOTANOC}$ *(top row) and* $^{18}\text{F} - \text{FET}$ *(bottom row) patients with reconstructions* **OSEM** *(left column) and* **PSF** *(right column). Values are shown as deviations from the* 10 min *acquisitions in a notched boxplot.*

deviation of SUV_{max} while SUV_{70} shows no significant difference. Further, the deviations of SUV_{41} and SUV_{50} are not significantly different from each other. That is to say, shorter frame length induces similar percentage increases to SUV_{41} and SUV_{50}, as well as to SUV_{70} and SUV_{max}. These results are valid for both reconstruction methods. Figure B.2 (see Appendix B) visualizes these correlations in separate scatter plots SUV_{seg} vs. SUV_{max}. The identity line symbolizes equal deviation for SUV_{seg} and SUV_{max}, while slopes < 1 of the linear fits signalize less effect on the respective SUV, which does not necessarily mean statistical significance of the differences. In the **OSEM**-graphs, the linear fit to the 30 s frames shows a slope of 0.55 (R-Square: 0.937) for SUV_{41}, which visualizes the significantly lower influence of acquisition time than on SUV_{max}. To the contrary, linear fit to SUV_{70} yields a slope much closer to the identity (0.87; R-Square: 0.987) emphasizing the results of the statistical analysis. In both cases the correlation of the segmented SUV and SUV_{max} is confirmed by high Pearson's r of 0.968 and 0.993 for SUV_{41} and SUV_{70}, respectively.
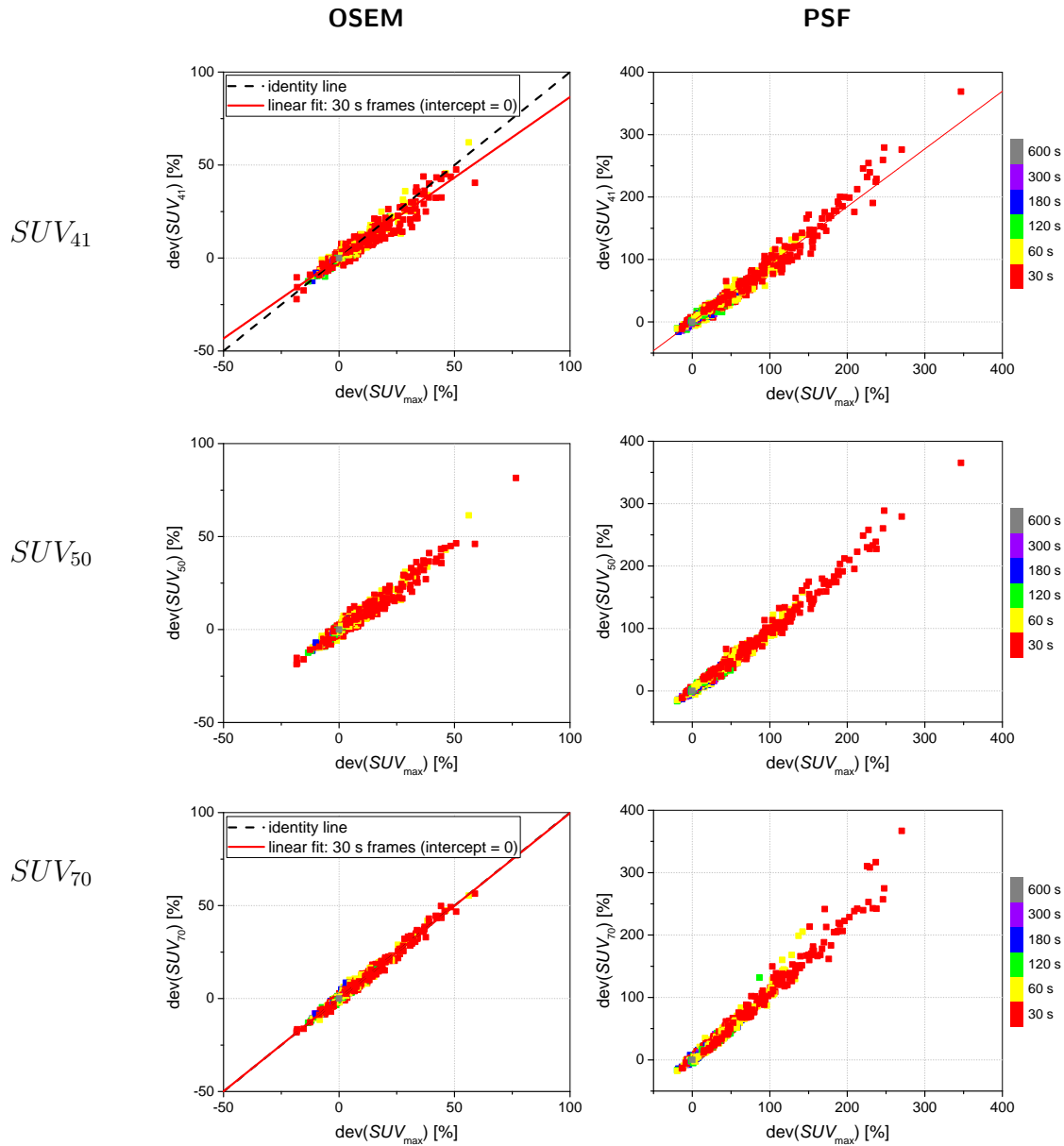
Figure 4.26: *Correlation of SUV_{41}, SUV_{50} and SUV_{70} with the corresponding SUV_{max} in the 16 evaluated VOI of ^{68}Ga − DOTANOC patients. Left column shows evaluation with reconstruction setting OSEM, right column with PSF. Values are plotted as deviations from the 10 min (600 s) frames. Colors indicate different frame lengths. For according images of ^{18}F − FET patients see Appendix B.*

4.2.7 Lesion-to-Background Ratio

DOTANOC In the reference frame, LBR_{max} ranges from 17-520 (median: 96) with OSEM reconstruction and from 34-806 (205) in PSF. LBR_{max} deviates significantly from the reference value for frame times $\leq 2\,\mathrm{min}$ with OSEM and $\leq 5\,\mathrm{min}$ with PSF. The median of LBR_{max} declines by 61 % to 38 with OSEM and by 47 % to 105 with PSF reconstruction. The sudden change of the background activity from 2 min to 1 min, as observed in Subsection 4.2.3, translates to the LBR as well (see Figure 4.27). Although the statistical tests reveal no significant difference, in the PSF images LBR_{max} first rises by up to 15 % for acquisitions 5 min, 3 min and 2 min before dropping significantly as just mentioned.

FET In the 20 min acquisitions of ^{18}F − FET patients, LBR_{max} ranges from 1.8-5.6 (median: 2.3) in OSEM images and from 2.3-7.2 (3.1) with PSF reconstruction. LBR_{max} deviates significantly from the 20 min frame for acquisition times $\leq 3\,\mathrm{min}$ with OSEM and $\leq 5\,\mathrm{min}$ with PSF. In contrast to

^{68}Ga − DOTANOC images, *LBR increases* by 14 % to median(IQR) 2.8(12) and by 65 % to 5.7(26) in OSEM and PSF images, respectively. With shorter frame times, the variation of individual LBR_{max} values increases as well, as indicated by the respective bigger boxes in Figure 4.27.
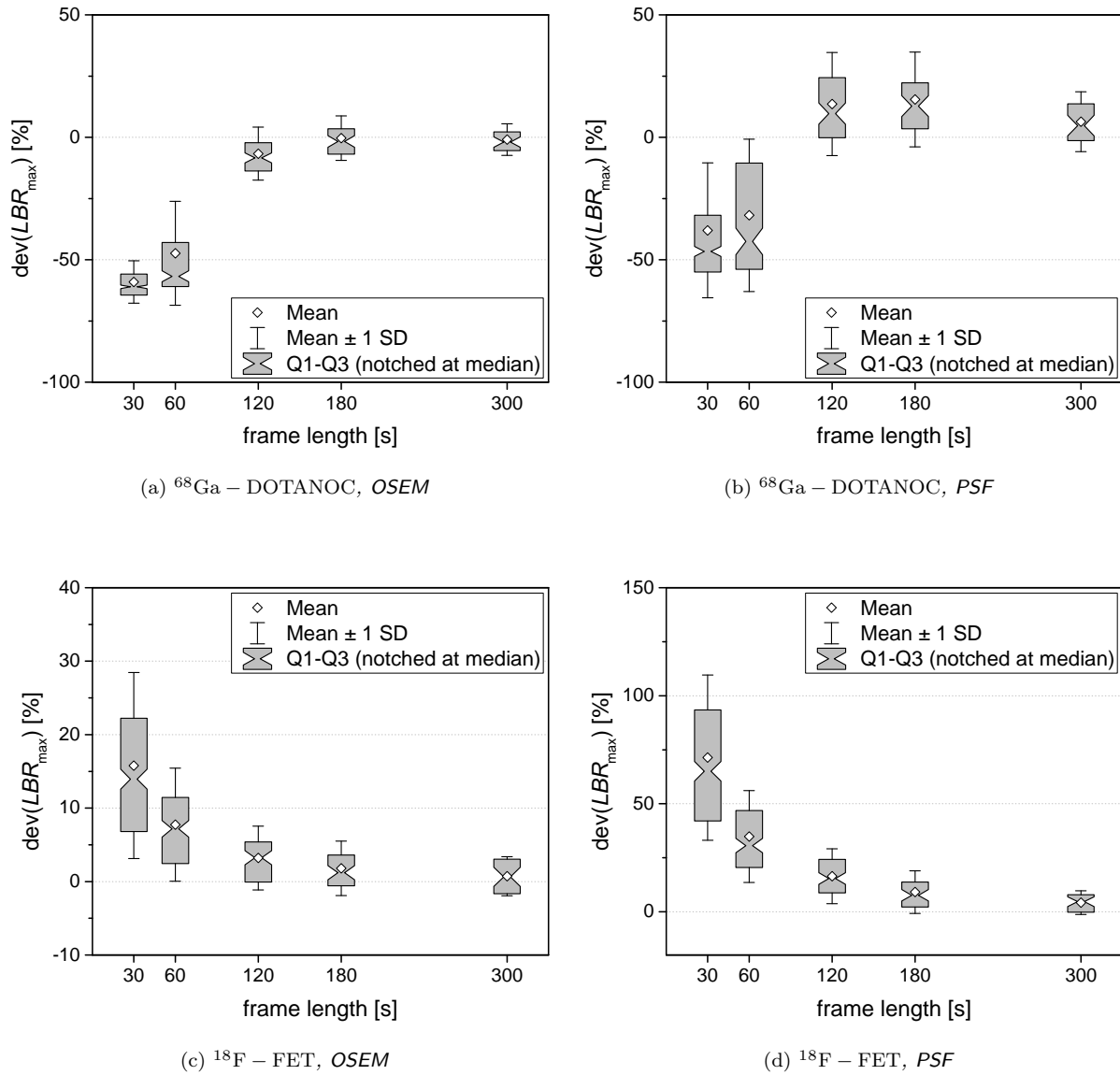

(a) ^{68}Ga − DOTANOC, *OSEM*

(b) ^{68}Ga − DOTANOC, *PSF*

(c) ^{18}F − FET, *OSEM*

(d) ^{18}F − FET, *PSF*

Figure 4.27: *LBR_{max} of the 16 evaluated VOI in ^{68}Ga − DOTANOC (top row) and ^{18}F − FET (bottom row) patients with reconstructions OSEM (left column) and PSF (right column). Values are shown as deviations from the 10 min acquisitions in a notched boxplot.*

4.2.8 Signal-to-Noise Ratio

DOTANOC In the reference frame, SNR_{max} ranges from 27-846 (median: 219) with OSEM reconstruction and from 41-904 (median: 353) in PSF. With both reconstruction methods, SNR_{max} deviates significantly for all frame times. The median of SNR_{max} declines by 73 % to 57 with OSEM and by 81 % to 62 with PSF reconstruction. SNR_{max} of the 1 min frames shows higher variation due to the discontinuity in the background variability (see Figure 4.28), visible for both, OSEM and PSF reconstructions.

FET In the 20 min acquisitions of ^{18}F − FET patients, $SNR_{\max}$ ranges from 12-58 (median: 21) in OSEM images and from 13-54 (median: 22) with PSF reconstruction. As for the ^{68}Ga − DOTANOC patients, $SNR_{\max}$ deviates significantly for all reduced frame times of OSEM and PSF images. As shown in Figure 4.28, $SNR_{\max}$ decreases steadily with reduced acquisition time. For 30 s acquisitions, $SNR_{\max}$ drops by 41 % and 43 % for OSEM and PSF reconstructions. In the images we then find the median(IQR) of $SNR_{\max}$ to be 14(9) and 13(6) for OSEM and PSF, respectively.
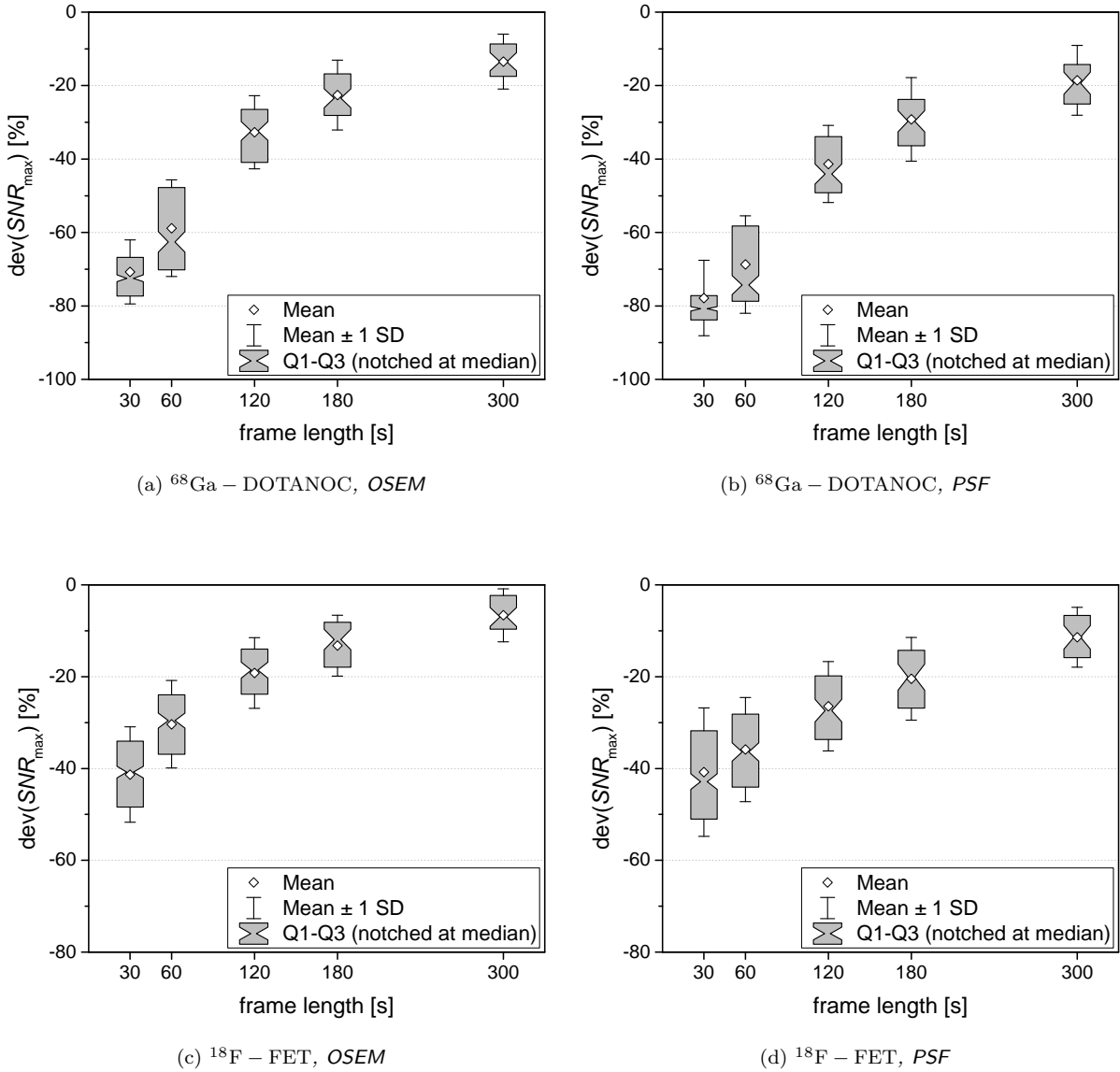

Figure 4.28: *Signal-to-Noise-Ratio* $SNR_{\max}$ *of the* 16 *evaluated VOI in* ^{68}Ga − DOTANOC *(top row) and* ^{18}F − FET *(bottom row) patients with reconstructions* **OSEM** *(left column) and* **PSF** *(right column). Values are shown as deviations from the* 10 min *acquisitions in a notched boxplot.*

4.2.9 Correlation between Figures of Merit

In this section, a short visual presentation of the correlations between several figures of merit shall be given. For the segmented volume, by means of VOL_{41}, we find certain dependence on $SUV_{\max}$, as illustrated by Figure 4.29 for PSF reconstruction: the higher the deviation of $SUV_{\max}$, the lower the segmented volume. And if $SUV_{\max}$ decreases, the segmented volume most certainly increases as well.
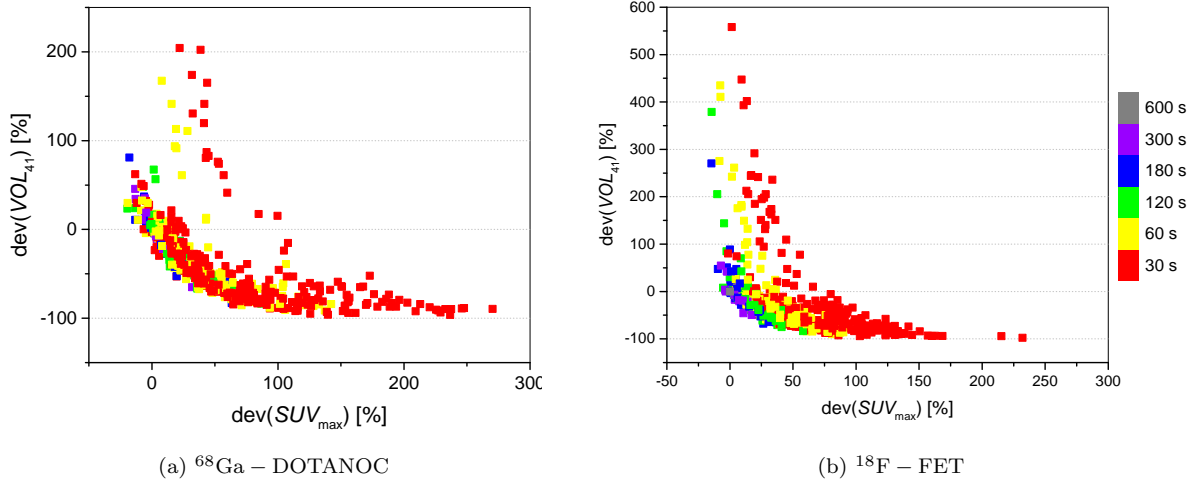
(a) ^{68}Ga − DOTANOC

(b) ^{18}F − FET

Figure 4.29: *Dependence of segmented volume VOL_{41} on maximum voxel value $SUV_{\max}$, both expressed as deviations, is shown for ^{68}Ga − DOTANOC (a) and ^{18}F − FET (b) with reconstruction setting PSF. Frame length is indicated by different colors.*

Figure 4.30 shows the correlation between $LBR_{\max}$ and $SNR_{\max}$ (both as deviations from the reference frame), which basically represents the relation between a_{BG} and N_{BG}, showing completely different behaviour for ^{68}Ga − DOTANOC and ^{18}F − FET images. In the ^{68}Ga − DOTANOC patients we find a separation between the low- (short acquisition) and the high-count (long acquisitions) images, with threshold at approximately 2.35×10^6 recorded prompts in the whole acquisition. The high-count images show deviations of $LBR_{\max}$ around zero, while the low-count images have high negative deviations. In the ^{18}F − FET patients, little deviation of $SNR_{\max}$ correlates to close to zero deviation of $LBR_{\max}$, which is satisfied for long acquisitions. Reduction of acquisition time implies for one reduction of $SNR_{\max}$ as well as increase of $LBR_{\max}$, which do correlate indirectly as the figures confirm.
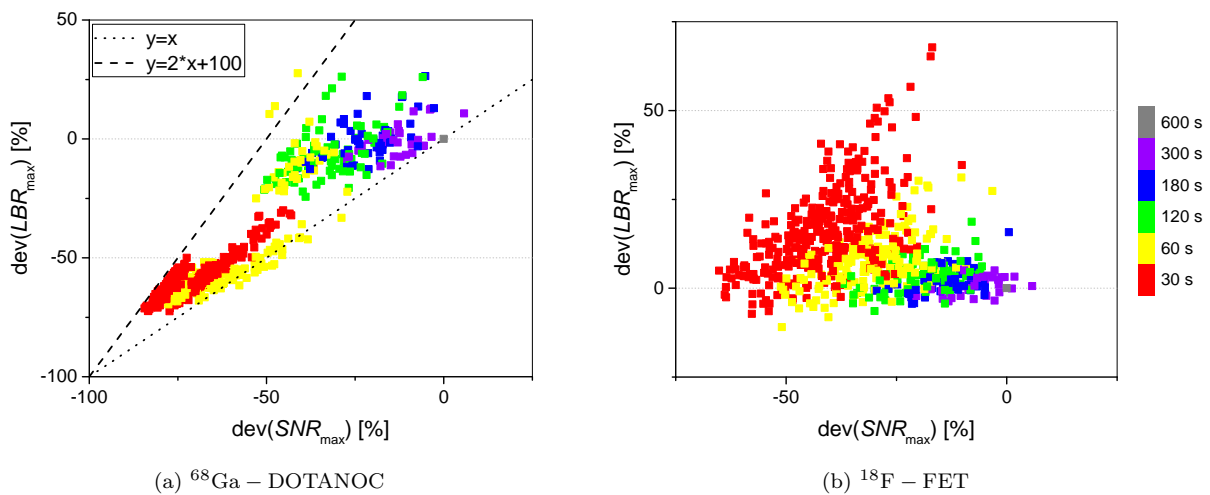

(a) ^{68}Ga − DOTANOC

(b) ^{18}F − FET

Figure 4.30: *Correlation between $LBR_{\max}$ and $SNR_{\max}$, both expressed as deviations, is shown for ^{68}Ga − DOTANOC (left) and ^{18}F − FET (right) with reconstruction setting OSEM. Frame length is indicated by different colors. Dotted line describes the identity line ($y = x$), dashed line gives $y = 2 \cdot x + 100\,\%$.*

Figure 4.31 demonstrates the relation between $LBR_{\max}$ and $SUV_{\max}$, which is a derivative

of the more fundamental correlation of a_{BG} and the "SUV-denominator" ($\frac{A_{\mathrm{adm}}}{BW}$). As supposed, for the $^{18}\mathrm{F} - \mathrm{FET}$ patients, we clearly see a direct and linear correlation. On the other hand, for the $^{68}\mathrm{Ga} - \mathrm{DOTANOC}$ patients there is a high discrepancy for low-count images and high-count images. This is not because of the different tracer but reasoned in the low-count statistics. We expect to observe similar behaviour in $^{18}\mathrm{F} - \mathrm{FET}$ patients for similarly low countrates as well. This should be addressed in a follow-up study.
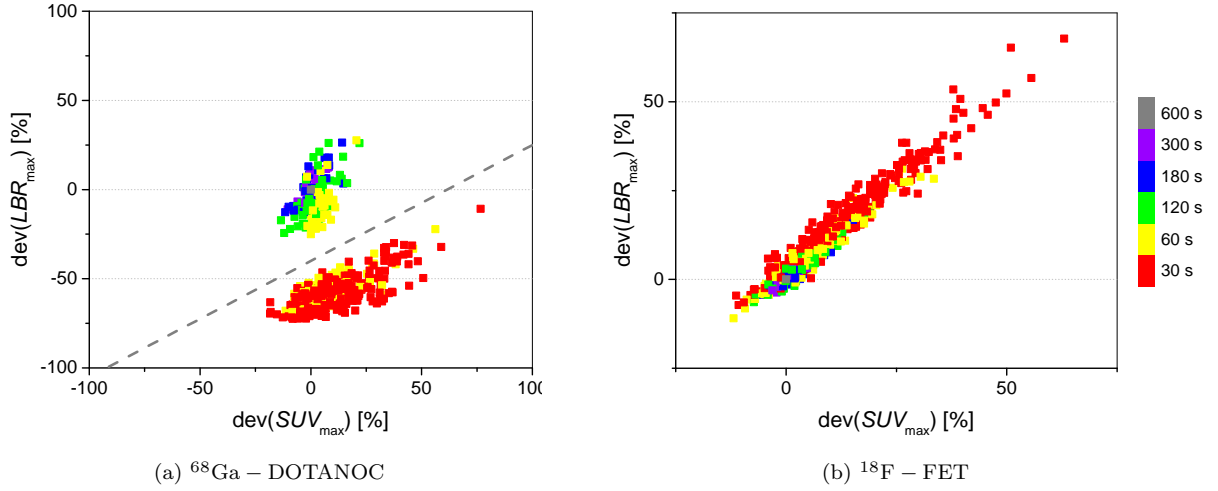

(a) $^{68}\mathrm{Ga} - \mathrm{DOTANOC}$ (b) $^{18}\mathrm{F} - \mathrm{FET}$

Figure 4.31: *Correlation between LBR_{max} and SUV_{max}, both expressed as deviations, is shown for $^{68}\mathrm{Ga} - \mathrm{DOTANOC}$ (left) and $^{18}\mathrm{F} - \mathrm{FET}$ (right) with reconstruction setting **OSEM**. Frame length is indicated by different colors. Dashed line in the $^{68}\mathrm{Ga} - \mathrm{DOTANOC}$ graph visualizes the observed inhomogeneity at 2.35×10^{6} prompts recorded. Difference between the tracers is due to the background region used for the evaluation. In $^{18}\mathrm{F} - \mathrm{FET}$, the background was a region with significant activity, while in the $^{68}\mathrm{Ga} - \mathrm{DOTANOC}$ the activity in the background was almost zero.*

Most interestingly, we see the correlation between SUV_{max} and the background variability N_{BG} in Figure 4.32. This confirms, that higher background variability directly contributes to higher SUV_{max} values in several cases. But the second even more important point is the confirmation of the degraded accuracy directly caused by higher background variability. For low N_{BG} we find only little deviations of SUV_{max}, that means, high accuracy between patients and for slight reductions of acquisition time. On the other hand, with high N_{BG} the SUV_{max} values deviate between $-15\,\%$ and $70\,\%$ which signalizes low accuracy for different measurements. Finally, as very short acquisition time by tendency relates to higher N_{BG}, we can state, that this relates to less accuracy as well.
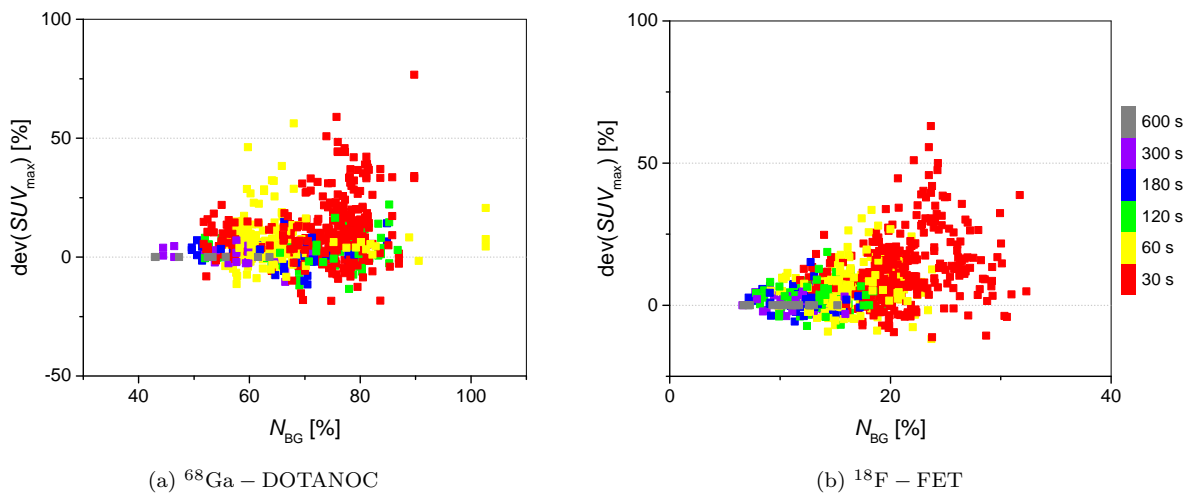
(a) ^{68}Ga − DOTANOC

(b) ^{18}F − FET

Figure 4.32: *Correlation between $SUV_{\max}$ (deviation) and background variability N_{BG} is shown for ^{68}Ga − DOTANOC (left) and ^{18}F − FET (right) with reconstruction setting OSEM. Frame length is indicated by different colors.*

Chapter 5

Summary and Discussion

The results from the previous chapter are first briefly summarized (Section 5.1), before going deeper into discussion. Section 5.2 and Section 5.3 treat phantom and patient data separately, followed by the comparison between these two measurements (Section 5.4) and to the literature (Section 5.5). Implications of the work in the last section complete this chapter. With the here presented discussion of the results, this chapter bridges to the final conclusions in the following chapter.

5.1   Summary of Results

Focus of this study was to evaluate the change of several quantitative image measures with reduced scan duration. Although the acquisition time of the reference frame was different for phantom (20 min) and patient measurements (10 min), the shortest scan time was accordingly adapted (1 min and 30 s, respectively) to fit one-twentieth of the reference. Beside absolute values of the measures, relative values were calculated, expressed in % deviation from the value in the reference frame.

In Table 5.1 the average deviations from the shortest to the reference frame are summarized for most measures (columns "Deviations"). Additionally, the first frame length (in min) for which the average deviation was significantly ($P < 0.01$) different from the reference (zero deviation), is listed in the columns "1$^{\text{st}}$ sign.". Background activity increases with reducing frame length in the phantom and ^{68}Ga − DOTANOC patients while it decreases in the ^{18}F − FET patients. Noise increases for all measurements, in PSF images distinctly stronger than in OSEM acquisitions. This increase induces partly strong increases of $RC_{\max}$ and $SUV_{\max}$ values, and weaker or even nonsignificant deviations for RC_{41} and SUV_{41}. In PSF images the changes are considerably higher and significance of deviations is reached largely for reduction of acquisition times below 50 %. High variations of SUV values of different patients were found. In patients, the segmented volume VOL_{41} shows high variations but only slight increases that are significant just at the shortest frame lengths. Volume segmentation of spheres is highly dependent on partial volume effects, showing high positive deviations for the 10 mm sphere but notable negative deviations for the 37 mm sphere. $SNR_{\max}$ showed heavy changes with reductions of up to 70 % in both patient groups and $LBR_{\max}$ with similar decreases in ^{68}Ga − DOTANOC but slight increases in ^{18}F − FET patients due to minimally sinking background activity and rising maximum activity. In the phantom measurements, quantifications of 10 mm and 37 mm spheres were different for the most part. While spheres as small as 10 mm are hugely influenced by partial volume effects, the changes in big spheres are highly noise dependent. Deviations of ^{68}Ga − DOTANOC and ^{18}F − FET patients were mostly different, especially for background activity and image noise, as well as lesion-to-background and signal-to-noise ratios. This mismatch was mainly introduced by the highly varying background activity in ^{68}Ga − DOTANOC patients.

66

Table 5.1: *Summarizing results: deviations of average when reducing acquisition time by a factor of 20 (phantom: 20 min to 1 min; patients: 10 min to 30 s) and acquisition time [min] for which deviations are initially significantly different from the reference.*

Measure	Data source	OSEM		PSF	
		Deviation [%]	1st sign.* [min]	Deviation [%]	1st sign.* [min]
a_{BG}	Phantom	5.6(6)	5	5.5(6)	5
	^{68}Ga $-$ DOTANOC	173(34)	2	173(34)	2
	^{18}F $-$ FET	$-3(2)$	1	$-3(2)$	2
N_{BG}	Phantom	100	5	200	5
	^{68}Ga $-$ DOTANOC	40(19)	5	176(37)	5
	^{18}F $-$ FET	102(31)	5	192(30)	5
VOL_{41}	Phantom 37 mm	-11	2	-65	3
	Phantom 10 mm	122	1	137	1
	^{68}Ga $-$ DOTANOC	10	1	54	3
	^{18}F $-$ FET	11	0.5	58	2
RC_{max}	Phantom 37 mm	12	2	56	3
	Phantom 10 mm	< 2	NS	20	1
RC_{41}	Phantom 37 mm	< 1	NS	28	3
	Phantom 10 mm	< 2	NS	< 11	NS
RC_{mean}	Phantom 37 mm	-3	5	-2	5
	Phantom 10 mm	< 2	NS	< 1	NS
LBR_{max}	^{68}Ga $-$ DOTANOC	-61	2	-47	5
	^{18}F $-$ FET	14	3	65	5
SNR_{max}	Phantom 37 mm	-67	5	-78	5
	Phantom 10 mm	-70	5	-76	5
	^{68}Ga $-$ DOTANOC	-73	5	-81	5
	^{18}F $-$ FET	-41	5	-43	5
SUV_{max}	^{68}Ga $-$ DOTANOC	8.3	2	49	5
	^{18}F $-$ FET	10	3	64	5
SUV_{41}	^{68}Ga $-$ DOTANOC	7.1	1	39	5
	^{18}F $-$ FET		2		5

NS = not significant, deviations are not even significant for the shortest acquisition time

*1st sign. (first significance) is the highest acquisition time for which the measure deviates significantly

Generally, measures based on the maximum voxel activities are influenced stronger by reduction of scan duration than the same measures calculated with average activities from 41 % threshold segmentation. Image noise (or background variability in patient studies) increases in all measurements with high correlation to the reduction of counts in the image, or similarly shorter frame length. Due to higher noise, PSF images show intensified deviations compared to the same image with strong post-smoothing (OSEM). SNR values decrease proportional to the image noise with shorter scan durations.

5.2 Discussion of Phantom Evaluation

The negligible difference between the measured activity concentration a_{BG} in the 20 min images and the truly administered concentration of $< 1\%$ (OSEM and PSF), validates the high quantitative accuracy in the reference acquisition. As we saw by comparison of different sphere sizes, the noted misalignment of two spheres (13 mm and 22 mm) did not produce notable differences of absolute RC-values, neither did it significantly affect the evaluation of deviations. This was confirmed by comparing the evaluated

values to the results of interpolation between adjacent spheres.

In the phantom measurements we identified significant impact of partial volume effects. The evaluation of partial volume correction (PVC) was not performed in this work, because although several approaches for PVC have been proposed in the literature (Soret et al., 2007; Rousset et al., 2007; Meltzer et al., 1999), the adoption of PVC in clinical routine is still an open issue (Erlandsson et al., 2012). Nevertheless, some crucial findings shall be discussed in the following, as they expand to the influence of acquisition time as well.

Impacts of PVE on the phantom measurements are well visualized by the two line-profiles in Figure 4.2. First, the slopes of the activity distributions are steeper in PSF than in OSEM, what improves visual detectability. Second, the total spill-out is perceptibly less in all frame times for PSF. And third, the peak of the activity distribution ($RC_{\max}$) is significantly higher in the bigger spheres and closer to the true value in the smaller spheres (PSF). Overall, reconstruction with resolution recovery (PSF) clearly reduces PVE, what we can see in better visual representation of the spheres and improved detection at least in the reference frame. In shorter acquisitions, noise equalizes or even reverses the improvements. Interesting is the fact, that PVE masks or even dominates the effect caused by reducing acquisition time. While we do see influence of acquisition time on the biggest sphere, where PVE is still manageable, in the smallest sphere, where PVE is crucial, there is hardly any significant effect of shorter frame lengths. This might be particularly important for the interpretation of the patient data, as tumors of all sizes (1-29 cm^3 with 41 % segmentation) were pooled and evaluated together. Eventually this means, that with good PVE-correction we could expect even higher influence of reduced acquisition time - or in other words, SUV-values of smaller tumors might appear stable when reducing acquisition time, while they are in fact just greatly underestimated because of PVE.
All together, this confirms findings of Boellard et al that SUV-values showed strong variations with tumor size, which in non-smoothed data were due to noise and in smoothed data due to PVE (Boellaard et al., 2004).

In the phantom measurements, we were able to control the accuracy of the segmentation algorithm by comparing the results of the segmentation at various thresholds (41 %, 50 % and 70 %) to the known volumes of the spheres. Amongst several delineation methods VOL_{41}, as used in this study, was found the most accurate algorithm in terms of volume segmentation (Firouzian et al., 2014; Tylski et al., 2010). Still, the actual threshold for recovering the full lesion volume is individual for patients and tumors and is very sensible to factors as lesion size, reconstruction settings, post-filtering and noise level (Ford et al., 2006), creating the need for more sophisticated algorithms (Hofheinz et al., 2013). It was shown (Ford et al., 2006), that as little as 5 % change in the threshold contour level might cause changes in segmented volume of up to 200 %. Our results confirm the draw-backs of the used segmentation method. Recovered volume is by tendency lower for all sphere sizes in PSF images, what is induced by the higher noise level. While the recovered volume in the OSEM reference image is similar for all sphere sizes, the behaviour for shorter acquisition times is completely opposite. The biggest spheres are generally underestimated, while the smallest spheres are overestimated by up to 250 % with a big variation of outcomes. This behaviour combines several effects induced by shorter frame length. First, higher noise in the background elevates the surrounding activity (spill-out) and elevates the possibility of neighbouring voxels to be included into the delineated volume. Second, noise in the sphere influences the maximum voxel value significantly, and as we found increases of $RC_{\max}$ between 10 % and 70 %, this is a major source of uncertainty for accurate volume recovery. Third, reduced activity recovery due to PVE translates directly into the segmentation algorithm and therefore influences the size of the segmented volume crucially. These explanations as well support the observation that volumes in non-smoothed images (PSF) are effected stronger by reduction of acquisition time than in the respective post-filtered images (OSEM). Additionally, segmentation with

50 % and 70 % thresholds were analysed. VOL_{50} resulted in slightly worse volumes than VOL_{41}, favouring the latter. VOL_{70} was found insufficient for actual volume comparison due to the small absolute volumes segmented by this threshold. Realising the mentioned problems, the results for volume segmentation of patient data generally have to be interpreted very carefully, taking into account the performance of the segmentation algorithm for the respective tumor size. Although we lack comparison to other methods, the phantom results clearly suggest necessary improvements of volume segmentation algorithms. In patient data, we found the opposite behaviour of small and big tumors with shorter acquisition time regarding segmented volume (Figure 4.23). Especially in the OSEM images both cases, increasing and decreasing volume, appear. As classification by absolute tumor volume was not intended initially, statistical analysis with classification by absolute tumor volumes are proposed for follow-up research.

5.3 Discussion of Patient Evaluations

Within the 20 different 30 s frames of a single patient, N_{BG} and SUV_{max} vary just randomly and no significant correlation to the absolute counts, or equally the elapsed time, was found. This confirms our assumptions of negligible tracer kinetics within the observed time of 10 min.

The background variability is a widely used but simple measure for image noise with some implications that degrade the comparability between patients. Due to different tumor locations, the definition of the BG-ROIs had to be done manually in different locations for each patient. This introduces a variance between patients, first because of the varying locations of the ROIs and second because of individual anatomical structures, additionally to variances of tracer uptake in the background. In the phantom, the background is uniformly and statically filled with activity, while in patient measurements tracer kinetics and biological processes can play a role.

In patient images with a total number of prompts below approximately 2×10^6, we found a significant discontinuity in the dependence of a_{BG} (Figure 4.19) and N_{BG} (Figure 4.21) on the frame time. Only some $^{68}\text{Ga} - \text{DOTANOC}$ images presented counts below 2×10^6 prompts, due to the lower injected activity and the longer post-injection time compared to $^{18}\text{F} - \text{FET}$ and phantom data. The nature of this sudden increase (SUV_{BG}) and decrease (N_{BG}) is not yet completely verified, but poor performance of scatter correction combined with the above mentioned positivity constraint are the most probable causes. Further investigations with different reconstruction algorithms (e. g. FBP) have to be conducted to verify this suspicion. FBP was repeatedly reported (Bélanger et al., 2004; Reilhac et al., 2008) as a reliable alternative to MLEM-based algorithms when reconstructing low-count images.

Contrary to the evaluated measures N_{BG}, LBR and SNR, SUV_{max} was found to be an accurate measure when reducing acquisition time to a third ($^{18}\text{F} - \text{FET}$) or a fifth ($^{68}\text{Ga} - \text{DOTANOC}$) in OSEM. As the most accurate measure emerged SUV_{41} with stable accuracy down to a fifth in $^{18}\text{F} - \text{FET}$ or even a tenth in $^{68}\text{Ga} - \text{DOTANOC}$ of the reference time or reference activity in OSEM. Overall, smoothing of the images supported the quantitative accuracy of images to a large extent. Generally , PSF was found to be influenced stronger by reduction of acquisition time, mostly due to the increasing noise in images with less counts.

In $^{68}\text{Ga} - \text{DOTANOC}$ patients the behaviour of SUV_{BG} with shorter frame times is justifiable by two factors: the biological process that drives the tracer uptake and the behaviour of the reconstruction algorithm at very low count numbers. $^{68}\text{Ga} - \text{DOTANOC}$ is only taken up into brain tissue when the blood-brain-barrier is disrupted (Sharma et al., 2013), which is the case in the present tumor tissue but of course not in the uniform regions. Consequently, the uptake in the BG-ROIs is marginal with $< 100 \, \text{Bq} \, \text{ml}^{-1}$, which equals approximately 50 decays per voxel and minute, or equally not even 1

decay per second in an area of $2\,\text{mm} \times 2\,\text{mm} \times 2\,\text{mm}$. The huge relative increase of up to $+200\,\%$ of SUV_{BG} amounts just to around $100\,\text{Bq}\,\text{ml}^{-1}$ in absolute numbers. This positive bias originates from the positivity constraint of the MLEM-based reconstruction algorithm that is implemented to not generate negative counts in sinogram bins when scatter correction and randoms estimations would exceed the prompt rate (Reilhac et al., 2008).

In $^{68}\text{Ga} - \text{DOTANOC}$ patients we generally found close to zero background activity, a circumstance that increases detectability and separability of tumors vastly. On the other hand, reduction of acquisition time and/or counts influences background and noise heavily. Consequently, the sensitivity of measures as SNR and LBR to reduction of acquisition time, especially with PSF, is very high. Accuracy and reproducibility of those measures are consequently low, what suggests the need of different or complementary figures in $^{68}\text{Ga} - \text{DOTANOC}$ images. Further, literature on the relation between segmented and true volume is still limited, that's why the accuracy of volume measures in $^{68}\text{Ga} - \text{DOTANOC}$ patients is not assured yet either. Noise measures, LBR and SNR were all found to be very prone to slight changes of acquisition time, showing high deviations, low accuracy, low stability and consequently low reproducibility. Nevertheless, the absolute values confirm the visual inspections. LBR_{max} of up to 100-200 combined with SNR_{max} of 200-300 signalize, that the image contrast is high, the lesion is clearly separable from the background and consequently the detectability should be very high. Even after significant influences of reduced acquisition time that could lead to the believe of degraded image quality, the synergy of SNR and LBR still ensure clear visual assessment of the images.

5.4 Comparison of Phantom and Patient Results

This study analysed phantom as well as patient data, demonstrating dependence on acquisition duration for either cases. Contrarily to the controlled phantom study, in patients additional factors (anatomic structure, metabolic processes, respiratory motion, etc.) might interfere with the effect of reduced acquisition time in patient studies. In the phantom acquisition, the time activity curve is inherently constant, but the obvious big difference between the theoretical decay of ^{18}F and the observed reduction of count rate (Figure 4.13) in the patients, suggest biological decay which means draining off of activity from the cerebral region. Observed in more detail, tracer kinetics can deliver a significant message about the grading of a tumor (Pöpperl et al., 2006, 2007).

The total number of prompts in the phantom is by a factor of 4 higher than in the patient images on average, of which a factor of approximately 2 derives from the redoubled acquisition time.

The absolute background values of the longest acquisition in $^{18}\text{F} - \text{FET}$ patients and the phantom are of similar magnitude, but show opposing behaviour with shorter frame lengths. SUV_{BG} in $^{18}\text{F} - \text{FET}$ patients decreases by $3(2)\,\%$ when reducing acquisition time by a factor of 20.

As expected, background variability increased in all cases (phantom, $^{68}\text{Ga} - \text{DOTANOC}$, $^{18}\text{F} - \text{FET}$; OSEM and PSF) strongly with reduced acquisition time. This is apparently solely caused by the reduction of prompts per image, as Figure 4.5 demonstrated for the phantom. In the patient data we found similar dependences with small variances. OSEM reconstruction influences noise properties significantly less then PSF reconstruction, but still noise more than doubles in all cases when reducing frame length by a factor of 20. In the phantom and the $^{18}\text{F} - \text{FET}$ images, the absolute N_{BG} values are very similar (as the background activities are), but in $^{68}\text{Ga} - \text{DOTANOC}$ patients, N_{BG} and a_{BG} have to be taken with caution. The extremely low number of counts in uniform regions is easily influenced by the reconstruction algorithm, as described above. For low activity concentrations, noise alone can be misleading and should be avoided to solely describe the image properties. Resolution recovery without post-filtering (PSF) generally expresses approximately twice as high image noise as the

smoothed OSEM alternative.

While PSF improved image quality and quantity in long acquisitions of the phantom measurements, for short acquisitions the very nature of PSF and the lack of post-filtering deteriorated the image quality for visual assessment, as had been observed before (Kadrmas et al., 2012). The quantifications with PSF generally showed higher deviations (see Table 5.1) than OSEM. Additionally, PSF images were notably less stable against reduction of acquisition time.

Similar to the phantom results, we found increasing $LBR_{\max}$ in ^{18}F $-$ FET patients. Contrarily to the phantom, the background activity in the ^{18}F $-$ FET patients decreased and therefore, together with the increasing maximum activity, contributed to increasing $LBR_{\max}$. Taking into account the comparability of several parameters, as similar lesion size, background activity and of course same radioisotope, direct comparison between phantom and ^{18}F $-$ FET patient data is justified. For the deviations (reducing acquisition time by a factor of 20) of most measures (N_{BG} , $RC_{\max}$, $SNR_{\max}$ and $SUV_{\max}$) we indeed found quite similar results for OSEM and PSF. Average of all spheres gives comparable behaviour to the ^{18}F $-$ FET data for VOL_{41} as well.

For future studies, it is suggested to take into account further and more complex measures, especially SUV_{peak} , into account. SUV_{peak} is the highest average SUV that can be found in a $1\,\mathrm{cm}^3$-sized spherical ROI around the $SUV_{\max}$. Compared to $SUV_{\max}$, it has the disadvantage of reduced sensitivity to image characteristics (Lodge et al., 2012), but has proven as a very robust measure for short acquisition times, at least in specific studies (Sher et al., 2016). The combination of $SUV_{\max}$ and SUV_{peak} (Lasnon et al., 2013) was suggested as a new standard approach for PET/CT (Boellaard, 2013).

5.5 Comparison of Results to the Literature

In a study of ultra-low-count images, similar negative bias of 2-6 %, as found in the ^{18}F $-$ FET patients, was reported for low-active regions (cerebellum) (Jian et al., 2015). In contrast to this, background activity a_{BG} shows significant *increase* of $5.6(6)\,\%$ in our phantom measurements, which has been reported similarly before (Walker et al., 2011; Reilhac et al., 2008).

Literature suggests to avoid concentrations below $50\,\mathrm{Bq}\,\mathrm{ml}^{-1}$ because of the mentioned bias, or to apply for low count images to the more stable forward-back-projection (FBP) (Bélanger et al., 2004). Described improvements with applied resolution recovery (Walker et al., 2011) could not be validated.

That short image acquisition times resulting in noisy images not necessarily have to be a crucial problem for qualitative assessment and tumor detection, as found in a previous study (Halpern et al., 2004).

$SUV_{\max}$ in ^{68}Ga $-$ DOTANOC patients was demonstrated to have high prognostic value for neuroendocrine tumors (NET), supposed to improve disease characterization and management (Campana et al., 2010). In the same study, $SUV_{\max}$ showed no significant differences if compared by sex, syndrome, stage or classification, while observing high variations of $SUV_{\max}$ between patients. Elsewhere (Ambrosini et al., 2015), $SUV_{\max}$ of ^{68}Ga-DOTA-peptides (as ^{68}Ga $-$ DOTANOC) was found to be not directly comparable between patients, deteriorating the general and unlimited applicability. Our evaluation of $SUV_{\max}$ in ^{68}Ga $-$ DOTANOC patients fit well to the results of the previously mentioned studies, but also confirmed the mentioned implications. We found $SUV_{\max}$ to range over nearly two magnitudes (2.2-93) including outliers, and even after cleaning up the data still ranging between 5-30.

For pediatric FDG PET/CT studies similar evaluations led to the conclusion, that reductions of acquisition time of more than 40 % led to a significant degradation of accuracy (Alessio et al., 2011). Similarly for a PET/CT an evaluation showed that the reduction by 50 % from 3 min to 1.5 min per

bed position in whole-body FDG scans had just slight negative effects on image quality but didn't affect lesion detection rate significantly (Hausmann et al., 2012). For a PET/MR scanner Zeimpekis et al proposed a reduction of 37% of acquisition time (or injected activity) without degrading image quality (Zeimpekis et al., 2015). Our evaluations are confirmed by these findings and we even propose the possibility of higher reductions either in acquisition time or injected activity, depending on the optimizing of tracer used and reconstruction setting.

Previously, a study by Cal-González et al. was conducted to investigate the influence of acquisition time on quantification accuray in a PET/CT system (Siemens Biograph True Point True View PET/CT) (Cal-González et al., 2015b). A phantom study with a sphere-to-background ratio of 4.9 as well as an analysis of $^{18}\mathrm{F}-\mathrm{FET}$ patients was performed with alike materials and methodology, allowing direct comparison to the results of the study presented here. No significant differences between our results (PET/MR) and the mentioned study (PET/CT) were found for noise and background activity in the phantom study. Differences in noise were only visible in OSEM reconstructions and very short scan duration ($1\,\mathrm{min}$), where the PET/MR, due to its higher sensitivity, showed 25% lower noise than the PET/CT. Results for the smallest spheres were identical in both systems, affirming, that in small lesions partial volume effect predominantly influenced quantitative measures and no significant differences because of scanner-properties (sensitivity, peak NEC rate,...) would be visible. Generally, for the bigger spheres, image noise mainly influenced quantification accuracy, which suggested distinct outcomes for different scanners. Concretely, the sensitivity of this PET/CT ($8.1\,/(\mathrm{s\,MBq})$ (Jakoby et al., 2009)) is by 41% lower than our PET/MR's ($13.8\,/(\mathrm{s\,MBq})$). One would expect this to reduce deviations in acquisitions with PET/MR. With OSEM reconstruction, both RC_{50} and $RC_{\max}$ were similar in PET/CT and PET/MR acquisitions. With PSF reconstruction, the PET/MR showed *higher RC*-values than the PET/CT in the $20\,\mathrm{min}$ acquisitions, but differences of up to 20% in the $1\,\mathrm{min}$ images. This surprising result has to be verified by a repeated evaluation of the phantom data by assuring identical acquisition protocols. Analysis of the $^{18}\mathrm{F}-\mathrm{FET}$ patient data revealed smaller deviations with shorter acquisition times in PET/MR than in PET/CT. This is, as mentioned above, the behaviour expected from the higher sensitivity of the Biograph mMR. With OSEM reconstruction differences for $SUV_{\max}$ and SUV_{50} were found similar, the PET/MR showing significantly lower deviations than the PET/CT. With PSF reconstruction, the differences between the systems were notable but statistically not significant. Background activity (SUV_{BG}) in PET/MR and PET/CT patients showed diametrically opposite results. As mentioned, in PET/MR we found decreasing SUV_{BG} for shorter acquisition times, while in the PET/CT acquisitions SUV_{BG} increased by up to 12% with both reconstruction settings. The cause of this difference has not been fully understood yet and is subject to further investigations. Concluding, we found similar behaviour when reducing acquisition time in both systems, but differences in the performance of the scanners with shorter scan duration were identified. Those differences were not transferable from the phantom to the patient data. In both systems similarly, threshold-based measures (RC_{50}, SUV_{50}) were generally less influenced by shorter acquisition time than maximum activity measures ($RC_{\max}$, $SUV_{\max}$).

5.6   Implications of the Work

Study in controlled environment (phantom acquisition) was only done with one tracer, $^{18}\mathrm{F}$. For complete validation of the whole patient data ($^{18}\mathrm{F}-\mathrm{FET}$ *and* $^{68}\mathrm{Ga}-\mathrm{DOTANOC}$), a second phantom study with a $^{68}\mathrm{Ga}$-based tracer has to be performed as well. In the $10\,\mathrm{min}$ list mode acquisition no tracer dynamics are assumed. This has been affirmed to satisfying accuracy by visual comparison of the shortest frames, which are very similar to a dynamic acquisition. The quest for reducing overall time of combined PET acquisitions is more important for whole-body studies in PET/CT that cover several

bed positions. Acquisition time in PET/MR is still mainly limited by the duration of the MR sequence and therefore is not yet required reduction of PET scan time. For these cases, the presented results are similarly applicable, as changes in acquisition time are closely related to adaptations of administered activity. No pathological gold standard was provided, but instead the longest acquisition (20 min and 10 min in phantom and patient scans, respectively) was defined as the gold standard for this study. The presented evaluation was a *statistical* analysis of a pool of real patients. Individual patients, even those included in the study, might significantly deviate from the presented average, as data from patients with a variety of parameters (size, location and form of tumor, anamnesis, previous treatments) was pooled. The reconstruction algorithms are not adapted for best imaging results, but should represent two opposite approaches: OSEM with heavy post-filtering may result in overly smooth images and thereby reduce the detectability of very small lesions, while PSF with resolution recovery but without filtering "encourages" noise and might lead to a high rate of false-positives in clinical assessment. Further analysis of the data with additional classifications (e.g. patient weight, administered activity, tumor size, etc.) and combined factor analysis could reveal statistical differences between groups and consequently reveal further approaches to improve the quantification accuracy.

Chapter 6

Conclusions

In a general attempt to potentially reduce administered doses, we studied the influence of acquisition time, as a surrogate for injected dose, on quantitative accuracy of PET images. We found significant influence on image quality as well as on quantitative measures in phantom and patient studies. As a main contributor to degrading quantification accuracy, noise increases directly with reducing acquisition time, or accordingly the number of counts per image. Reconstruction settings mainly influence overall image appearance but even more distinctly quantitative measures. Post-filtering of images introduced stability for a wide range of scan durations. On the other hand, images with resolution modelling but without smoothing were influenced significantly stronger by reduction of acquisition time. While noise most significantly influences maximum activity measures in bigger lesions, in small lesions partial volume effect determines the accuracy of these measures. In this regard, Erlandsson et al. noted pointedly about partial volume correction (PVC):

> "PVC is an important aspect of quantitative analysis in emission tomography, which remains an area of active research. The clinical community should be encouraged to adopt PVC methods as part of standard processing procedures. Multimodality systems, combining PET or SPECT with CT or MRI, allow acquisition of co-registered functional and anatomical images. As these systems are becoming widely available, perhaps the time has come for PVC to be routinely used in clinical practice." (Erlandsson et al., 2012)

Effects of reducing acquisition time can not be generalized, but have to be separately evaluated for different tracers. Qualitative assessment might still be valid even for further reductions than measured here, even if quantification accuracy is no longer fulfilled. This was observed for radiopharmaceuticals as ^{68}Ga – DOTANOC due to the negligible uptake in non-tumor regions. Overall, reducing acquisition time by up to 50 % was found to not influence image quality nor quantitative measures. The potential reductions depend heavily on the applied settings, as choice of tracer, administered activity and reconstruction algorithm, and can even be raised by individually adapting these settings for each study.

Final conclusion

The increase of image noise, RC and SUV, and the decrease of SNR with shorter scan duration affect quantification accuracy adversely. However, measures from mean activities within a segmented threshold are less affected by reduction of acquisition duration than measures from maximum activity, and hence more convenient to evaluate studies at different levels of noise. By using mean segmented activities, potential reductions of acquisition time up to 50 % can be obtained without compromising image quality.

Outlook

The development of even more specified tracers will initiate new opportunities of improving patient well-being. In order to pursue the idea of minimizing patient exposure in PET imaging, research has to be extended to ultra-low-count acquisitions. At this point, partial volume effects will play an even more crucial role, therefore PVC has to be driven forward. Optimizing the settings for each PET-study to achieve the optimum of acquisition time, administered activity and image quality will be a future challenge.

Abbreviations

BG	background
CT	computed tomography
DOTANOC	a ^{68}Ga-based radiotracer
FET	an ^{18}F-based radiotracer
FOV	field of view
FWHM	full width at half maximum
IQ	image quality
IQR	interquartile range
it	iteration(s)
LBR	lesion-to-background ratio
MR	magnetic resonance (imaging)
MRI	magnetic resonance imaging
NEMA	National Electrical
NET	neuroendocrine tumor
OSEM	ordered subsets expectation maximization
PET	positron emission tomography
PET/CT	hybrid PET and CT system
PET/MR	hybrid PET and MR system
PSF	point spread function
RC	recovery coefficient
ROI	region of interest
SD	standard deviation
SNR	signal-to-noise ratio
subs	subsets
SUV	standardized uptake value
TOF	time of flight
VOI	volume of interest
VOL	(segmented) volume

List of Figures

List of Tables

Bibliography

G. Akamatsu, K. Ishikawa, K. Mitsumoto, T. Taniguchi, N. Ohya, S. Baba, K. Abe, and M. Sasaki. Improvement in PET/CT Image Quality with a Combination of Point-Spread Function and Time-of-Flight in Relation to Reconstruction Parameters. *Journal of Nuclear Medicine*, 53(11): 1716–1722, nov 2012. ISSN 0161-5505. doi: 10.2967/jnumed.112.103861. URL http://www.ncbi.nlm.nih.gov/pubmed/22952340http://jnm.snmjournals.org/cgi/doi/10.2967/jnumed.112.103861.

N. L. Albert, M. Weller, B. Suchorska, N. Galldiks, R. Soffietti, M. M. Kim, C. la Fougère, W. Pope, I. Law, J. Arbizu, M. C. Chamberlain, M. Vogelbaum, B. M. Ellingson, and J. C. Tonn. Response Assessment in Neuro-Oncology working group and European Association for Neuro-Oncology recommendations for the clinical use of PET imaging in gliomas. *Neuro-Oncology*, 18(9):1199–1208, sep 2016. ISSN 1522-8517. doi: 10.1093/neuonc/now058. URL http://neuro-oncology.oxfordjournals.org/lookup/doi/10.1093/neuonc/now058.

A. Alessio and P. Kinahan. PET image reconstruction. In R. Henkin, editor, *Nuclear medicine*. 2nd edition, 2006a. URL http://faculty.washington.edu/aalessio/papers/alessioPETRecon.pdf.

A. M. Alessio and P. E. Kinahan. Improved quantitation for PET/CT image reconstruction with system modeling and anatomical priors. *Medical Physics*, 33(11):4095, 2006b. ISSN 00942405. doi: 10.1118/1.2358198. URL http://scitation.aip.org/content/aapm/journal/medphys/33/11/10.1118/1.2358198.

A. M. Alessio, M. Sammer, G. S. Phillips, V. Manchanda, B. C. Mohr, and M. T. Parisi. Evaluation of Optimal Acquisition Duration or Injected Activity for Pediatric 18F-FDG PET/CT. *Journal of Nuclear Medicine*, 52(7):1028–1034, jul 2011. ISSN 0161-5505. doi: 10.2967/jnumed.110.086579. URL http://jnm.snmjournals.org/cgi/doi/10.2967/jnumed.110.086579.

V. Ambrosini, D. Campana, G. Polverari, C. Peterle, S. Diodato, C. Ricci, V. Allegri, R. Casadei, P. Tomassetti, and S. Fanti. Prognostic Value of 68Ga-DOTANOC PET/CT SUVmax in Patients with Neuroendocrine Tumors of the Pancreas. *Journal of nuclear medicine : official publication, Society of Nuclear Medicine*, 56(12):1843–8, 2015. ISSN 1535-5667. doi: 10.2967/jnumed.115.162719. URL http://www.ncbi.nlm.nih.gov/pubmed/26405169.

B. Bai, J. Bading, and P. S. Conti. Tumor Quantification in Clinical Positron Emission Tomography. *Theranostics*, 3(10):787–801, 2013a. ISSN 1838-7640. doi: 10.7150/thno.5629. URL http://www.thno.org/v03p0787.htm.

B. Bai, Q. Li, and R. M. Leahy. Magnetic Resonance-Guided Positron Emission Tomography Image Reconstruction. *Seminars in Nuclear Medicine*, 43(1):30–44, jan 2013b. ISSN 00012998. doi: 10.1053/j.semnuclmed.2012.08.006. URL http://linkinghub.elsevier.com/retrieve/pii/S0001299812000827.

D. L. Bailey. Transmission scanning in emission tomography. *European Journal of Nuclear Medicine*, 25 (7):774–787, 1998. ISSN 03406997. doi: 10.1007/s002590050282.

D. L. Bailey, D. W. Townsend, P. E. Valk, and M. N. Maisey, editors. *Positron Emission Tomography*. Springer-Verlag, London, 2005. ISBN 1-85233-798-2. doi: 10.1007/b136169. URL `http://link.springer.com/10.1007/b136169`.

M.-J. Bélanger, J. Mann, and R. V. Parsey. OS-EM and FBP reconstructions at low count rates: effect on 3D PET studies of [11C] WAY-100635. *NeuroImage*, 21(1):244–250, jan 2004. ISSN 10538119. doi: 10.1016/j.neuroimage.2003.08.035. URL `http://linkinghub.elsevier.com/retrieve/pii/S1053811903005433`.

N. a. Benatar, B. F. Cronin, and M. J. O'Doherty. Radiation dose rates from patients undergoing PET: implications for technologists and waiting areas. *European journal of nuclear medicine*, 27(5):583–589, 2000. ISSN 0340-6997. doi: 10.1007/s002590050546.

F. M. Bengel, T. Higuchi, M. S. Javadi, and R. Lautamäki. Cardiac Positron Emission Tomography, 2009. ISSN 07351097.

T. Beyer, D. W. Townsend, T. Brun, P. E. Kinahan, M. Charron, R. Roddy, J. Jerin, J. Young, L. Byars, and R. Nutt. A combined PET/CT scanner for clinical oncology. *J Nucl Med*, 41(8):1369–1379, 2000. ISSN 0161-5505. URL `http://www.ncbi.nlm.nih.gov/pubmed/10945530`.

T. Beyer, G. Antoch, S. Müller, T. Egelhof, L. S. Freudenberg, J. Debatin, and A. Bockisch. Acquisition protocol considerations for combined PET/CT imaging. *Journal of nuclear medicine : official publication, Society of Nuclear Medicine*, 45 Suppl 1(1 suppl):25S–35S, jan 2004. ISSN 0161-5505. URL `http://jnm.snmjournals.org/content/45/1{_}suppl/25S.abstracthttp://www.ncbi.nlm.nih.gov/pubmed/14736833`.

T. Beyer, M. Weigert, H. H. Quick, U. Pietrzyk, F. Vogt, C. Palm, G. Antoch, S. P. Müller, and A. Bockisch. MR-based attenuation correction for torso-PET/MR imaging: pitfalls in mapping MR to CT data. *European Journal of Nuclear Medicine and Molecular Imaging*, 35(6):1142–1146, jun 2008. ISSN 1619-7070. doi: 10.1007/s00259-008-0734-0. URL `http://link.springer.com/10.1007/s00259-008-0734-0`.

T. Beyer, L. S. Freudenberg, J. Czernin, and D. W. Townsend. The future of hybrid imagingpart 3: PET/MR, small-animal imaging and beyond. *Insights into Imaging*, 2(3):235–246, jun 2011a. ISSN 1869-4101. doi: 10.1007/s13244-011-0085-4. URL `http://link.springer.com/10.1007/s13244-011-0085-4`.

T. Beyer, D. W. Townsend, J. Czernin, and L. S. Freudenberg. The future of hybrid imaging-part 2: PET/CT. *Insights into imaging*, 2(3):225–34, 2011b. ISSN 1869-4101. doi: 10.1007/s13244-011-0069-4. URL `http://www.pubmedcentral.nih.gov/articlerender.fcgi?artid=3288992{&}tool=pmcentrez{&}rendertype=abstract`.

R. Boellaard. Optimisation and harmonisation: two sides of the same coin? *European Journal of Nuclear Medicine and Molecular Imaging*, 40(7):982–984, jul 2013. ISSN 1619-7070. doi: 10.1007/s00259-013-2440-9. URL `http://link.springer.com/10.1007/s00259-013-2440-9`.

R. Boellaard and H. H. Quick. Current Image Acquisition Options in PET/MR. *Seminars in Nuclear Medicine*, 45(3):192–200, may 2015. ISSN 00012998. doi: 10.1053/j.semnuclmed.2014.12.001. URL `http://linkinghub.elsevier.com/retrieve/pii/S0001299814001445`.

R. Boellaard, N. C. Krak, O. S. Hoekstra, and A. A. Lammertsma. Effects of noise, image resolution, and ROI definition on the accuracy of standard uptake values: a simulation study. *Journal of nuclear medicine : official publication, Society of Nuclear Medicine*, 45(9):1519–27, sep 2004. ISSN 0161-5505. URL `http://jnm.snmjournals.org/content/45/9/1519.abstractN2-http://www.ncbi.nlm.nih.gov/pubmed/15347719`.

R. Boellaard, R. Delgado-Bolton, W. J. G. Oyen, F. Giammarile, K. Tatsch, W. Eschner, F. J. Verzijlbergen, S. F. Barrington, L. C. Pike, W. A. Weber, S. Stroobants, D. Delbeke, K. J. Donohoe, S. Holbrook, M. M. Graham, G. Testanera, O. S. Hoekstra, J. Zijlstra, E. Visser, C. J. Hoekstra, J. Pruim, A. Willemsen, B. Arends, J. Kotzerke, A. Bockisch, T. Beyer, A. Chiti, and B. J. Krause. FDG PET/CT: EANM procedure guidelines for tumour imaging: version 2.0. *European Journal of Nuclear Medicine and Molecular Imaging*, 42(2):328–354, feb 2015. ISSN 1619-7070. doi: 10.1007/s00259-014-2961-x. URL `http://link.springer.com/10.1007/s00259-014-2961-x`.

Brilliant.org. brilliant.org. URL `https://brilliant.org/problems/foolish-proton-in-cyclotron/`.

G. Brix, U. Lechel, G. Glatting, S. I. Ziegler, W. Münzing, S. P. Müller, and T. Beyer. Radiation exposure of patients undergoing whole-body dual-modality 18F-FDG PET/CT examinations. *Journal of nuclear medicine : official publication, Society of Nuclear Medicine*, 46(4):608–13, 2005. ISSN 0161-5505. doi: 46/4/608[pii]. URL `http://www.ncbi.nlm.nih.gov/pubmed/15809483`.

J. Cal González. Positron range and prompt gamma modeling in PET imaging, apr 2014. URL `http://www.tdx.cat/handle/10803/356552`.

J. Cal-Gonzalez, J. L. Herraiz, S. Espana, M. Desco, J. J. Vaquero, and J. M. Udias. Positron range effects in high resolution 3D PET imaging. In *2009 IEEE Nuclear Science Symposium Conference Record (NSS/MIC)*, pages 2788–2791. IEEE, oct 2009. ISBN 978-1-4244-3961-4. doi: 10.1109/NSSMIC.2009. 5401950. URL `http://ieeexplore.ieee.org/lpdocs/epic03/wrapper.htm?arnumber=5401950`.

J. Cal-González, E. Lage, E. Herranz, E. Vicente, J. M. Udias, S. C. Moore, M.-A. Park, S. R. Dave, V. Parot, and J. L. Herraiz. Simulation of triple coincidences in PET. *Physics in medicine and biology*, 60(1):117–36, jan 2015a. ISSN 1361-6560. doi: 10.1088/0031-9155/60/1/117. URL `http://ieeexplore.ieee.org/lpdocs/epic03/wrapper.htm?arnumber=6829155http://www.ncbi.nlm.nih.gov/pubmed/25479147`.

J. Cal-González, I. Rausch, and T. Beyer. PET quantification as a function of the acquisition time in PET/CT. Vienna, 2015b.

D. Campana, V. Ambrosini, R. Pezzilli, S. Fanti, A. M. M. Labate, D. Santini, C. Ceccarelli, F. Nori, R. Franchi, R. Corinaldesi, and P. Tomassetti. Standardized Uptake Values of 68Ga-DOTANOC PET: A Promising Prognostic Tool in Neuroendocrine Tumors. *Journal of Nuclear Medicine*, 51(3):353–359, mar 2010. ISSN 0161-5505. doi: 10.2967/jnumed.109.066662. URL `http://jnm.snmjournals.org/cgi/doi/10.2967/jnumed.109.066662`.

T. Carlier, L. Ferrer, H. Necib, C. Bodet-Milin, C. Rousseau, and F. Kraeber-Bodéré. Clinical NECR in 18F-FDG PET scans: Optimization of patient specific activity and variable acquisition time. Relationship with SNR. In *IEEE Nuclear Science Symposium Conference Record*, 2013. ISBN 9781479905348. doi: 10.1109/NSSMIC.2013.6829382.

S. C. Chawla, N. Federman, D. Zhang, K. Nagata, S. Nuthakki, M. McNitt-Gray, and M. I. Boechat. Estimated cumulative radiation dose from PET/CT in children with malignancies: a 5-year retrospective review. *Pediatric Radiology*, 40(5):681–686, may 2010. ISSN 0301-0449. doi: 10.1007/s00247-009-1434-z. URL `http://link.springer.com/10.1007/s00247-009-1434-z`.

M.-K. Chen, D. H. Menard, and D. W. Cheng. Determining the Minimal Required Radioactivity of 18F-FDG for Reliable Semiquantification in PET/CT Imaging: A Phantom Study. *Journal of nuclear medicine technology*, 44(1):26–30, 2016. ISSN 1535-5675. doi: 10.2967/jnmt.115.165258. URL `http://www.ncbi.nlm.nih.gov/pubmed/26769598`.

D. W. Cheng, D. Ersahin, L. H. Staib, D. Della Latta, A. Giorgetti, and F. D'Errico. Using SUV as a Guide to 18F-FDG Dose Reduction. *Journal of Nuclear Medicine*, 55(12):1998–2002, dec 2014. ISSN 0161-5505. doi: 10.2967/jnumed.114.140129. URL `http://jnm.snmjournals.org/cgi/doi/10.2967/jnumed.114.140129`.

J. F. Cornelius, G. Stoffels, C. Filß, N. Galldiks, P. Slotty, M. Kamp, M. el Khatib, D. Hänggi, M. Sabel, J. Felsberg, H. J. Steiger, H. H. Coenen, N. J. Shah, and K. J. Langen. Uptake and tracer kinetics of O-(2-¹⁸F-fluoroethyl)-l-tyrosine in meningiomas: preliminary results. *European Journal of Nuclear Medicine and Molecular Imaging*, 42(3):459–467, 2014. ISSN 16197089. doi: 10.1007/s00259-014-2934-0.

W. G. Cross, H. Ing, and N. Freedman. A short atlas of beta-ray spectra. *Physics in Medicine and Biology*, 28(11):1251, 1983. ISSN 00319155. URL `http://stacks.iop.org/0031-9155/28/i=11/a=005`.

G. Delso, S. Furst, B. Jakoby, R. Ladebeck, C. Ganter, S. G. Nekolla, M. Schwaiger, and S. I. Ziegler. Performance Measurements of the Siemens mMR Integrated Whole-Body PET/MR Scanner. *Journal of Nuclear Medicine*, 52(12):1914–1922, dec 2011. ISSN 0161-5505. doi: 10.2967/jnumed.111.092726. URL `http://jnm.snmjournals.org/content/52/12/1914$\delimiter"026E30F$nhttp://jnm.snmjournals.org/content/52/12/1914.full.pdf$\delimiter"026E30F$nhttp://www.ncbi.nlm.nih.gov/pubmed/22080447http://jnm.snmjournals.org/cgi/doi/10.2967/jnumed.111.092726`.

A. P. Dempster, N. M. Laird, and D. B. Rubin. Maximum Likelihood from Incomplete Data via the EM Algorithm. *Journal of the Royal Statistical Society. Series B*, 39(1):1–38, 1977. ISSN 00359246. doi: 10.2307/2984875. URL `http://www.jstor.org/stable/2984875`.

V. Dunet, C. Rossier, A. Buck, R. Stupp, and J. O. Prior. Performance of 18F-Fluoro-Ethyl-Tyrosine (18F-FET) PET for the Differential Diagnosis of Primary Brain Tumor: A Systematic Review and Metaanalysis. *Journal of Nuclear Medicine*, 53(2):207–214, feb 2012. ISSN 0161-5505. doi: 10.2967/jnumed.111.096859. URL `http://www.ncbi.nlm.nih.gov/pubmed/22302961http://jnm.snmjournals.org/cgi/doi/10.2967/jnumed.111.096859`.

A. J. Einstein. Effects of Radiation Exposure From Cardiac Imaging. *Journal of the American College of Cardiology*, 59(6):553–565, feb 2012. ISSN 07351097. doi: 10.1016/j.jacc.2011.08.079. URL `http://linkinghub.elsevier.com/retrieve/pii/S0735109711049217`.

El-se.com. NEMA IEC PET Body, 2016. URL `http://www.el-se.com/en/prodotti/nuclear-medicine/quality-control/phantoms/nema-iec-pet-body/`.

K. Erlandsson, I. Buvat, P. H. Pretorius, B. a. Thomas, and B. F. Hutton. A review of partial volume correction techniques for emission tomography and their applications in neurology, cardiology and oncology. *Physics in Medicine and Biology*, 57(21):R119–R159, nov 2012. ISSN 0031-9155. doi: 10.1088/0031-9155/57/21/R119. URL `http://stacks.iop.org/0031-9155/57/i=21/a=R119?key=crossref.4613f99a63010e4337b3a316357415db`.

F. H. Fahey. Data acquisition in PET imaging. *Journal of nuclear medicine technology*, 30(2):39–49, jun 2002. ISSN 0091-4916. URL `http://www.ncbi.nlm.nih.gov/pubmed/12055275`.

B. J. Feir-Walsh and L. E. Toothaker. An Empirical Comparison of the Anova F-Test, Normal Scores Test and Kruskal-Wallis Test Under Violation of Assumptions. *Educational and Psychological Measurement*, 34(4):789–799, 1974. ISSN 0013-1644. doi: 10.1177/001316447403400406. URL `http://epm.sagepub.com/cgi/content/abstract/34/4/789`.

A. Firouzian, M. D. Kelly, and J. M. Declerck. Insight on automated lesion delineation methods for PET data. *EJNMMI Research*, 4(1):69, dec 2014. ISSN 2191-219X. doi: 10.1186/s13550-014-0069-8. URL `http://www.ejnmmires.com/content/4/1/69`.

E. C. Ford, P. E. Kinahan, L. Hanlon, A. Alessio, J. Rajendran, D. L. Schwartz, and M. Phillips. Tumor delineation using PET in head and neck cancers: threshold contouring and lesion volumes. *Medical physics*, 33(11):4280–4288, 2006. ISSN 00942405. doi: 10.1118/1.2361076.

A. M. Grant, T. W. Deller, M. M. Khalighi, S. H. Maramraju, G. Delso, and C. S. Levin. NEMA NU 2-2012 performance studies for the SiPM-based ToF-PET component of the GE SIGNA PET/MR system. *Medical Physics*, 43(5):2334–2343, may 2016. ISSN 0094-2405. doi: 10.1118/1.4945416. URL http://scitation.aip.org/content/aapm/journal/medphys/43/5/10.1118/1.4945416.

M. Guillaume, A. Luxen, B. Nebeling, M. Argentini, J. C. Clark, and V. W. Pike. Recommendations for fluorine-18 production. *International Journal of Radiation Applications and Instrumentation. Part*, 42 (8):749–762, jan 1991. ISSN 08832889. doi: 10.1016/0883-2889(91)90179-5. URL http://linkinghub. elsevier.com/retrieve/pii/0883288991901795.

B. S. Halpern, M. Dahlbom, A. Quon, C. Schiepers, C. Waldherr, D. H. Silverman, O. Ratib, and J. Czernin. Impact of patient weight and emission scan duration on PET/CT image quality and lesion detectability. *Journal of nuclear medicine : official publication, Society of Nuclear Medicine*, 45(5): 797–801, may 2004. ISSN 0161-5505. URL http://www.ncbi.nlm.nih.gov/pubmed/15136629.

D. Hausmann, D. J. Dinter, M. Sadick, J. Brade, S. O. Schoenberg, and K. Busing. The Impact of Acquisition Time on Image Quality in Whole-Body 18F-FDG PET/CT for Cancer Staging. *Journal of Nuclear Medicine Technology*, 40(4):255–258, dec 2012. ISSN 0091-4916. doi: 10.2967/jnmt.112.103291. URL http://tech.snmjournals.org/cgi/doi/10.2967/jnmt.112.103291.

A. Hirtl. Functional imaging technology and devices Physical principles Outline of Part I. 2016.

F. Hofheinz, J. Langner, J. Petr, B. Beuthien-Baumann, J. Steinbach, J. Kotzerke, and J. van den Hoff. An automatic method for accurate volume delineation of heterogeneous tumors in PET. *Medical physics*, 40(8):082503, 2013. ISSN 0094-2405. doi: 10.1118/1.4812892. URL http://www.ncbi.nlm. nih.gov/pubmed/23927348.

B. Huang, M. W.-M. Law, and P.-L. Khong. Whole-Body PET/CT Scanning: Estimation of Radiation Dose and Cancer Risk. *Radiology*, 251(1):166–174, apr 2009. ISSN 0033-8419. doi: 10.1148/radiol. 2511081300. URL http://pubs.rsna.org/doi/10.1148/radiol.2511081300.

B. Huang, J. Li, M. W.-M. Law, J. Zhang, Y. Shen, and P. L. Khong. Radiation dose and cancer risk in retrospectively and prospectively ECG-gated coronary angiography using 64-slice multidetector CT. *The British Journal of Radiology*, 83(986):152–158, feb 2010. ISSN 0007-1285. doi: 10.1259/bjr/ 29879495. URL http://www.birpublications.org/doi/10.1259/bjr/29879495.

H. Hudson and R. Larkin. Accelerated image reconstruction using ordered subsets of projection data. *IEEE Transactions on Medical Imaging*, 13(4):601–609, 1994. ISSN 02780062. doi: 10.1109/42.363108. URL http://ieeexplore.ieee.org/lpdocs/epic03/wrapper.htm?arnumber=363108.

K. Inoue, H. Kurosawa, T. Tanaka, M. Fukushi, N. Moriyama, and H. Fujii. Optimization of injection dose based on noise-equivalent count rate with use of an anthropomorphic pelvis phantom in three-dimensional 18F-FDG PET/CT. *Radiological Physics and Technology*, 5(2):115–122, 2012. ISSN 18650333. doi: 10.1007/s12194-011-0144-z.

International Electrotechnical Comission. IEC 61675-1:2013, Radionuclide imaging devices - Characteristics and test conditions - Part 1: Positron emission tomographs. 2013.

H. Jadvar and P. M. Colletti. Competitive advantage of PET/MRI, 2014. ISSN 0720048X.

B. W. Jakoby, Y. Bercier, C. C. Watson, B. Bendriem, and D. W. Townsend. Performance characteristics of a new LSO PET/CT scanner with extended axial field-of-view and PSF reconstruction. *IEEE Transactions on Nuclear Science*, 56(3):633–639, 2009. ISSN 00189499. doi: 10.1109/TNS.2009.2015764.

Y. Jian, B. Planeta, and R. E. Carson. Evaluation of bias and variance in low-count OSEM list mode reconstruction. *Physics in Medicine and Biology*, 60(1):15–29, jan 2015. ISSN 0031-9155. doi: 10.1088/0031-9155/60/1/15. URL `http://www.ncbi.nlm.nih.gov/pubmed/25479254$\delimiter"026E30F$nhttp://dx.doi.org/10.1088/0031-9155/60/1/15http://stacks.iop.org/0031-9155/60/i=1/a=15?key=crossref.057cbf488d1ce1359786b99350a1e748`.

D. J. Kadrmas, M. B. Oktay, M. E. Casey, and J. J. Hamill. Effect of Scan Time on Oncologic Lesion Detection in Whole-Body PET. *IEEE Transactions on Nuclear Science*, 59(5):1940–1947, oct 2012. ISSN 0018-9499. doi: 10.1109/TNS.2012.2197414. URL `http://ieeexplore.ieee.org/lpdocs/epic03/wrapper.htm?arnumber=6213167`.

O. Kagna, N. Pirmisashvili, S. Tshori, N. Freedman, O. Israel, and Y. Krausz. Neuroendocrine Tumor Imaging With 68 Ga-DOTA-NOC: Physiologic and Benign Variants. *American Journal of Roentgenology*, 203(6):1317–1323, dec 2014. ISSN 0361-803X. doi: 10.2214/AJR.14.12588. URL `http://www.ajronline.org/doi/abs/10.2214/AJR.14.12588`.

A. C. Kak and M. Slaney. *Principles of Computerized Tomographic Imaging*. Society for Industrial and Applied Mathematics, jan 2001. ISBN 978-0-89871-494-4. doi: 10.1137/1.9780898719277. URL `http://epubs.siam.org/doi/book/10.1137/1.9780898719277`.

H. J. Keselman, C. J. Huberty, L. M. Lix, S. Olejnik, R. a. Cribbie, B. Donahue, R. K. Kowalchuk, L. L. Lowman, M. D. Petoskey, J. C. Keselman, and J. R. Levin. Statistical Practices of Educational Researchers: An Analysis of their ANOVA, MANOVA, and ANCOVA Analyses. *Review of Educational Research*, 68(3):350–386, 1998. ISSN 0034-6543. doi: 10.3102/00346543068003350.

P. E. Kinahan and J. W. Fletcher. Positron Emission Tomography-Computed Tomography Standardized Uptake Values in Clinical Practice and Assessing Response to Therapy. *Seminars in Ultrasound, CT and MRI*, 31(6):496–505, dec 2010. ISSN 08872171. doi: 10.1053/j.sult.2010.10.001. URL `http://linkinghub.elsevier.com/retrieve/pii/S0887217110000880`.

P. E. Kinahan, D. W. Townsend, T. Beyer, and D. Sashin. Attenuation correction for a combined 3D PET/CT scanner. *Medical Physics*, 25(10):2046, 1998. ISSN 00942405. doi: 10.1118/1.598392. URL `http://scitation.aip.org/content/aapm/journal/medphys/25/10/10.1118/1.598392`.

C. Klenk, R. Gawande, L. Uslu, A. Khurana, D. Qiu, A. Quon, J. Donig, J. Rosenberg, S. Luna-Fineman, M. Moseley, and H. E. Daldrup-Link. Ionising radiation-free whole-body MRI versus 18F-fluorodeoxyglucose PET/CT scans for children and young adults with cancer: a prospective, non-randomised, single-centre study. *The Lancet Oncology*, 15(3):275–285, mar 2014. ISSN 14702045. doi: 10.1016/S1470-2045(14)70021-X. URL `http://linkinghub.elsevier.com/retrieve/pii/S147020451470021X`.

F. F. R. Knapp and S. Mirzadeh. The continuing important role of radionuclide generator systems for nuclear medicine. *European Journal of Nuclear Medicine*, 21(10):1151–1165, oct 1994. ISSN 03406997. doi: 10.1007/BF00181073. URL `http://link.springer.com/10.1007/BF00181073`.

G. F. Knoll. *Radiation Detection and Measurement*. 2010. ISBN 9780470131480.

C. N. Ladefoged, A. E. Hansen, S. H. Keller, S. Holm, I. Law, T. Beyer, L. Højgaard, A. Kjær, and F. L. Andersen. Impact of incorrect tissue classification in Dixon-based MR-AC: fat-water tissue

inversion. *EJNMMI Physics*, 1(1):101, 2014. ISSN 2197-7364. doi: 10.1186/s40658-014-0101-0. URL `http://www.ejnmmiphys.com/content/1/1/101`.

K. Lange and R. Carson. EM reconstruction algorithms for emission and transmission tomography. *Journal of computer assisted tomography*, 8(2):306–16, apr 1984. ISSN 0363-8715. URL `http://www.ncbi.nlm.nih.gov/pubmed/6608535`.

C. Lartizien, C. Comtat, P. E. Kinahan, N. Ferreira, B. Bendriem, and R. Trébossen. Optimization of injected dose based on noise equivalent count rates for 2- and 3-dimensional whole-body PET. *Journal of nuclear medicine : official publication, Society of Nuclear Medicine*, 43(9):1268–78, 2002. ISSN 0161-5505. URL `http://www.ncbi.nlm.nih.gov/pubmed/12215569`.

M.-C. Lasne, C. Perrio, J. Rouden, L. Barré, D. Roeda, F. Dolle, and C. Crouzel. Chemistry of b + -Emitting Compounds Based on Fluorine-18. In *Topics in Current Chemistry*, volume 222, pages 203–258. 2002. ISBN 978-3-540-43451-1. doi: 10.1007/3-540-46009-8_7. URL `http://dx.doi.org/10.1007/3-540-46009-8{_}7http://link.springer.com/10.1007/3-540-46009-8{_}7`.

C. Lasnon, C. Desmonts, E. Quak, R. Gervais, P. Do, C. Dubos-Arvis, and N. Aide. Harmonizing SUVs in multicentre trials when using different generation PET systems: Prospective validation in non-small cell lung cancer patients. *European Journal of Nuclear Medicine and Molecular Imaging*, 40(7):985–996, 2013. ISSN 16197070. doi: 10.1007/s00259-013-2391-1.

R. M. Leahy and J. Qi. No Title. *Statistics and Computing*, 10(2):147–165, 2000. ISSN 09603174. doi: 10.1023/A:1008946426658. URL `http://link.springer.com/article/10.1023/A:1008946426658$\delimiter"026E30F$nhttp://link.springer.com/content/pdf/10.1023/A:1008946426658http://link.springer.com/10.1023/A:1008946426658`.

R. Lecomte. Novel detector technology for clinical PET. *European Journal of Nuclear Medicine and Molecular Imaging*, 36(SUPPL. 1):69–85, 2009. ISSN 16197070. doi: 10.1007/s00259-008-1054-0.

C. S. Levin and E. J. Hoffman. Calculation of positron range and its effect on the fundamental limit of positron emission tomography system spatial resolution. *Physics in medicine and biology*, 44(3): 781–799, 1999. ISSN 0031-9155. doi: 10.1088/0031-9155/45/2/501.

T. K. Lewellen. Recent developments in PET detector technology. *Physics in medicine and biology*, 53 (17):R287–317, sep 2008. ISSN 0031-9155. doi: 10.1088/0031-9155/53/17/R01. URL `http://stacks.iop.org/0031-9155/53/i=17/a=R01?key=crossref.26ad9dcc43770f6e6011dae8be7e2380http://www.ncbi.nlm.nih.gov/pubmed/18695301http://www.pubmedcentral.nih.gov/articlerender.fcgi?artid=PMC2891023`.

M. A. Lodge, M. A. Chaudhry, and R. L. Wahl. Noise considerations for PET quantification using maximum and peak standardized uptake value. *Journal of nuclear medicine : official publication, Society of Nuclear Medicine*, 53(7):1041–7, 2012. ISSN 1535-5667. doi: 10.2967/jnumed.111.101733. URL `http://www.pubmedcentral.nih.gov/articlerender.fcgi?artid=3417317{&}tool=pmcentrez{&}rendertype=abstract`.

M. Magdics, B. Tóth, B. Kovács, and L. Szirmay-Kalos. Total Variation Regularization in PET Reconstruction. In *KÉPAF' 2011 - 8th Conference of the Hungarian Association for Image Processing and Pattern Recognition (January 2011)*, pages 40–53, 2011. URL `http://www.cs.cornell.edu/{~}bkovacs/resources/99135.pdf`.

J. D. Mathews, A. V. Forsythe, Z. Brady, M. W. Butler, S. K. Goergen, G. B. Byrnes, G. G. Giles, A. B. Wallace, P. R. Anderson, T. A. Guiver, P. McGale, T. M. Cain, J. G. Dowty, A. C. Bickerstaffe, and S. C. Darby. Cancer risk in 680,000 people

exposed to computed tomography scans in childhood or adolescence: data linkage study of 11 million Australians. *BMJ*, 346:f2360, 2013. ISSN 1756-1833. doi: 10.1136/bmj.f2360. URL `http://www.ncbi.nlm.nih.gov/pubmed/23694687$\delimiter"026E30F$nhttp://www.ncbi.nlm.nih.gov/pmc/articles/PMC3660619/pdf/bmj.f2360.pdf`.

R. McGill, J. W. Tukey, and W. a. Larsen. Variations of Box Plots. *The American Statistician*, 32(1): 12, feb 1978. ISSN 00031305. doi: 10.2307/2683468. URL `http://www.jstor.org/stable/2683468?origin=crossref`.

C. C. Meltzer, P. E. Kinahan, P. J. Greer, T. E. Nichols, C. Comtat, M. N. Cantwell, M. P. Lin, and J. C. Price. Comparative evaluation of MR-based partial-volume correction schemes for PET. *Journal of nuclear medicine : official publication, Society of Nuclear Medicine*, 40(12):2053–65, 1999. ISSN 0161-5505. URL `http://www.ncbi.nlm.nih.gov/pubmed/10616886`.

F. Molina-Duran, D. Dinter, F. Schoenahl, S. O. Schoenberg, and G. Glatting. Dependence of image quality on acquisition time for the PET/CT Biograph mCT. *Zeitschrift für Medizinische Physik*, 24(1):73–79, mar 2014. ISSN 09393889. doi: 10.1016/j.zemedi.2013.03.002. URL `http://dx.doi.org/10.1016/j.zemedi.2013.03.002http://linkinghub.elsevier.com/retrieve/pii/S0939388913000329`.

W. W. Moses. Time of Flight in PET Revisited. *IEEE Transactions on Nuclear Science*, 50(5 II): 1325–1330, 2003. ISSN 00189499. doi: 10.1109/TNS.2003.817319.

W. W. Moses. Fundamental limits of spatial resolution in PET. *Nuclear Instruments and Methods in Physics Research Section A: Accelerators, Spectrometers, Detectors and Associated Equipment*, 648 (SUPPL. 1):S236–S240, aug 2011. ISSN 01689002. doi: 10.1016/j.nima.2010.11.092. URL `http://linkinghub.elsevier.com/retrieve/pii/S0168900210026276`.

G. Muehllehner and J. S. Karp. Positron emission tomography. *Physics in Medicine and Biology*, 51(13): R117–R137, jul 2006. ISSN 0031-9155. doi: 10.1088/0031-9155/51/13/R08. URL `http://stacks.iop.org/0031-9155/51/i=13/a=R08?key=crossref.def2bf3786bdd2a2661ca56a5a6d1399`.

National Electrical Manufacturers Association. NEMA NU 2-2012 Performance Measurements of Positron Emission Tomographs. Technical report, Rosslyn, 2013.

NEMA. NU 2-2001: Performance Measurements of Positron Emission Tomographs (PETs). *NEMA Standards Publication*, NU 2-2001:47, 2001.

N. Q. Nguyen, C. K. Abbey, and M. F. Insana. Detectability index describes the information conveyed by sonographic images. In *2011 IEEE International Ultrasonics Symposium*, pages 680–683. IEEE, oct 2011. ISBN 978-1-4577-1252-4. doi: 10.1109/ULTSYM.2011.0165. URL `http://ieeexplore.ieee.org/lpdocs/epic03/wrapper.htm?arnumber=6293235`.

R. A. J. Nievelstein, H. M. E. Q. Van Ufford, T. C. Kwee, M. B. Bierings, I. Ludwig, F. J. A. Beek, J. M. H. De Klerk, W. P. T. M. Mali, P. W. De Bruin, and J. Geleijns. Radiation exposure and mortality risk from CT and PET imaging of patients with malignant lymphoma. *European Radiology*, 22(9):1946–1954, 2012. ISSN 09387994. doi: 10.1007/s00330-012-2447-9.

R. Nutt. The History of Positron Emission Tomography. *Molecular Imaging & Biology*, 4(1):11–26, feb 2002. ISSN 15361632. doi: 10.1016/S1095-0397(00)00051-0. URL `http://linkinghub.elsevier.com/retrieve/pii/S1095039700000510`.

M. Oehmigen, S. Ziegler, B. W. Jakoby, J.-C. Georgi, D. H. Paulus, and H. H. Quick. Radiotracer Dose Reduction in Integrated PET/MR: Implications from National Electrical Manufacturers Association Phantom Studies. *Journal of nuclear medicine : official publication, Society of Nuclear Medicine*, 55

(8):1361–1367, 2014. ISSN 1535-5667. doi: 10.2967/jnumed.114.139147. URL `http://www.ncbi.nlm.nih.gov/pubmed/25006216`.

Origin. OriginLab.

V. Y. Panin, F. Kehren, C. Michel, and M. Casey. Fully 3-D PET reconstruction with system matrix derived from point source measurements. *IEEE Transactions on Medical Imaging*, 25(7):907–921, 2006. ISSN 02780062. doi: 10.1109/TMI.2006.876171.

M. S. Pearce, J. A. Salotti, M. P. Little, K. McHugh, C. Lee, K. P. Kim, N. L. Howe, C. M. Ronckers, P. Rajaraman, A. W. Craft, L. Parker, and A. B. De González. Radiation exposure from CT scans in childhood and subsequent risk of leukaemia and brain tumours: A retrospective cohort study. *The Lancet*, 380(9840):499–505, 2012. ISSN 01406736. doi: 10.1016/S0140-6736(12)60815-0.

M. E. Phelps, E. J. Hoffman, N. A. Mullani, and M. M. Ter-Pogossian. Application of annihilation coincidence detection to transaxial reconstruction tomography. *Journal of nuclear medicine : official publication, Society of Nuclear Medicine*, 16(3):210–224, 1975. ISSN 0161-5505.

G. Pöpperl, F. W. Kreth, J. Herms, W. Koch, J. H. Mehrkens, F. J. Gildehaus, H. a. Kretzschmar, J. C. Tonn, and K. Tatsch. Analysis of 18F-FET PET for grading of recurrent gliomas: is evaluation of uptake kinetics superior to standard methods? *Journal of nuclear medicine : official publication, Society of Nuclear Medicine*, 47(3):393–403, mar 2006. ISSN 0161-5505. doi: 47/3/393[pii]. URL `http://www.ncbi.nlm.nih.gov/pubmed/16513607`.

G. Pöpperl, F. W. Kreth, J. H. Mehrkens, J. Herms, K. Seelos, W. Koch, F. J. Gildehaus, H. A. Kretzschmar, J. C. Tonn, and K. Tatsch. FET PET for the evaluation of untreated gliomas: Correlation of FET uptake and uptake kinetics with tumour grading. *European Journal of Nuclear Medicine and Molecular Imaging*, 34(12):1933–1942, 2007. ISSN 16197070. doi: 10.1007/s00259-007-0534-y.

L. H. Portnow, D. E. Vaillancourt, and M. S. Okun. The history of cerebral PET scanning: From physiology to cutting-edge technology. *Neurology*, 80(10):952–956, mar 2013. ISSN 0028-3878. doi: 10.1212/WNL.0b013e318285c135. URL `http://www.neurology.org/cgi/doi/10.1212/WNL.0b013e318285c135`.

A. Rahmim, J. Qi, and V. Sossi. Resolution modeling in PET imaging: Theory, practice, benefits, and pitfalls. *Medical Physics*, 40(6):064301, 2013. ISSN 0094-2405. doi: 10.1118/1.4800806. URL `http://scitation.aip.org/content/aapm/journal/medphys/40/6/10.1118/1.4800806$\delimiter"026E30F$nhttp://scitation.aip.org/deliver/fulltext/aapm/journal/medphys/40/6/1.4800806.pdf?itemId=/content/aapm/journal/medphys/40/6/10.1118/1.4800806{&}mimeType=pdf{&}containerItemId=conten`.

A. Reilhac, S. Tomeï, I. Buvat, C. Michel, F. Keheren, and N. Costes. Simulation-based evaluation of OSEM iterative reconstruction methods in dynamic brain PET studies. *NeuroImage*, 39(1):359–368, jan 2008. ISSN 10538119. doi: 10.1016/j.neuroimage.2007.07.038. URL `http://linkinghub.elsevier.com/retrieve/pii/S1053811907006659`.

O. Rousset, A. Rahmim, A. Alavi, and H. Zaidi. Partial Volume Correction Strategies in PET, 2007. ISSN 15568598.

R. Sanchez-Jurado, M. Devis, R. Sanz, J. E. Aguilar, M. d. Puig Cozar, and J. Ferrer-Rebolleda. Whole-Body PET/CT Studies with Lowered 18F-FDG Doses: The Influence of Body Mass Index in Dose Reduction. *Journal of Nuclear Medicine Technology*, 42(1):62–67, mar 2014. ISSN 0091-4916. doi: 10.2967/jnmt.113.130393. URL `http://www.ncbi.nlm.nih.gov/pubmed/24503348http://tech.snmjournals.org/cgi/doi/10.2967/jnmt.113.130393`.

D. R. Schaart, H. T. van Dam, S. Seifert, R. Vinke, P. Dendooven, H. Löhner, and F. J. Beekman. A novel, SiPM-array-based, monolithic scintillator detector for PET. *Physics in medicine and biology*, 54 (11):3501–3512, 2009. ISSN 0031-9155. doi: 10.1088/0031-9155/54/11/015.

H.-P. W. Schlemmer, B. J. Pichler, M. Schmand, Z. Burbar, C. Michel, R. Ladebeck, K. Jattke, D. Townsend, C. Nahmias, P. K. Jacob, W.-D. Heiss, and C. D. Claussen. Simultaneous MR/PET imaging of the human brain: feasibility study. *Radiology*, 248(3):1028–1035, 2008. ISSN 0033-8419. doi: 10.1148/radiol.2483071927.

P. Sharma, A. Mukherjee, C. Bal, A. Malhotra, and R. Kumar. Somatostatin receptor-based PET/CT of intracranial tumors: a potential area of application for 68 Ga-DOTA peptides? *AJR. American journal of roentgenology*, 201(6):1340–7, dec 2013. ISSN 1546-3141. doi: 10.2214/AJR.13. 10987. URL `http://www.ajronline.org/doi/abs/10.2214/AJR.13.10987http://www.ncbi.nlm. nih.gov/pubmed/24896203`.

L. A. Shepp and Y. Vardi. Maximum Likelihood Reconstruction for Emission Tomography. *IEEE Transactions on Medical Imaging*, 1(2):113–122, oct 1982. ISSN 0278-0062. doi: 10.1109/TMI.1982. 4307558. URL `http://ieeexplore.ieee.org/lpdocs/epic03/wrapper.htm?arnumber=4307558`.

A. Sher, F. Lacoeuille, P. Fosse, L. Vervueren, A. Cahouet-Vannier, D. Dabli, F. Bouchet, and O. Couturier. For avid glucose tumors, the SUV peak is the most reliable parameter for [18F]FDG-PET/CT quantification, regardless of acquisition time. *EJNMMI Research*, 6(1):21, 2016. ISSN 2191-219X. doi: 10.1186/s13550-016-0177-8. URL `http://www.ejnmmires.com/content/6/1/ 21`.

K. Shibuya, E. Yoshida, F. Nishikido, T. Suzuki, T. Tsuda, N. Inadama, T. Yamaya, and H. Murayama. Annihilation photon acollinearity in PET: volunteer and phantom FDG studies. *Phys. Med. Biol. Phys. Med. Biol*, 52(52):5249–5261, 2007. ISSN 0031-9155. doi: 10.1088/0031-9155/52/17/010. URL `http://iopscience.iop.org/0031-9155/52/17/010`.

Siemens. Siemens, 2016. URL `https://usa.healthcare.siemens.com/ magnetic-resonance-imaging/mr-pet-scanner/biograph-mmr/technical-details`.

A. Sonzogni. NuDat2, 2016. URL `http://www.nndc.bnl.gov/nudat2/`.

M. Soret, S. L. Bacharach, and I. Buvat. Partial-Volume Effect in PET Tumor Imaging. *Journal of Nuclear Medicine*, 48(6):932–945, jun 2007. ISSN 0161-5505. doi: 10.2967/jnumed.106.035774. URL `http://jnm.snmjournals.org/cgi/doi/10.2967/jnumed.106.035774`.

S. Surti. Update on Time-of-Flight PET Imaging. *Journal of Nuclear Medicine*, 56(1):98–105, jan 2015. ISSN 0161-5505. doi: 10.2967/jnumed.114.145029. URL `http://www.pubmedcentral. nih.gov/articlerender.fcgi?artid=4287223{&}tool=pmcentrez{&}rendertype=abstracthttp: //jnm.snmjournals.org/cgi/doi/10.2967/jnumed.114.145029`.

Y. F. Tai and P. Piccini. Applications of positron emission tomography (PET) in neurology. *Journal of neurology, neurosurgery, and psychiatry*, 75(5):669–676, 2004. ISSN 0022-3050. doi: http://dx.doi. org/10.1136/jnnp.2003.028175. URL `http://15090557`.

M. M. Ter-Pogossian, M. E. Phelps, E. J. Hoffman, and N. a. Mullani. A positron-emission transaxial tomograph for nuclear imaging (PETT). *Radiology*, 114(5):89–98, 1975. ISSN 0033-8419. doi: 10.1148/ 114.1.89.

S. Troncoso Skidmore and B. Thompson. Bias and precision of some classical ANOVA effect sizes when assumptions are violated. *Behavior Research Methods*, pages 536–546, 2012. ISSN 1554-3528. doi: 10.3758/s13428-012-0257-2.

P. Tylski, S. Stute, N. Grotus, K. Doyeux, S. Hapdey, I. Gardin, B. Vanderlinden, and I. Buvat. Comparative Assessment of Methods for Estimating Tumor Volume and Standardized Uptake Value in 18F-FDG PET. *The Journal of Nuclear Medicine*, 51(2):268–276, 2010. ISSN 1535-5667. doi: 10.2967/jnumed.109.066241. URL `http://jnm.snmjournals.org/cgi/content/abstract/51/2/268`.

UNSCEAR. *Sources and effects of ionizing radiation*, volume I. 2008. ISBN 9789211422740.

S. Vandenberghe and P. K. Marsden. PET-MRI: a review of challenges and solutions in the development of integrated multimodality imaging. *Physics in Medicine and Biology*, 60(4):R115, 2015. ISSN 0031-9155. doi: 10.1088/0031-9155/60/4/R115. URL `http://stacks.iop.org/0031-9155/60/i=4/a=R115{%}5Cnhttp://iopscience.iop.org/article/10.1088/0031-9155/60/4/R115/meta;jsessionid=2164445C37ABA46A50D9C8F11B2BEE76.c1/pdf`.

S. Vandenberghe, E. Mikhaylova, E. D'Hoe, P. Mollet, and J. S. Karp. Recent developments in time-of-flight PET. *EJNMMI Physics*, 3(1):3, dec 2016. ISSN 2197-7364. doi: 10.1186/s40658-016-0138-3. URL `http://dx.doi.org/10.1186/s40658-016-0138-3http://www.ejnmmiphys.com/content/3/1/3`.

M. D. Walker, J. C. Matthews, M.-C. Asselin, A. Saleem, C. Dickinson, N. Charnley, P. J. Julyan, P. M. Price, and T. Jones. Optimization of the injected activity in dynamic 3D PET: a generalized approach using patient-specific NECs as demonstrated by a series of 15O-H2O scans. *Journal of nuclear medicine : official publication, Society of Nuclear Medicine*, 50(9):1409–17, 2009. ISSN 0161-5505. doi: 10.2967/jnumed.109.062679. URL `http://www.ncbi.nlm.nih.gov/pubmed/19690021`.

M. D. Walker, M.-C. Asselin, P. J. Julyan, M. Feldmann, P. S. Talbot, T. Jones, and J. C. Matthews. Bias in iterative reconstruction of low-statistics PET data: benefits of a resolution model. *Physics in medicine and biology*, 56(4):931–49, feb 2011. ISSN 1361-6560. doi: 10.1088/0031-9155/56/4/004. URL `http://ieeexplore.ieee.org/document/5401635/http://www.ncbi.nlm.nih.gov/pubmed/21248391`.

K. P. Willowson, E. A. Bailey, and D. L. Bailey. A retrospective evaluation of radiation dose associated with low dose FDG protocols in whole-body PET/CT. *Australasian Physical & Engineering Sciences in Medicine*, 35(1):49–53, mar 2012. ISSN 0158-9938. doi: 10.1007/s13246-011-0119-8. URL `http://link.springer.com/10.1007/s13246-011-0119-8`.

H. Zaidi, editor. *Quantitative Analysis in Nuclear Medicine Imaging*. Springer US, Boston, MA, 2006. ISBN 978-0-387-23854-8. doi: 10.1007/b107410. URL `http://link.springer.com/10.1007/b107410`.

H. Zaidi and B. Hasegawa. Determination of the Attenuation Map in Emission Tomography. *Journal of Nuclear Medicine*, 44(2):291–315, 2003. ISSN 0161-5505, 2159-662X. URL `http://jnm.snmjournals.org/content/44/2/291$\delimiter"026E30F$nhttp://jnm.snmjournals.org/content/44/2/291.full.pdf$\delimiter"026E30F$nhttp://www.ncbi.nlm.nih.gov/pubmed/12571222`.

K. G. Zeimpekis, F. Barbosa, M. Hüllner, E. ter Voert, H. Davison, P. Veit-Haibach, and G. Delso. Clinical Evaluation of PET Image Quality as a Function of Acquisition Time in a New TOF-PET/MRI Compared to TOF-PET/CTInitial Results. *Molecular Imaging and Biology*, 17(5):735–744, oct 2015. ISSN 1536-1632. doi: 10.1007/s11307-015-0845-5. URL `http://link.springer.com/10.1007/s11307-015-0845-5`.

P. Ziai, M. R. Hayeri, A. Salei, A. Salavati, S. Houshmand, A. Alavi, and O. M. Teytelboym. Role of Optimal Quantification of FDG PET Imaging in the Clinical Practice of Radiology. *RadioGraphics*, 36(2):481–496, mar 2016. ISSN 0271-5333. doi: 10.1148/rg.2016150102. URL `http://pubs.rsna.org/doi/10.1148/rg.2016150102`.

S. Ziegler, B. W. Jakoby, H. Braun, D. H. Paulus, and H. H. Quick. NEMA image quality phantom measurements and attenuation correction in integrated PET/MR hybrid imaging. *EJNMMI physics*, 2(1):18, 2015. ISSN 2197-7364 (Electronic). doi: 10.1186/s40658-015-0122-3. URL `http://dx.doi.org/10.1186/s40658-015-0122-3`.

S. I. Ziegler. Positron Emission Tomography: Principles, Technology, and Recent Developments. *Nuclear Physics A*, 752(1-4 SPEC. ISS.):679–687, apr 2005. ISSN 03759474. doi: 10.1016/j.nuclphysa.2005.02.067. URL `http://linkinghub.elsevier.com/retrieve/pii/S0375947405002265`.

Appendix A

Supplementary Phantom Results

Reconstructed Images

Additionally to the reconstructed images in Subsection 4.1.2, a series of slices showing higher activity of the spheres is presented in Figure A.1 and a complete comparison of all acquisition times for a transverse slice in OSEM and PSF images is given in Figure A.2.
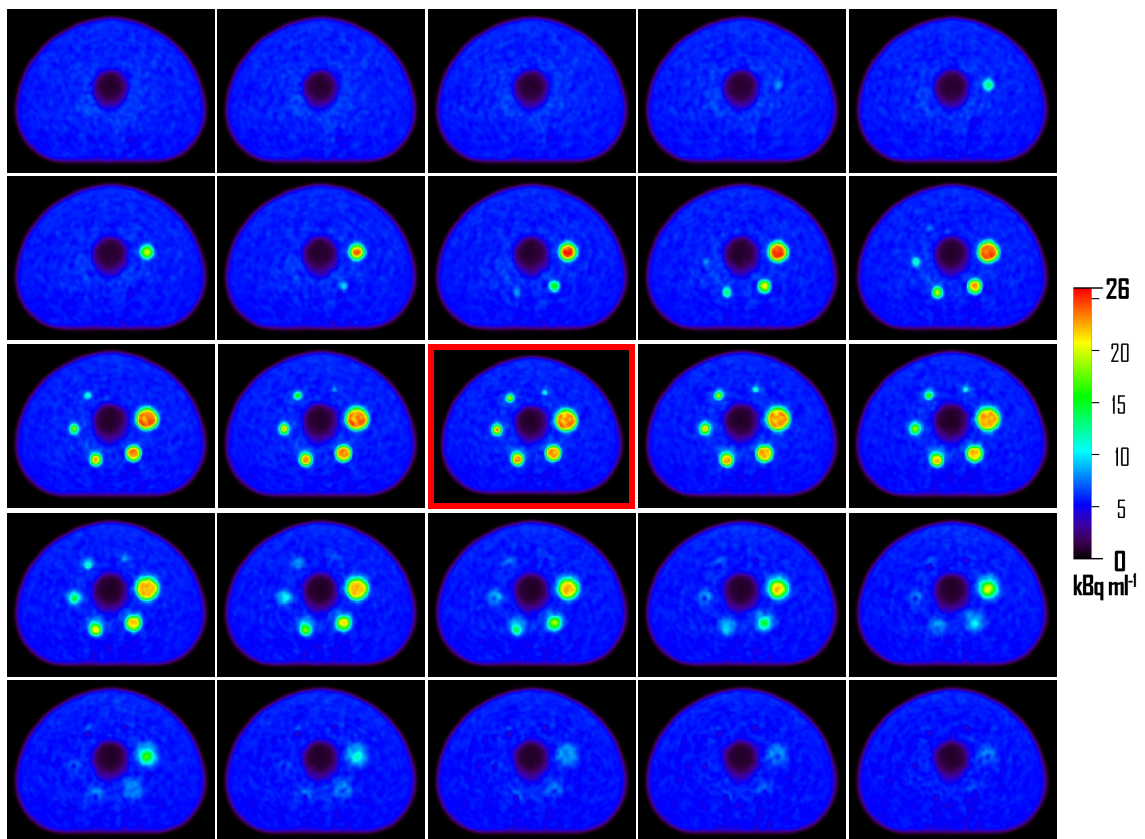

Figure A.1: *Consecutive transverse slices for the* 20 min *image with* **OSEM** *reconstruction. Sequence starts at top left and goes row-wise to bottom right. Slice that matches the center-plane of the spheres is marked with a red frame.*
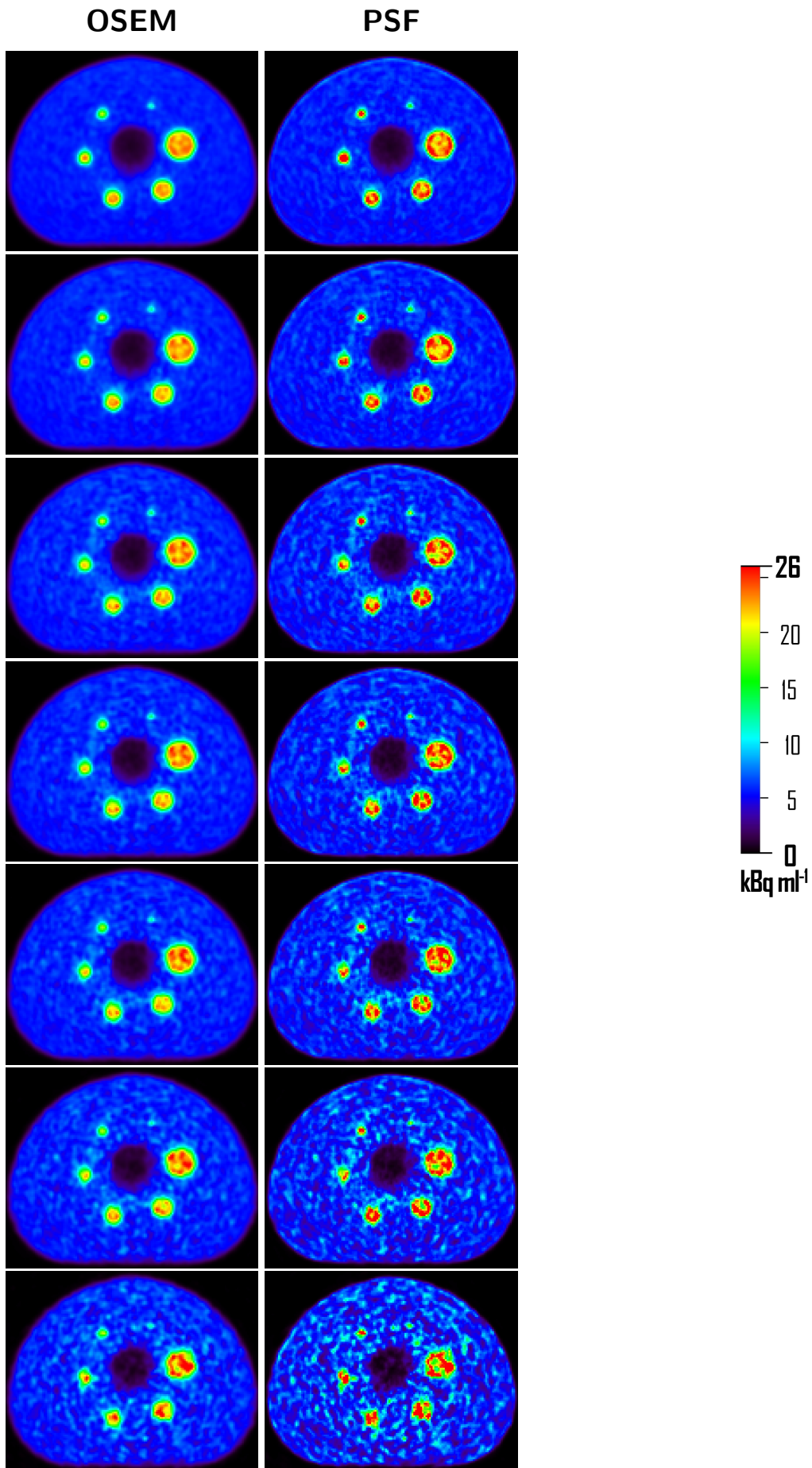
Figure A.2: *Transverse slices of **OSEM** (left column) and **PSF** (right column) images of the phantom for all acquisition times* 20 min, 10 min, 5 min, 4 min, 3 min, 2 min *and* 1 min *in descending order from top to bottom. Always first frame is shown, slices are taken at center of* 10 mm *sphere. Same colour scale applied to all images.*

II

Background

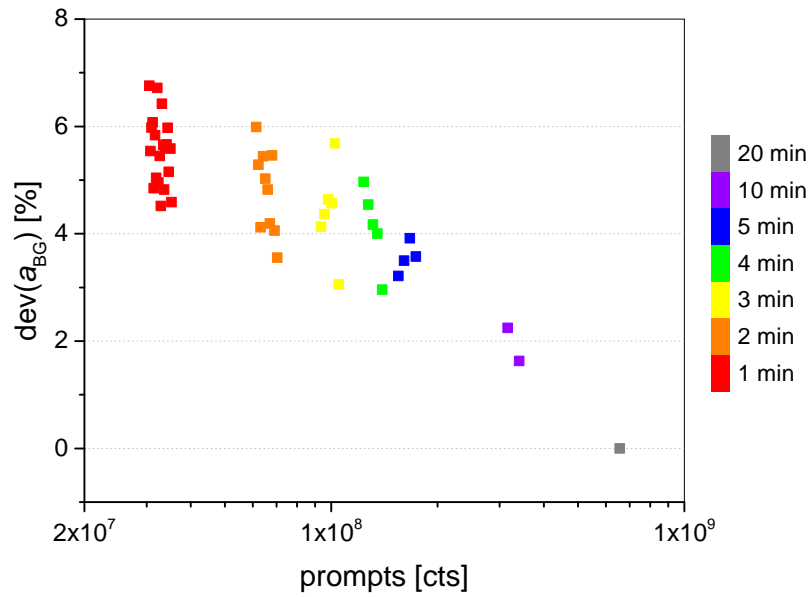Figure A.3 shows background activity for OSEM reconstruction as shown in Figure 4.4 for PSF.

Figure A.3: *Background activity* a_{BG} *as a function of number of counts in the image (for OSEM).*

Recovery Coefficient

In Subsection 4.1.5 the results of the RC-values were presented for the two extreme sizes of the spheres (10 mm and 37 mm) and discussed more generally for all sizes in between. For the sake of completeness, the results for the remaining spheres shall be given here.
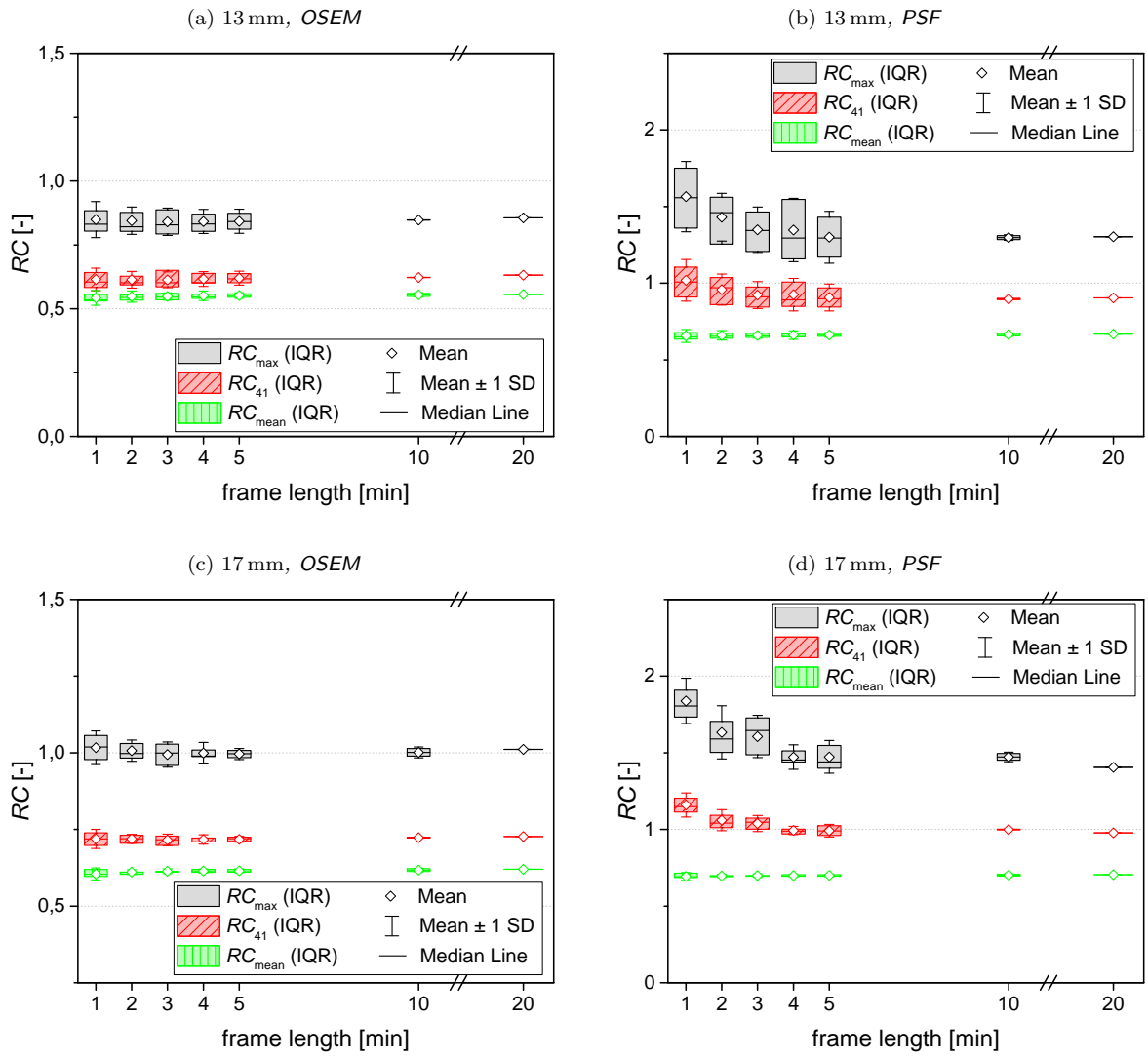
Figure A.4: *Dependence of RC_{max}, RC_{41} and RC_{mean} values on acquisition duration with OSEM (left column) and PSF (right column) reconstructions each, is shown for 13 mm (top row) and 17 mm (bottom row) spheres.*
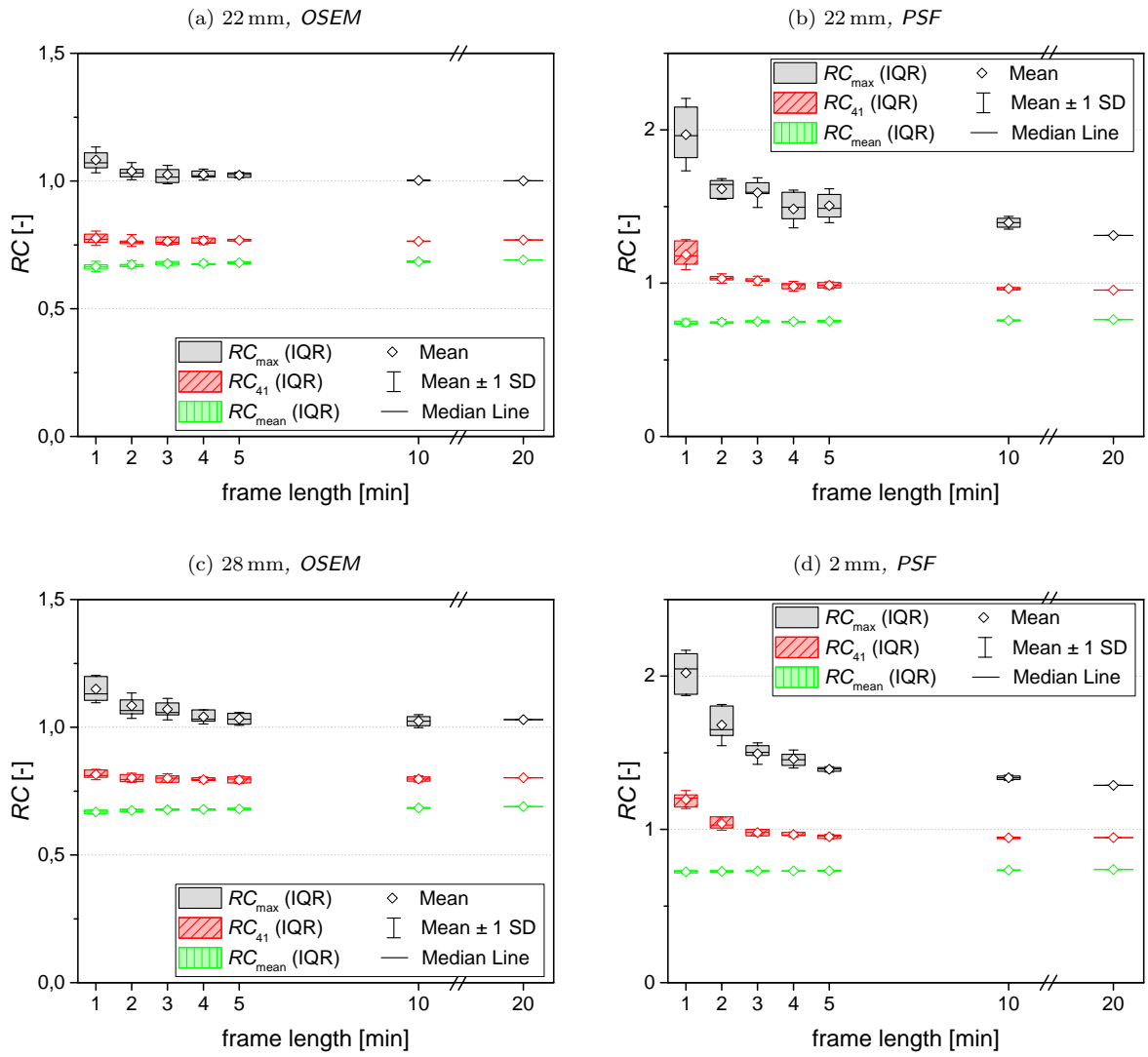
Figure A.5: *Dependence of* RC_{max}, RC_{41} *and* RC_{mean} *values on acquisition duration with* **OSEM** *(left column) and* **PSF** *(right column) reconstructions each, is shown for* 22 mm *(top row) and* 28 mm *(bottom row) spheres.*

Appendix B

Supplementary Patient Results

For the sake of completeness, results not presented in the main part due to redundancy are given here.

SUV-values

In addition to the SUV results for OSEM images shown in Figure 4.24, the respective graphs for PSF are given here.
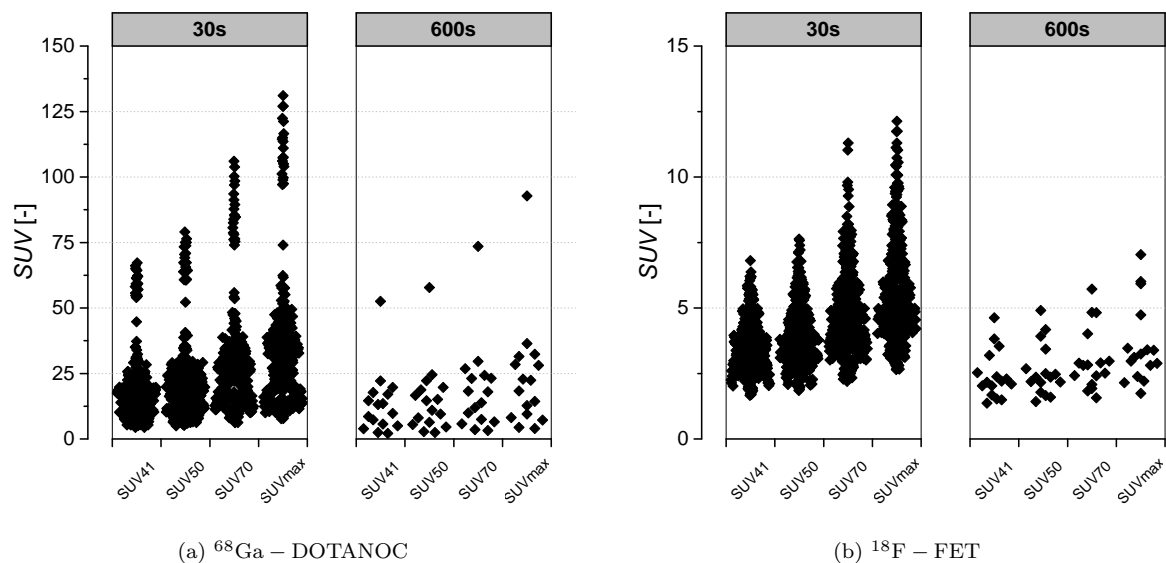

(a) ^{68}Ga − DOTANOC   (b) ^{18}F − FET

Figure B.1: *Comparison of absolute Standard Uptake Values at different threshold levels for* $30\,\mathrm{s}$ *and* $600\,\mathrm{s}$ *frame lengths. Figures (a) and (b) show the results for* ^{68}Ga − DOTANOC *and* ^{18}F − FET *patient data, respectively. Both groups contain* 16 *ROIs in the* $20\,\mathrm{min}$ *acquisition, reconstructed with PSF.*

Correlations

Figure B.2 shows the correlations of SUV_{41}, SUV_{50} and SUV_{70} with the corresponding SUV_{max} for ^{18}F − FET patients. For discussion of the graphs, see Subsection 4.2.6.
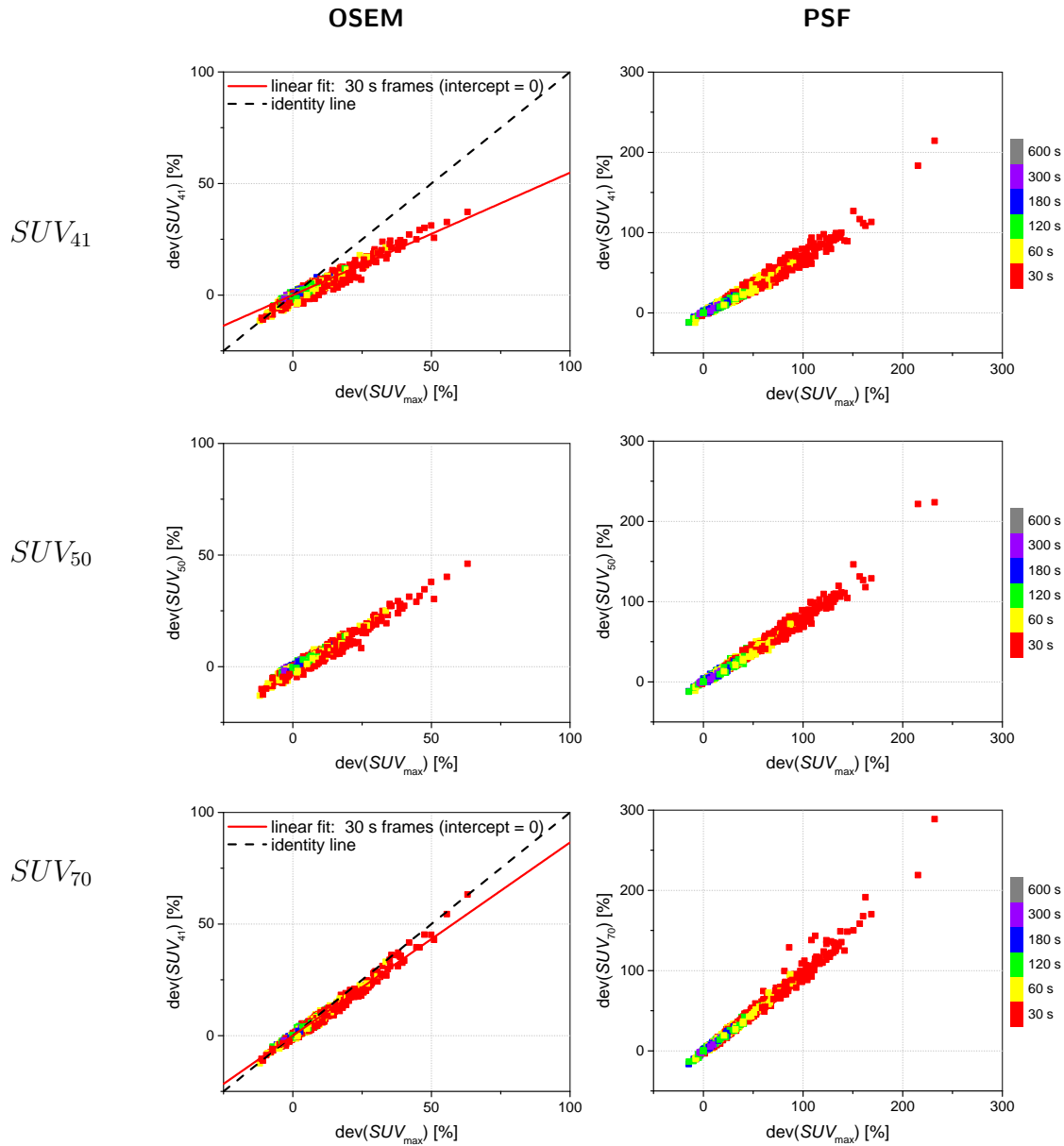
Figure B.2: *Correlation of SUV_{41}, SUV_{50} and SUV_{70} with the corresponding SUV_{max} in the 16 evaluated ^{18}F $-$ FET patients. Left column shows evaluation with reconstruction setting OSEM, right column with PSF. Values are plotted as deviations from the 10 min (600 s) frames. Colours indicate different frame lengths. For according images of ^{18}F $-$ FET patients see Appendix B.*